NTNU
Norwegian University of
Science and Technology

Investigation of Sloshing Inside Closed Aquaculture Plants

Christian Kosacki

NTNU
Norwegian University of Science and Technology

M.Sc. thesis

Spring 2017

Christian Kosacki

Investigation of Sloshing Inside Closed Aquaculture Plants

The aquaculture industry is seeing extensive technological development in the last years where new fish farm cage designs are proposed due to greater focus on environmental impact, efficiency and upscaling of the industry. In order to meet the growing demands, closed fish farm structures have been proposed as a solution. There are a number of prototypes and planned projects with closed aquaculture plants. The purpose will be to investigate the effect of *sloshing inside the closed plants*. This will affect the fish welfare, operations and requirements for structural strength.

In that regard, Professor Trygve Kristiansen of the Department of Marine Technology, NTNU, has proposed a thesis concerning the sloshing effect inside closed fish farm plants exposed to external waves. This subject is an opportunity for the student to work on both numerical and experimental hydrodynamics. The work will involve basic experiments in Lilletanken, as well as numerical work. The waves inside and outside the structure will interact, and sloshing waves are going to be excited. Basic examples will demonstrate this. Theoretical and numerical work will then be used to quantify these effects. Potential flow theory will be assumed.

The work may be carried out in steps as follows:

- Present literature study performed on the aquaculture industry and research done on sloshing.
- Present the governing equations and the basic theory describing the dynamics of a closed aquaculture plant at sea with two degrees of freedom assuming linear potential theory.
- Re-analyze data from the experiment conducted in the specialization project in the Fall of 2016 investigating sloshing inside a closed upright circular cylindrical fish farm plant subjected to regular waves.
- Create a numerical simulation of the free-surface elevation inside the closed aquaculture plant using linear modal theory assuming prescribed motions of the structure.
- Perform a sensitivity analysis to investigate the sensitivity of the numerical calculated free-surface elevation inside the closed plant regarding the prescribed motions.
- Inspect if non-linearities are occurring such as swirling and compare to theoretical results.

- Perform a coupled motion analysis of the given structure including sloshing.

The candidate should in his/her report give a personal contribution to the solution of the problem formulated in this text. All assumptions and conclusions should be supported by mathematical models and/or references to physical effects in a logical manner. The candidate should apply all available sources to find relevant literature and information on the actual problem.   The report should be well organized and give a clear presentation of the work and all conclusions. It is important that the text is well written and that tables and figures are used to support the verbal presentation. The report should be complete, but still as short and concise as possible.   The final report must contain this text, acknowledgment, summary, main body, conclusion, suggestions for future work, nomenclature, references, and appendices. All figures and tables in the main body must be identified with numbers. References should be given by author name and year in the text, and presented alphabetically by name in the reference list.   In the report, it should be possible to identify the work carried out by the candidate and what has been found in the available literature or new studies given to the candidate from other authors. It is important to clearly display the references to the original source for theories and experimental results.

The report must be signed by the candidate.

The thesis is to be submitted in DAIM.

Supervisor: Professor Trygve Kristiansen

Co-supervisor: David Kristiansen, SINTEF Ocean AS

Start: 15.01.2017

Deadline: 11.06.2017

Preface

This thesis is the final part of the Master in Science in Marine Technology degree specializing in marine hydrodynamics. The thesis is written at the Department of Marine Technology (IMT) at the Norwegian University of Science and Technology (NTNU), Trondheim, in the Spring of 2017, supervised by Professor Trygve Kristiansen. The work load of this thesis corresponds to 30 ECTS.

I have great interest in working with new technologies and ideas, and wanted to implement that into my master's thesis. Since the aquaculture industry is designing and testing new concepts it fit perfectly with my academic background and interest. The experimental work was performed during my specialization project in the Fall of 2016, and will be implemented into this master's thesis.

Trondheim, 9th-June-2017

Christian Kosacki

Acknowledgment

I would like to thank Terje Rostad and Torgeir Wahl for their great help during the experimental setup. I also want to thank Professor Trygve Kristiansen for great supervising, feedback and help during this project. I would also thank Alexander Timokha for explanation of sloshing theory and help in interpretation of some of the results. I would also thank my fellow student colleague Mona Tofte for the weekly discussions concerning sloshing and support when the thesis met difficulties. The thesis would not be as complete without your help. Lastly I would thank my girlfriend for supporting and motivation throughout the whole project.

C.K.

Abstract

This thesis concerns the sloshing effect inside closed fish farm plants exposed to external waves. To investigate the sloshing phenomenon, linear potential theory together with linear modal theory was implemented, and a model test at NTNU's Lilletanken using a floating circular cylinder with a free-surface on the inside was performed. The model scale was set to 1:81, representing a full scale enclosed fish farm plant with a diameter of 40 meters. Waves with three steepnesses $\frac{H}{\lambda} = \frac{1}{60}, \frac{1}{45}$ and $\frac{1}{30}$ with wave periods T $\in$ [3.6, 7.2] in full scales were used, and responses inside the bucket measured using wave probes, accelerometers and strain gauges at the anchoring lines.

The model test results show the largest measured sloshing amplitude occurs at $\omega = 1$ rad/s in full scale, corresponding to the coupled system frequency. The amplitude is measured to be 4-5 times larger than the incoming wave amplitude. The theoretical first sloshing mode is given at $\omega = 0.93$ rad/s, which is ≈ 10 % off the experimental sloshing amplitude. Due to linear theory, the Response Amplitude Operator (RAO) for the three steepnesses was expected to be similar, however the steepest wave gave a smaller RAO due to non-linearities like viscous damping of the model and overtopping of the outer collar of the model. The surge and pitch motions experiences a cancellation at each side of the natural sloshing frequency.

The comparison between the numerical sloshing amplitude and measured sloshing amplitude showed that the corresponding amplitudes over the frequency range did not match. The theoretical calculations resulted in a large top at the sloshing natural frequency followed by a smaller top at the experimentally found coupled frequency.

A sensitivity analysis of the prescribed motions used in the modal function solved numerically by the ODE45-function in MATLAB was performed. The results showed a great sensitivity of sloshing amplitude when varying the input parameters slightly, especially around the natural sloshing frequency of the sloshing. The new sloshing RAO with adjusted parameters fit the experimental sloshing RAO reasonably, except for the frequencies around the natural sloshing period.

The non-linear analysis showed presence of 2nd harmonic amplitudes at the sloshing RAOs

at the natural sloshing frequency, which were also visible in the time-series plots of sloshing taken from the model test. Swirling was also detected at the shorter wave lengths with dominant 2nd harmonics at the side probe WP1 at the sloshing frequency.

This study shows that the sloshing is difficult to predict correctly and linear modal theory has shortcoming especially around the natural sloshing frequency even with prescribed motions. The sensitivity analysis revealed also high sensitivity to the input parameters. Therefore, great care must be taken when calculating numerical sloshing amplitudes.

Contents

Nomeclature

Acronyms

DAF Dynamic Amplification Factor

DoF Degrees of Freedom

Fn Froude Number

FHF Fiskeri- og Havbruksnæringens Forskningsfond

RAO Response Amplitude Operator

Re Reynold Number

WAMIT Wave Analysis Massachusetts Institute of Technology

WP Wave probe

Greek Letters

β_n Modal function

η_j Body motion in j-direction

$\eta_j a$ Force amplitude in j-direction

ι Nondimensional root of the derivative of the Bessel function

λ Wavelength

λ_s Scaling factor

Ω Fluid domain

ω Angular frequency

ϕ Spatial velocity potential

ρ Liquid density

σ Forcing frequency

θ Phase angle of the calculated amplitudes

ξ Damping ratio

ζ Free surface

ζ_a Wave amplitude

ζ_{slosh} Sloshing wave amplitude

Coordinates

(x,z) Body-fixed coordinates

(x',y',z') Pre-corrected coordinates

Roman Letters

A_{ij} Added mass in j-direction due to force in i-direction

B Damping

B Collar breadth

C_g Group velocity

C Stiffness

F_{ex} Excitation forces

F_{HD} Hydrodynamic forces

F_{inner} Inner sloshing forces

f_z Distance between mean free-surface inside structure and z-accelerometer

g Gravity

H Collar height. If used with λ, it is wave height

H_j Transfer function in j-direction

h Water height

I Mass moment of inertia

k Wave number

M_l Liquid mass

m Mass

M Body Mass

n Unit vector pointing into the fluid

L_z Distance between z-accelerometers

p Pressure

R_0 Structure radius

t Time

T Period

Introduction

By 2050, the world population will surpass 9 billion people putting pressure on available food resources. In order to meet the increasing demand, food production has to increase by a predicted 60 % (FAO, 2016). A proposition to meet the demands is to develop the aquaculture industry with its reputation of being an efficient way of producing food. For Norway, the aquaculture industry has a potential of unfolding its value with a factor of six by 2050 ((DKNVS) and (NTVA), 2016).

Aquaculture has been driven by traditional methods using net cages up until around 30 years ago. Lately, there has been a fast technological development of aquaculture due to greater application of science (Edwards, 2015). Due to a greater focus on environmental impact, efficiency and upscaling of the industry, a number of prototypes and planned projected within the fish farming industry are being researched. Numerous fish farm concepts are already being developed and are given new development concessions from the Norwegian State (Fiskedirektoratet.no, 2016). This points to the aquaculture having great potential for expansion to meet the worlds demand for food in 2050 (Olsen et al., 2008).

Traditional cage systems placed far inshore rely on steady water exchange and have known problems regarding lice, fish escaping due to net breakage and waste management. By enclosing the fish farm, lice, fish escape and waste contamination can be controlled more efficiently. However, there are some major hydrodynamical differences between the two concepts.

Figure 1.1: *Neptun 3* closed fish farm plant located in Skaanevik, where Marine Harvest has its test production. The structure has a diameter = 40 meters and height = 22 meters (Kyst.no, 2016).

An enclosed structure like *Neptun 3* shown in Figure 1.1 is prone to sloshing when exposed to motions due to currents and waves. Sloshing is of concern for fish welfare and structural integrity of the farm and have to be taken into consideration in the design phase. The sloshing phenomenon is well know in other industries like LNG ships, petrol tankers on the roads, spacecraft fuel tanks. Therefore, the knowledge build over the years of research in the other fields can be applied to a new concepts, namely floating closed aquaculture plants.

1.1 Objectives

In this master thesis I will investigate linear sloshing inside closed fish farm plants. Sloshing inside these plants is of particular interest first and foremost because of fish welfare, operations and requirements for structural strength. The experimental data is taken from the

specialization project last semester. The objectives are listed below:

1. Present literature study performed on the aquaculture industry and research done on sloshing.

2. Present the governing equations and the basic theory describing the dynamics of a closed aquaculture plant at sea with two degrees of freedom assumiong linear potential theory.

3. Present the model test and re-analyze data conducted in the specialization project from the Fall of 2016.

4. Create a numerical simulation of the free-surface elevation inside the closed aquaculture plant using linear modal theory assuming prescribed motions of the structure. Compare these results to the experimental results.

5. Perform a sensitivity analysis to investigate the sensitivity of the numerically calculated free-surface elevation inside the closed plant regarding the prescribed motions.

6. Inspect if non-linearties are present in the model test and what effect these have compared to the theoretically calculated wave elevation of sloshing.

7. Perform a coupled motion analysis of the given structure including the sloshing effects.

1.2 Limitations

Resonant sloshing is a highly non-linear phenomenon, however transient and non-resonant sloshing can be described using linear theory. Therefore, the work is limited to linear theory as the experiment is performed in linear conditions. However, the non-linearities will be investigated in the results in order to investigate the linear assumptions. The present work is restricted to only one model test where we consider the surge and pitch motion as the only contributing motions to the sloshing.

1.3 Approach

To couple the relevance of this thesis to the industry, a literature study is going to be formed. The literature study is a continuation from the specialization project in the Fall of 2016. This will also give an insight into the problems the aquaculture industry is facing from a technological perspective, as well as give insight into the research that has been done on sloshing. Further, a theoretical inspection of the fluid domain has to be performed in order to reach objective 2.

The third objective is to present and re-analyze the data collected from the model test in the Fall of 2016 due to correction factors which were not included, as well as keeping the body-fixed coordinate system opposed to the Earth-fixed used in the project. A more detailed extraction of amplitudes will also performed.

The fourth objective undertakes the task of solving the sloshing equation in order to find the surface elevation due to sloshing. This is performed by solving the modal function using MATLAB ODE45-function. The results from the numerical calculations and experimentally found sloshing amplitudes are going to compared by amplitude comparison, phase difference and RAOs.

The fifth objective is performed to inspect the sensitivity of the numerical sloshing amplitude regarding the prescribed motions. The prescribed motions are slightly varied and the numerical scheme is performed to see the differences.

The sixth objective is to investigate the non-linear effects that can contribute to the deviation from linear theory. The first, second and third harmonics will be extracted and compared as well as time-series of the model test will be inspected in order to study the non-linearities.

The last objective is not reached due to the challenges met in the previous objectives. A great amount of time was used to understand why the comparison between numerical calculations and model test did not match. Unfortunately, no time was left to perform the coupled analysis, but is suggested as a recommendation for further work.

1.4   Structure of the Report

Chapter 1: Literature study introduces aquaculture and sloshing as a topic. The literature study covers the importance of aquaculture for the future, the current state in Europe and Norway, challenges of traditional fishing industry and why new concepts like closed fish farms are being researched.

Chapter 2: Theory introduces the basic concepts behind potential theory inside a closed structure filled with a fluid and the spectral problem, which is the basis for the sloshing natural frequencies and the approach to finding the theoretical sloshing amplitudes. The chapter goes also through the dynamics of a mass-spring system as well as coupled motion. Lastly, it finishes with a brief insight into the equation of motion coupled with sloshing.

Chapter 3: Model Test presents the experimental setup for the model test in detail. The Chapter also describes the possible error sources and the post-processing procedure, where the acquired raw data is prepared to present the results.

Chapter 4: Results includes the observations and findings from the model test, as well as the calculated sloshing results. The data is compared, inspectede and commented. The sensitivity analysis is performed by the variation of surge acceleration and distance between then enclosed mean free-surface and accelerometer. The results are compared to the experimental results to check the sensitivity of the parameters. A non-linear analysis is also performed to investigate if non-linearities are present and their effect.

Chapter 5: General Discussion gives a general discussion of the experiment and the findings.

Chapter 6: Conclusion gives a conclusive summary of the whole investigation and proposes recommendations for further work.

1.5   Literature Study

The following section presents the general background of the aquaculture industry in a global scale down to the trends in Norway's aquaculture industry. Further, the sloshing phenomenon is presented together with areas of application and work that has been done. This literature study is a continuation of the project thesis in the Fall of 2016.

1.5.1   Aquaculture

In a global perspective the world population is estimated to exceed 9 billion people by 2050. Increasing the world population by 2 billion people, from today's 7 billion, carries major challenges regarding food supply and environmental impact. A potential solution is to develop the fish farm industry due to fish being a great protein source and containing important nutrients which is also considered as part of a healthy diet.

By the mid 1970's, fish made up a total of 7 % as a food source. 30 years later, in 2004, the aquaculture industry increased the share to 39 % (FAO, 2016). The aquaculture industry has shown tremendous growth, and by applying modern and innovative technology, the aquaculture industry has major potential to face the increasing food demand over the next decades.

Global statistics show that the aquaculture has gone through a very fast growth since the 1990 (Olsen et al., 2008). With China leading with a total increase of 34 % between 1990 and 2000, other countries including Norway are also expanding (Brugère and Ridler, 2004). Olsen et al. (2008) points to a global increase in aquaculture production between 0.4 % and 5.3 % per year between 2008 and 2020-2050. A report published by the *Food and Agriculture Organization* of the United Nations (FAO, 2016) states that aquaculture industry is the quickest expanding animal-production segment of the food industry with a 37 % increase in the past decade.

Aquaculture accounts for 47 % of world fish production, but due to careful regulations preventing overfishing and environmental pollution, the European production is far below its

potential (Monteiro and Salvador, 2014). The European production was only 2.6 % in volume and 5.1 % in value of the world production, however with more technologically advanced fish farms with sophisticated control systems, the industry can achieve significantly higher production rates.

Norway stands out being the worlds largest producer of Atlantic salmon (Laksefakta.no, 2016). One of the reasons for its success is due to the traditional open-net cages which utilize the access to fresh and clean seawater. In 2015, the export value for Norwegian salmon and trout exceeded 50 billion NOK corresponding to over 1 million tons of salmon exported. Data from *ssb.no* present the export value of 2016 of salmon showing promising numbers for 2016 as well (SSB.no, 2016).

The traditional aquaculture is based inshore in shallow waters. Good quality fish are dependent on water flow through the cage ensuring oxygen rich and pollution free water (Sveälv, 1988). Although Norway has good access to fresh sea water, a larger density of traditional cages installed in shallow inshore locations introduces the problem of eutrophication of water in which the cages are placed (Edwards, 2015). Eutrophication is the depletion of oxygen in a given volume. Normally, the cages have no waste control systems meaning the waste diffuses into the water surroundings, slowly settling on the bottom. However due to shallow water and underwater currents, the waste drifts into nearby cages decreasing oxygen concentrations and water quality typically leading to massive fish kills.

A common factor for aquaculture is that fish is grown at a greater density than in nature, making it likely to affect the local environment (Crawford and MacLeod, 2009). New enclosed fish farm concepts lessen the effect of environmental impact by controlling the environment surrounding the fish, making them comparable to onshore fish farms. They are being proposed over traditional cages due to reduction of lice problems, waste accumulation underneath the cages and fish escaping.

The modern aquaculture industry is still in its infancy due to the relatively late application of science and technology. Therefore new ideas and concepts as well as creative thinking is immensely important for new innovative solutions (Shainee et al., 2013). New concepts like the totally enclosed fish farms are being proposed enabling total control of the environment as well as careful monitoring and control of the water flow inside, waste collection and water

filtering. However, the motion of water inside closed offshore cages can actually lead to sea sickness of the fish due to the fish following the water particles circular paths (Helling et al., 2003).

1.5.2 Sloshing

When a ship with liquid tanks moves in waves, sloshing may happen. The sloshing phenomenon occurs for any moving tank with a free surface. The effect is important to consider during design because of the danger of uncontrolled resonant excitation of the liquid inside (Faltinsen and Timokha, 2009). The moving fluid can lead to structural instability and damage, or induce larger fatigue on for example LNG tankers, or in more modern cases, enclosed floating fish farms.

Sloshing has been a topic of interest for many years, especially for the aeronautical industry in the 1960's. Sloshing inside large fuel tanks on spacecrafts during take-off could send the vessel off course, thus giving aeronautical engineers a very good reason to do extensive studies of this phenomenon (Abramson, 1966). Another topic of interest are the massive LNG-containers on LNG-tankers. The containers have typical filling levels of 95-97 percent due to boil-off (Bass et al., 1985). The boil-off introduces a free surface with can cause sloshing inside these tanks. Another critical moment occurs under loading and off-loading of LNG where the tanks are only partly filled, exposing the ship to the danger of sloshing.

Anti-roll tanks on ships exploit the sloshing phenomenon to decrease the roll motions of a ship. These tanks are cleverly designed and engineered to be out of phase reducing the roll motion. Large buildings swaying in the wind can also have these systems integrated. Harbors are also exposed to sloshing due to large water volumes which can lead to substantial forces (Miles, 1974).

Considering floating closed aquaculture plants with large free surfaces, sloshing inside can occur. Sloshing can cause heavy loads on the structure and also affect fish welfare. The dynamic pressures and accelerations in the tank will also affect circulation which is necessary to provide the fish with oxygen rich water.

The mentioned cases are only some areas of interest where sloshing has to be considered. Sloshing has been extensively studied using many analytical, numerical and experimental methods. However, this phenomenon is challenging to predict due to its largely nonlinear nature including breaking waves, water spray and mixing of air and water or oil.

The linear problem is also solvable for response of irregular motions of the tank, however if the fluid is nonlinearly dependent on the forced motion, the problem becomes highly complex (Solaas, 1995). Additionally, analytical solutions do not include impact pressure or loads, breaking waves, vortex shedding due to potential theory, water inlet or drainage due to potential flow assumptions.

Abramson (1966) shows extensive investigation into both linear and nonlinear analytical solutions for sloshing inside tanks with different geometries. The analytical solutions are given for three dimensional rectangular tanks as well as vertical cylinder tanks. These solutions are solved for tanks in both sway and surge (rotational and translational motion) with harmonic motion. In reality harmonic motions are replaced by the the motions of the vessel introducing a coupling between motions outside and inside the tank.

The analytical solutions can also expand to non-linear solutions using potential theory. Faltinsen (1974) derives a nonlinear analytical solution using a inviscid boundary-value problem of potential flow for sloshing inside a two dimensional tank.

The analytical solutions fall short when breaking waves and spray are introduced because of their nonlinear nature. The analytical solutions also get hard to handle due to the shear size of expressions. Therefore numerical and experimental approaches are introduced that can show effects that are not taken into account in theory or are too complicated to calculate analytically. The numerical models are also suitable to validate experimental work.

At the flume tank of the Department of Marine Hydrodynamics at NTNU, Rognebakke and Faltinsen (2003) performed experimental work investigating the coupling between ship motions and sloshing excitation. A two dimensional box-shaped ship section excited by regular waves that is only allowed to move in surge is performed. The experimental results and computed linear and nonlinear values are compared. The results show that the linear model follows the general trends of the experiments although prediction of sway amplitude and

frequency of minimal sway is inaccurate. The non-linear calculations show agreement with experiments.

Small scale experiments performed by Abramson (1966) using different geometries such a rectangular, circular and spherical tanks with different separation devices splitting the inside into compartments are done. The experiments are performed to study the effects of dampening devices and viscosity on sloshing. These test were done for further investigation into designing fuel tanks for spacecrafts.

Offshore storage tanks which are gravity based structures placed on the ocean floor can be susceptible to internal sloshing due to hydroelasticity or earthquakes shaking the bottom. Chakrabarti (1993) performed an experiment studying the effects of wall deflections as well as bottom displacement by rotational and translational motion of the test model. The experimental data was compared with linear theory which showed that with a fitting damping factor, potential theory can be used to predict sloshing with small amplitudes inside a partly filled circular cylinder.

There are many numerical models using finite difference methods, finite volume methods, finite element methods and boundary element methods. Each of these numerical methods have strengths and weaknesses opening the possibility for validation by conducting experimental tests. Rafiee et al. (2011) use a partly filled simple rectangular tank equipped with pressure sensor excited in sway motion. The surface at a given time frame as well as pressure calculations can be compared. The report concludes that there is good agreement between experiments and simulation but some impact pressures are overestimated.

Theory

The aim of this Chapter is to give a mathematical overview of the sloshing problem focusing on linear sloshing theory, modal theory for circular cylinders and dynamic response. The first part introduces the governing equations regarding potential flow and linear sloshing theory. The linear sloshing theory is based on potential theory and will be presented for 3D circular cylinders. Further, modal theory is presented in form of a 2D rectangular tank in sway. The example is used in order to present the general modal theory where pitch is included. This leads to the formulation of hydrodynamic coefficients and modal functions for circular tanks needed in order to find the sloshing amplitudes. A system with 1 and 2 DOF are also presented leading to the total coupled equation of motion. Lastly, a short overview of the coupled motion problem is given. Sloshing introduced new terms into the coupled equation of motion, and alters the natural frequencies. Since this part was meant for the last objective that was not reached, only a short overview will be given.

The theory chapter is based on Faltinsens *Sloshing* (Faltinsen and Timokha, 2009) and *Sea Loads on Ships and Offshore Structures* (Faltinsen, 1990). This is meant as an overview over the sloshing problem and how to approach the spectral problem in a general fashion. The theory does not go into full detail due to the shear complexity and amount. If the reader is interested, all the details can be found in chapter 4 and 5 in *Sloshing* Faltinsen and Timokha (2009).

The linear sloshing frequencies and modes can be described analytically in both rectangular and circular tanks. The lowest natural sloshing frequencies are of particular interest due to the severity of these waves. Linear theory is limited to nonresonant and transient sloshing because of the assumptions of potential flow which has no damping effects. Resonant sloshing is therefore dominated by non-linearities. If damping of the sloshing wave is introduced, there will be a range where sloshing acts as a damper. In reality, nonlinear contributions of the free surface will cause finite sloshing amplitudes due to transfer of energy to higher modes.

There are numerous ways of estimating the natural frequencies, like domain decomposition, benchmark numerical solutions or variational calculus, but we limit ourselves to analytical solutions which are applicable for 2D and 3D rectangular and circular tanks by applying separation of variables.

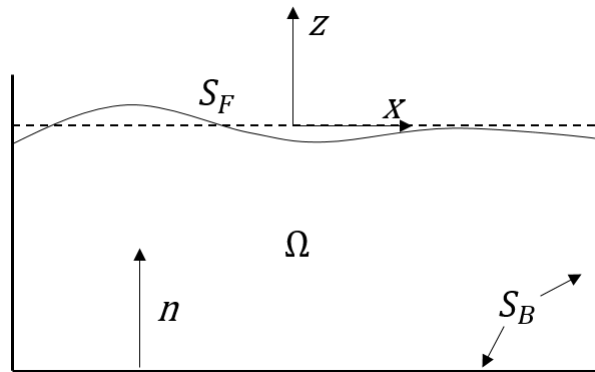We linearize the sloshing problem by assuming small amplitudes of sloshing $\rho << l$.

Figure 2.1: Illustration of linearized sloshing inside a closed tank. The domain is denoted as Ω and the boundaries as $S = S_B + S_F$. The coordinate system (x,z) is defined at the mean free surface. The normal vector n is pointing into the fluid domain.

2.1 Governing Equations

Linear modal theory for sloshing is described by the potential flow theory. The potential theory is a simplification of reality by assuming the flow domain Ω to be inviscid, incompressible and irrotational. Given these assumptions, the fluid is evaluated with the Laplace equation

$$\nabla^2 \phi = 0 \quad \text{in } \Omega \tag{2.1}$$

where ∇ is the nabla operator and the velocity is defined by the gradient of the velocity potential $u = \nabla \phi$. We want to solve for the velocity potential ϕ over the domain Ω. For solving this, we use relevant boundary conditions which consist of a dynamic and kinematic free-surface conditions along S_F while for S_B we define a no permeability condition.

For the free surface, the utilize the dynamic free-surface condition derived from the Bernoulli's equation. The Bernoulli's equation relates the pressure p in the fluid, velocity and gravita-

tional forces per fluid volume at any point in the fluid domain

$$p + \rho \frac{\partial \phi}{\partial t} + \rho \frac{1}{2} \left(\frac{\partial \phi}{\partial x} \right)^2 + \rho \frac{1}{2} \left(\frac{\partial \phi}{\partial z} \right)^2 + \rho g z = C \tag{2.2}$$

where ρ is the fluid density, g is the gravitational acceleration and z is the vertical coordinate in the coordinate system defined at the free surface as in Figure 2.1. C is an arbitrary constant. For the special case of no flow in the fluid domain, we have that $p + \rho g z = C$ from equation (2.2), and $C = p_a$ which is the atmospheric pressure at $z = 0$. This leads to the dynamic free surface condition which says that the fluid pressure is equal to the atmospheric pressure p_a at the free-surface S_F.

$$g\zeta + \frac{\partial \phi}{\partial t} + \frac{1}{2} \left(\left(\frac{\partial \phi}{\partial x} \right)^2 + \left(\frac{\partial \phi}{\partial z} \right)^2 \right) = 0 \qquad \text{on } S_F \tag{2.3}$$

The other condition, namely the kinematic free-surface condition, says that a fluid particle on the free-surface is to stay on the free-surface. This means that this satisfies $F(x, z, t) = z - \zeta(x, t) = 0$ which describes the fluid elevation. This leads to the kinematic boundary condition which is applicable on the free-surface

$$\frac{\partial \zeta}{\partial t} + \frac{\partial \phi}{\partial x} \frac{\partial \zeta}{\partial x} - \frac{\partial \phi}{\partial z} = 0 \qquad \text{on } S_F \tag{2.4}$$

Further we look at the solid boundaries where the no permeability condition is applied, giving

$$\frac{\partial \phi}{\partial n} = U n \qquad \text{on } S_B \tag{2.5}$$

where U is the velocity of the boundary relative to the defined Earth-fixed coordinate system.

If the linearized problem is investigated, the boundary itself does not evolve in time. The boundary condition is therefore imposed on the initial condition, reducing (2.3) and (2.4) to the following equations

$$\begin{aligned} \frac{\partial \phi}{\partial t} &= - g\zeta \qquad \text{on } z = 0 \\ \frac{\partial \zeta}{\partial t} &= \frac{\partial \phi}{\partial z} \qquad \text{on } z = 0 \end{aligned} \tag{2.6}$$

where $\frac{\partial}{\partial z} = -\frac{\partial}{\partial n}$ due to the normal vector pointing into the fluid. Therefore, a known velocity potential gives the possibility to find the free-surface elevation. As the velocity potential ϕ oscillates harmonically in time with circular frequency ω, it is possible to find the combined

free-surface condition using equation (2.6).

$$-\omega^2\phi + g\frac{\partial\phi}{\partial z} = 0 \qquad \text{on } S_F \tag{2.7}$$

2.1.1 Coordinate System and Rigid-Body Motion

We define the translatory rigid-body motions as surge η_1, sway η_2 and heave η_3. The angular motions are reffered to as roll η_4, pitch η_5 and yaw η_6. For the case of a floating fish farm, we concentrate on the vertical motion heave, longitudinal motion surge and roll which is the angular motion about the longitudinal axis. We define the coordinate system, the translatory and angular motion in the following way

$$s = \eta_1\vec{i} + \eta_2\vec{j} + \eta_3\vec{k} + \omega \times r \quad \text{where} \quad \omega = \eta_4\vec{i} + \eta_5\vec{j} + \eta_6\vec{k} \tag{2.8}$$

where $\vec{i}$, $\vec{j}$, $\vec{k}$ are called the unit vectors which are along the x-, y- and z-axis. This leads to the total equation

$$s = (\eta_1 + z\eta_5 - y\eta_6)\vec{i} + (\eta_2 - z\eta_4 + x\eta_6)\vec{j} + (\eta_3 + y\eta_4 - x\eta_5)\vec{k} \tag{2.9}$$

In our case, we focus on the surge and pitch motions first and foremost. Heave motion will be discussed in the Chapter 4. Equation (2.9) is therefore reduced to

$$s = (\eta_1 + z\eta_5)\vec{i} \tag{2.10}$$

We operate with two different coordinate systems, namely the Earth-fixed and body-fixed coordinate system. The Earth-fixed coordinate system is fixed and does not move with the motion of the body. The body-fixed coordinate system is fixed onto a point on the body and will therefore move with the body. For the calculation of sloshing amplitude and presentation of results, body-fixed coordinates are used.

2.2   Natural Sloshing Modes

This Chapter describes how to estimate natural sloshing frequencies by an analytical approach. The lowest natural frequencies are of interest due to their severe natures. This is where the largest sloshing occurs. There exist some analytical solutions for both rectangular and circular tanks in both two and three dimensions. In the specialization project the spectral problem for rectangular tanks was described. We will now proceed with a three dimensional case for circular cylinders. The following section is only a recapitulation of theory which does not go into full detail. A full explanation can be found on page 122 to 125 and 133 to 135 in Faltinsen and Timokha (2009).

2.2.1   Natural Frequencies and Modes

The natural sloshing frequencies and natural sloshing modes are nontrivial solutions for no external applied force. Linear natural sloshing modes imply that linear potential theory is valid as explained in Section 2.1. The coordinate system is set at the mean free-surface with the z-axis pointing upwards, where the mean free-surface is a linearized condition given by equation (2.6). As there is no tank excitation, equation (2.5) equals to 0. Another requirement is the conservation of fluid volume given as $\int_{S_F} \zeta\, dx dy = 0$ where $z = \zeta(x, y, t)$. Because of the solution being time-periodic with circular frequency σ, the solution is expressed as

$$
\begin{aligned}
\zeta(x, y, t) &= f(x, y) e^{i\sigma t} = \phi(x, y, 0) e^{i\sigma t} \\
\Phi(x, y, z, t) &= \frac{ig}{\sigma} \phi(x, y, z) e^{i\sigma t}
\end{aligned}
\tag{2.11}
$$

where the real part of f and ϕ is evaluated. By substituting (2.11) into (2.3) and (2.4), we get the spectral problem

$$
\begin{aligned}
\nabla^2 \phi &= 0 & \text{in } \Omega & & \frac{\partial \phi}{\partial n} &= 0 & \text{in } S_B \\
\frac{\partial \phi}{\partial z} &= k\phi & \text{in } S_F & & \int_{S_F} \phi\, dx dy &= 0
\end{aligned}
\tag{2.12}
$$

The spectral problem is a homogeneous problem with an infinite number of natural modes ϕ_n and corresponding natural frequencies $\sigma_n = \sqrt{g\kappa_n}$ where n = 1,2,3..., and κ are the so

called spectral values.

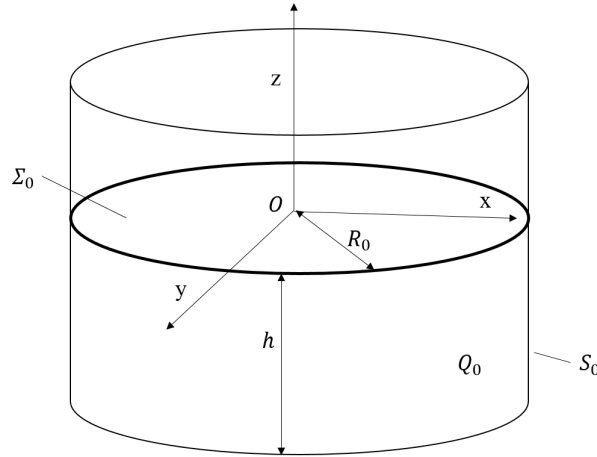## 2.2.2 3D Upright Circular Cylindrical Tanks

Figure 2.2: 3D upright circular cylinder with coordinate system. R_0 is the tank radius, h is the liquid height, S_0 is the mean wetted surface of the tank, Q_0 is the mean liquid domain, and Σ_0 is the mean liquid surface tank.

For a 3D upright circular cylinder, there exists an exact solution for the natural modes and frequencies. The solution is best considered using polar coordinates, and can be found using separation of variables for $\phi = R(r)\Theta(\theta)Z(z)$. The solutions are the natural modes of the Laplace equation, which are called Bessel functions. The spectral problem for an upright circular cylinder is given as

$$
\begin{aligned}
\nabla^2 \phi &= 0, && 0 \le r < R_0, && -h \le z < 0, && 0 \le \theta < 2\pi \\
\frac{\partial \phi}{\partial r} &= 0, && r = R_0, && -h < z < 0, && 0 \le \theta < 2\pi \\
\frac{\partial \phi}{\partial z} &= 0, && z = -h, && r < R_0, && 0 \le \theta < 2\pi \\
\frac{\partial \phi}{\partial z} &= \kappa \phi, && z = 0, && r < R_0, && 0 \le \theta < 2\pi, \quad \phi(r,\theta,z) = \phi(r,\theta+2\pi,z) \\
& \int_0^{R_0} r \int_0^{2\pi} \phi(r,\theta,0)\, d\theta\, dr = 0
\end{aligned}
\tag{2.13}
$$

where z is the vertical position, h is the water depth and R_0 is the radius. By performing the separation of variables, the solution for the potential ϕ is given as

$$\phi_{m,i}(r,\theta,z) = J_m\left(\iota_{m,i}\frac{r}{R0}\right)\frac{\cosh(\iota_{m,i}(z+h)/R_0)}{\cosh(\iota_{m,i}h/R_0)} \times \begin{cases} \cos(m\theta) \\ \sin(m\theta) \end{cases} \quad m = 0,1,...; \quad i = 1,2,.... \quad (2.14)$$

where $\iota_{m,i}$ is related to the nondimensional roots of the derivative of the Bessel function $J'_m(l_{m,i}) = 0$ of the first kind where an infinite sets of these roots exists for every m. However, due to the right hand side of the modal equation (2.22) being zero except for $m = 1$, we do not consider other than $m = 1$. The index i represents the current mode, with $i = 1$ being the lowest mode and therefore corresponds natural mode of the system. Due to the polar coordinate system, the wave number k is described in angular and radial direction. Due to the circumstances of the experiment perform, we will only focus on the cosine term, which correspond to wave in-line with the incoming waves.

The surface patterns at $z = 0$ with only the cosine term and $m = 1$ as well as the corresponding natural frequencies are defined as

$$f_{1,i}(r,\theta) = \phi_{1,i}(r,\theta,0) = J_1\left(\iota_{i,1}\frac{r}{R_0}\right)\cos(\theta)$$

$$\sigma_{1,i}R_0/g = \iota_{1,i}\tanh(\iota_{1,i}h/R_0)$$

(2.15)

The lowest mode corresponds to $m = 1$ and $i = 1$, giving the first natural mode. The natural period is therefore given as

$$T \approx T_{1,1} = \frac{2\pi}{\sqrt{g\iota_{1,1}\tanh(\iota_{1,1}h/R_0)/R_0}}$$

(2.16)

where $g = 9.81\,m/s^2$, $\iota_{1,1} = 1.841$, h is the liquid depth and R_0 is the radius. The natural period for different radii R_0 is given for varying liquid depth is given in Figure 2.3. The figure shows that there is a lower limit of T corresponding to infinite liquid depth. The ratio $h/R_0 > 1.0$ gives less than 2.5 % difference from the infite depth value, while $h/R_0 > 1.5$ gives less than 1.0 %.
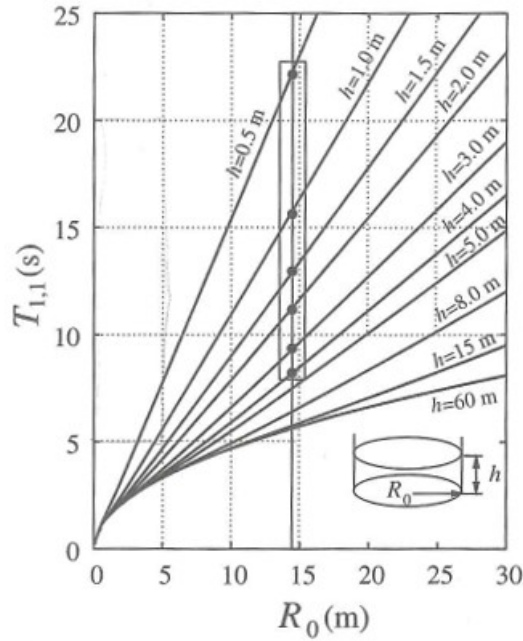
Figure 2.3: First mode of natural sloshing period for an upright circular cylinder for varying R_0 and height h (Faltinsen and Timokha, 2009). First mode of natural sloshing period for an upright circular cylinder with full scale radius $R_0 = 20.25$ m and water depth $h = 19.2$ m gives $T_{1,1} = 6.86$ s.

2.3 Linear Modal Theory

Modal theory is used when studying forced motions of rectangular tanks and circular cylinders. Modal theory changes the boundary value problem into a system of ordinary differential equations. The unknowns are generalized coordinates of the natural sloshing modes which are used to describe the free surface elevation inside a tank. By setting the tank in motion, we introduce $\frac{d\phi}{dx} = v_{01}$ at the tank walls. Even though we introduce an added motion, the potential theory with small liquid motions is still valid. This means that there is no damping at resonance giving a theoretical unlimited response. Normally, viscous effects are included acting as dampers. The following presents a rectangular tank with breadth l and depth h that is exposed to a horizontal velocity $v_{01}(t)$. The concept is introduced using a rectangular 2-dimensional tank and will move over to more general solutions in section 2.3.1. Equations (2.17) shows the modified boundary value problem.
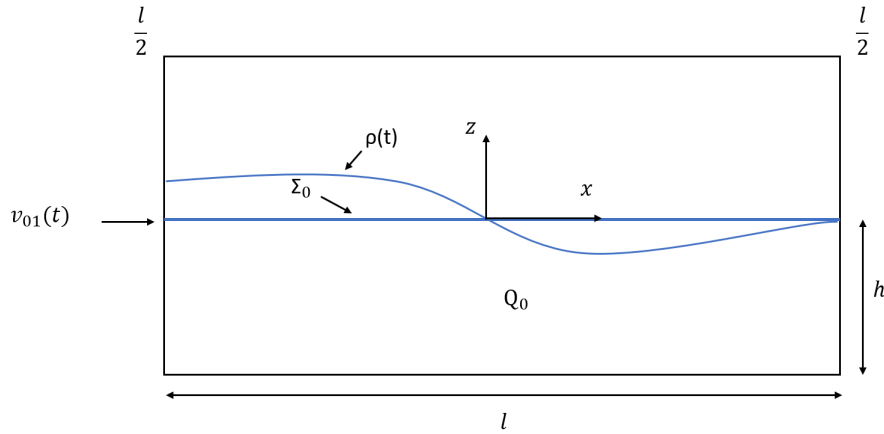
Figure 2.4: 2D rectangular tank with breadth $y \in [-\frac{1}{2}l, \frac{1}{2}l]$, depth h and origin at the surface. $v_o(t)$ is the added velocity. The Neumann condition on the wall shows that the velocity of the tank and is the same as on the wall.

$$
\begin{aligned}
\nabla^2 \Phi &= 0 && \text{in } Q_0 \\
\frac{\partial \Phi}{\partial z} &= 0 && \text{on } z = -h \\
\frac{\partial \Phi}{\partial x} &= v_{01} && \text{on } x = \pm\frac{1}{2}l \\
\frac{\partial \Phi}{\partial z} &= \frac{\partial \zeta}{\partial t} && \text{on } z = 0 \\
\frac{\partial \Phi}{\partial t} &= -g\zeta && \text{on } z = 0 \\
\int_{-\frac{l}{2}}^{\frac{l}{2}} \zeta \, dx &= 0
\end{aligned}
\tag{2.17}
$$

We also need some initial conditions for the problem. The free surface elevation ζ is expressed in terms of a Fourier series. This series satisfies conservation of volume and is given by

$$
\begin{aligned}
z = \zeta(x,t) &= \sum_{j=1}^{\infty} \beta_j(t) \cos(\pi j (x + \frac{1}{2}l)/l) \\
z &= \sum_{j=1}^{\infty} \beta_j(t) f_j(x)
\end{aligned}
\tag{2.18}
$$

Due to Laplace being linear we can superpose the velocity potentials as

$$
\Phi(x,z,t) = v_{01}(t)x + \phi(x,z,t)
\tag{2.19}
$$

Since the first term satisfies the boundary condition in (2.4), we have that ϕ from equation (2.12) also satisfies the zero Neumann boundary condition. A consequence of the natural

sloshing modes satisfying these conditions is that ϕ is a solution of n multiple natural modes $\phi_n(x,z)$

$$\phi(x,z,t) = \sum_{n=1}^{\infty} R_n(t)\phi_n(x,z) \tag{2.20}$$

We have now satisfied all conditions except the kinematic and dynamic free surface condition. In order to fulfill these conditions we insert equation (2.18) and (2.20) into the kinematic boundary condition and get

$$\dot{\beta}_n = \kappa_n R_n = \frac{n\pi}{l}\tanh(\frac{n\pi}{l}h)R_n \tag{2.21}$$

We insert the same equations into the dynamic condition giving the modal system for modal functions β_n in sway motion, which analogues to a mass-spring system without damping.

$$\ddot{\beta}_n + \sigma_n^2\beta = K_n(t) = -\dot{v}_{01}(t)\left[\frac{2}{n\pi}\tanh(\frac{\pi n}{l}h)((-1)^n - 1)\right] \tag{2.22}$$

where $\dot{v}_{01}$ is a function of time and $\left[\frac{2}{n\pi}\tanh(\frac{\pi n}{l}h)((-1)^n - 1)\right]$ of space. This is applicable to any steady and transient sea states, however for irregular sea an empirical damping coefficient should be included to avoid unphysical large responses around the natural period. The added damping is inserted in form of a damping ratio which gives the equation

$$\ddot{\beta}_n + 2\xi_n\sigma_n\dot{\beta}_n + \sigma_n^2\beta = K_n(t) \tag{2.23}$$

where ξ is the damping ratio which will be further discussed in Chapter 2.5. Once β is found, all of the hydrodynamic characteristics can be found like pressure distributions, forces, velocities and amplitudes. The instantaneous force acting on the tank walls, which is found by integrating the pressure over the mean wetted surface is given as

$$F_1 = -m_l\dot{v}_{01} + m_l\frac{l}{\pi^2 h}\sum_{n=1}^{\infty}\ddot{\beta}_n(t)\frac{1+(-1)^{n+1}}{n^2} \tag{2.24}$$

Where m_l is the frozen liquid mass. The sloshing in a closed tank will act as an added mass due to the fact that $\ddot{\beta}$ in equation (2.24) will either be 0 or 180 degrees out of phase with the force. This gives a discontinuity in the phase around the natural sloshing frequency, which is smoothed out when adding a damping term, which will be explained in Chapter 2.5.

2.3.1 General Solution of Linear Modal Theory

The last section presented modal theory for a 2D rectangular tank in forces sway motion. As our model is a circular cylinder, we turn our attention to the general case which also includes pitch motion. By introducing a rotational motion, the linear modal theory can be described in a general fashion as a sum of potentials. When sloshing is studied, a body-fixed coordinate system is most convenient with origin at the mean free surface of the tank. The infinite set of generalized coordinates β_i and $R_i(t)$ is introduced by expansion of the free surface elevation ζ and velocity potential Φ as a series of the natural sloshing terms

$$\zeta(x, y, t) = \sum_{i=1}^{\infty} \beta_i(t)\phi_i(x, y, 0) = \sum_{i=1}^{\infty} \beta_i(t) f_i(x, y) \tag{2.25}$$

$$\Phi(x, y, z, t) = v_0(t) r + \omega(t)\Omega_0(x, y, z) + \sum_{i=1}^{\infty} R_i(t)\phi_i(x, y, z) \tag{2.26}$$

Where the first term is due to the translational motion, the second due to rotational motion and the third is the sum of natural modes. ϕ_i are the natural sloshing modes defined by the eigenvalue problem given in equation (2.12), and $f(x, y) = \phi_i(x, y, 0)$. Ω_0 is the Stokes-Joukowski potential where a fully filled tank is considered under rotational motion. By following the approach presented on page 198 and 199 in *Sloshing* Faltinsen and Timokha (2009), the infinite set of uncoupled linear differential equations for the generalized coordinates β_i is given as

$$\mu_m(\ddot{\beta}_m + \sigma^2 \beta_m) + \lambda_{1m}(\ddot{\eta}_1 - g\eta_5) + \lambda_{2m}(\ddot{\eta}_2 \; g\eta_4) + \sum_{k=4}^{6} \ddot{\eta}_k \lambda_{0(k-3)m} \tag{2.27}$$

where the hydrodynamic coefficients are not dependent on time and can be found separately. The hydrodynamic coefficients are given in equation (5.26) in *Sloshing* (Faltinsen and Timokha, 2009). It is important to note which coordinate system one is working with as well as the sloshing being represented in added mass terms only. The added mass coefficients will be discussed in Chapter 2.7.

2.4 Hydrodynamic Coefficients for an Upright Circular Cylinder

By adapting the general solution of the linear modal theory for 3D upright circular cylinders, as well as using the natural modes described in equation (2.14) with the Stokes-Joukowski potential, we can find the hydrodynamic coefficients for the upright circular cylinder. As mentioned in equation (2.13) and (2.14), we perform the analysis for only the cosine term. Normally, another index is added to separate the cosine and sine term. As the following description follows the indexing of the book, we set the last index to 1.

Equation (2.14) is normalized which simplifies computing elevations at the wall which is common practice, giving a similar equation.

$$\phi_{m,n,1}(r,\theta,z) = R_{m,n}(r)\frac{\cosh(k_{m,n}(z+h))}{\cosh(k_{m,n}h)}\cos(m\theta)$$

$$k_{m,n} = \iota_{m,n}/R_0 \quad \text{and} \quad R_{m,n} = \frac{J_m(k_{m,n}r)}{J_m(k_{m,n}R_0)}$$

$$(2.28)$$

Note, the index i from equation (2.14) is replaced with n. As $r = R_0$ at the tank wall, we have that $R_{m,n} = 1$. We consider $m = 1$ due to the right hand side of equation (2.22) is zero for all except $m = 1$ because of the Stokes-Joukowski potential having uniquely defined cosine component.

For linear theory, surge and pitch are the only motions able to excite sloshing inside the circular structure. We are therefore left with the following equation which is based on the hydrodynamic coefficients given in equation (5.153) in *Sloshing* Faltinsen and Timokha (2009)

$$\ddot{\beta}_{1,j,1} + \sigma_{1,j}^2\beta_{1,j,1} = -P_j(\ddot{\eta}_1(t) - g\eta_5(t) - S_j\ddot{\eta}_5(t)) \tag{2.29}$$

where

$$P_j = \frac{2\iota_{1,j}\tanh(\iota_{1,j}h/R_0)}{\iota_{1,j}^2 - 1}$$

$$S_j = \frac{2R_0\tanh(\iota_{1,j}h/2R_0)}{\iota_{1,j}}$$

$$(2.30)$$

Where $\beta_{1,j,1}$ is the modal function, P_j and S_j are given as constants for each of the j modes.

$\sigma^2_{1,j}$ is the natural frequency for each mode, $\ddot{\eta}_1(t)$ is the acceleration in surge, $\eta_5(t)$ is the pitch motion and $\ddot{\eta}_5(t)$ is the pitch acceleration taken from the experiment. g is the gravitational acceleration. j is dependant on which mode we are considering, meaning $j = 1$ for the first root, $j = 2$ for the second root and so on. The solution can be found using MATLAB built in function ODE45 which solves the second order differential equation numerically which is explained in Chapter 3.3.6

When β is estimated, we use equation (2.25) with $f_{1,n,1} = \phi_{1,n,1}(r,\theta,0) = R_{1,n}(r)\cos(\theta)$ where $\theta = 0$ and $r = R_0$, simplifying the equation to $f_n = 1$. Therefore, equation (2.25) is reduced to

$$\zeta(x, y, t) = \sum_{n=1}^{\infty} \beta_n(t) f_n(x, y) = \beta_n(t) \tag{2.31}$$

Note, the index i from equation (2.25) is replaced with n. This shows the sloshing wave elevation at the front wall inside the structure given prescribed motions of the structure. This can now be compared with experimental data.

2.5   Dynamics of System with One Degree of Freedom

A system with one degree of freedom has only one position parameter moving alone a single axis. The principle is given as a mass attached to an elastic spring. The mass can be excited by an outer force in the direction of the spring and can also contain a damper. The dynamics of a single degree of freedom system with a mass, spring and damper can be described by mass on wheels moving along one axis shown in Figure 2.5.
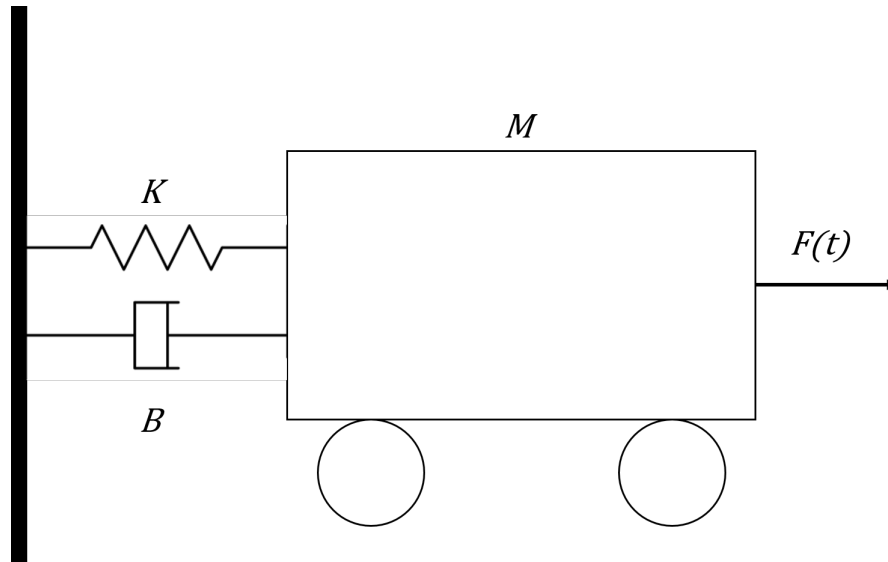
Figure 2.5: 1D mass-spring system where B is damper, K is the stiffness, M is the mass and $F(t)$ is the forcing term.

The motions of a 1 degree of freedom system with a forcing term can be described as

$$M\ddot{x}(t) + B\dot{x}(t) + Kx(t) = F(t) \tag{2.32}$$

where M is the mass of the system, B is the damping and K is the stiffness of the spring. The external load acting on the system is given as a time varying force which can for example oscillate with cosine $F(t) = F_0 \cos(\omega t)$. $\ddot{x}$, $\dot{x}$ and x is the acceleration, velocity and displacement respectively of the system at each given time. We identify the equation as a second order differential equation. The solution is given as homogeneous and particular part.

$$x(t) = x_H(t) + x_P(t) \tag{2.33}$$

The homogeneous solution is found by setting the right hand side of the equation (2.32) to zero $F(t) = 0$, and using some given initial conditions. This part of the solution is called the transient solution due to it dying out after a short period of time. The solution is given as

$$x_H(t) = A\sin(\omega_0 t) + B\cos(\omega_0 t) \tag{2.34}$$

where A and B are constants found by using the initial conditions. The initial conditions are

set as $x(0) = x_0$ and $\dot{x}(0) = \dot{x}_0$ giving

$$x(t) = \frac{\dot{x}_0}{\omega_0} \sin(\omega_0 t) + x_0 \cos(\omega_0 t) \tag{2.35}$$

The particular part for a harmonic system is given as

$$x_P = C_1 \sin(\omega t) + C_2 \cos(\omega t) \tag{2.36}$$

As mentioned, the particular part is the steady state part. By applying x_P to equation (2.32) we get the following equation

$$x_P = \frac{F_0}{\sqrt{(-\omega^2 M + K)^2 - (\omega c)^2}} \sin(\omega t - \beta) \tag{2.37}$$

The total solution is found by superponing the homogenious and particular part. The response amplitude operator can now be defined by the response amplitude by the forcing term

$$|\frac{x_P}{F_0}| = \frac{1}{\sqrt{(-\omega^2 M + K)^2 - (\omega c)^2}} \sin(\omega t - \beta) \tag{2.38}$$

Considering the equation of motion given in equation (2.32) without any forcing term, the natural period of the system can be found. This is the period of which the system will oscillate if set in motion. By inspecting the undamped natural frequency of the system, we find that

$$-\omega_{0n}^2 M + C = 0$$
$$\omega_{0n} = \sqrt{\frac{C}{M}} \tag{2.39}$$

Due to viscous effect and non-linearities, sloshing includes a damping factor. It is therefore reasonable to represent this factor using familiar terms like added mass and stiffness of the system

$$b = b_{cr} = 2m\omega_0 = 2\sqrt{mk} \tag{2.40}$$

In reality, all systems are affected by damping. With no damping, the response at the natural frequency goes to infinity, which is unphysical. This equation is referred to the critical damping and can be utilized to calculate the damping.

$$\xi = \frac{b}{b_{cr}} = \frac{b}{2\sqrt{mk}} \tag{2.41}$$

In order to find the dynamic amplification factor (DAF), we have to define a ratio between a specific frequency and the natural frequency of the system $\beta = \frac{\omega}{\omega_n}$. The DAF using equation (2.38)

$$DAF = \frac{1}{\sqrt{(1-\beta^2)^2 + (2\xi\beta)^2}}$$
(2.42)

The phase angle between force and response can now be computed as

$$\theta = \arctan(\frac{2\xi\beta}{1-\beta^2})$$
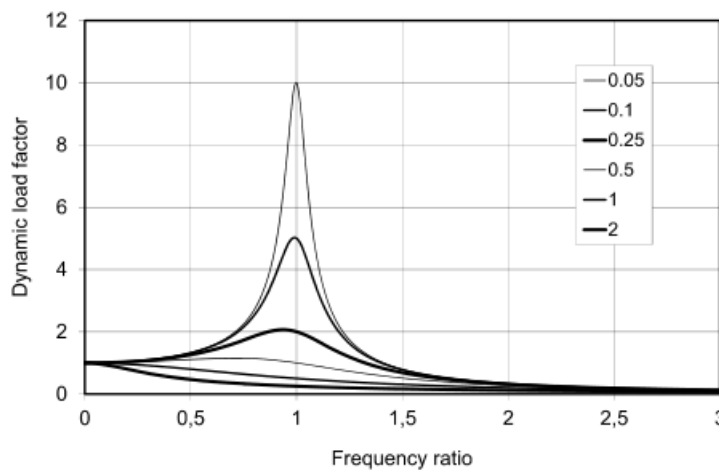(2.43)

The DAF and phase angle can be shown graphically as

Figure 2.7   Dynamic load factor as function of the frequency ratio for given values of damping ratio
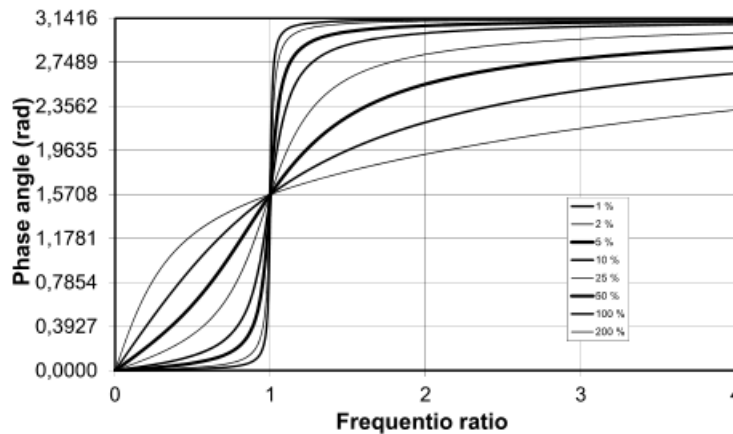
Figure 2.8   Phase angle between load and response as function of the frequency ratio for given values of the damping ratio

Figure 2.6: Figure shows the dynamic load factor (DAF) for different damping ratios and frequency ratios. The corresponding figure for the phase angle θ is given in the lower figure (Larsen, 2014)

2.6   System with Two Degrees of Freedom

In our mode test we have more than 1 degree of freedom due to rotational terms as well. We limit ourselves to only two degrees of freedom which are the most important for linear slolshing. We add another degree of freedom to the model, introducing a second equation of motion. The equations of motion can now be evaluated as a 2×2 matrix. Due to the coupling motion, some extra coupled terms have to be added. The terms are first presented in matrix form giving an overview

$$M + A(\sigma) = \begin{bmatrix} M + A_{11} & Mz_g + A_{15} \\ Mz_g + A_{51} & I_5 + A_{55} \end{bmatrix} \tag{2.44}$$

$$C = \begin{bmatrix} C_{11} & C_{15} \\ C_{51} & C_{55} \end{bmatrix} \tag{2.45}$$

By assuming no damping, the damping term disappears. For a free floating structure, there are no restoring forces in surge, leaving C_{55} as the only stiffness term which is due to the pitch righting moment.

2.6.1   Coupled Motion

Assuming that the motion can be written as a periodic function, $\eta = \eta_a cos(\sigma t - kx)$, the two equations can be set up in matrix form. By deriving $\ddot{\eta}_1$ and $\ddot{\eta}_5$ with respect to time, we get $\ddot{\eta}_1 = -\sigma^2 \eta_{1a} cos(\sigma t - kx)$ and $\ddot{\eta}_5 = -\sigma^2 \eta_{5a} cos(\sigma t - kx)$. The equation can be now written as

$$\begin{bmatrix} -\sigma^2(M + A_{11}) & -\sigma^2(A_{15} + M_{15}) \\ -\sigma^2(A_{51} + M_{51}) & -\sigma^2(I_5 + A_{55}) + C_{55} \end{bmatrix} \begin{bmatrix} \eta_{1a} \\ \eta_{5a} \end{bmatrix} = \begin{bmatrix} F_{1,ex} \\ F_{5,ex} \end{bmatrix} \tag{2.46}$$

$$\begin{bmatrix} -\sigma^2 \tilde{a}_{11} & -\sigma^2 \tilde{a}_{15} \\ -\sigma^2 \tilde{a}_{51} & -\sigma^2 \tilde{a}_{55} + C_{55} \end{bmatrix} \begin{bmatrix} \eta_{1a} \\ \eta_{5a} \end{bmatrix} = \begin{bmatrix} F_{1,ex} \\ F_{5,ex} \end{bmatrix} \tag{2.47}$$

Note, the added mass terms have been shortened to $\tilde{a}_{ij}$. A solution to this system of equations is found by evaluating the determinant of the first matrix giving a non-trivial solution

with multiple solutions for the natural frequency σ_n of the coupled system.

$$\sigma^4[\tilde{a}_{11}\tilde{a}_{55} + \tilde{a}_{15}\tilde{a}_{51}] - \sigma^2\tilde{a}_{11}C_{55} = 0 \tag{2.48}$$

We can now either solve for σ or plot the 4th order polynomial to see where function crosses the x-axis. The roots of the function that have a valid solution, give the natural frequency of the coupled system. A system with and without sloshing will have a shift in natural frequency due to multiple added mass terms being added.

2.7   Brief Introduction to the Response of Sloshing

We start off by assuming regular incident waves of small wave steepness and that the linear dynamics motions oscillate harmonically with the same frequency as the exciting wave loads. Following the notation of Faltinsen (1990), the hydrodynamic problem is split into two subproblems

1. Forces and moments on the body when the body is restrained from motion with incident regular waves. These hydrodynamic loads are the so called Froude-Krillof and diffraction forces and moments.

2. The forces due to forced oscillation with the wave excitation frequency in any rigid-body motion. In this mode, we do not consider any incident waves. The hydrodynamic loads are the so called added mass, damping and restoring terms.

Due to the linear assumptions, subproblem 1 and 2 can be superponed. The equation of motion for rigid body-motion is the same as give in the equation (2.32). The sum of forces on a body is given as

$$\sum F = F_{ex} + F_{HD} \tag{2.49}$$

where the sum of forces consists of excitation forces and hydrodynamic forces which come from the super-positioning.

Up until now we have considered the body to be a solid body. However, when we introduce

a free surface inside the structure which can slosh about, we have to split the hydrodynamic problem into an outer and inner problem. The inner problem consists of the sloshing forces and moments, and the outer problem consists of the problem described above. Equation (2.49) receives an additional term F_{inner}

$$\sum F = F_{ex} + F_{HD} + F_{inner} \tag{2.50}$$

F_{inner} includes the sloshing terms which are split into a solid part and floating part. The effect of sloshing is represented in terms of added mass when studying the interaction between steady-state sloshing and the structure. The sloshing added mass coefficient is represented for three cases

1. The liquid inside the structure is frozen and is considered as a solid body.

2. The tank is completely filled with liquid.

3. A free-surface is present with linear sloshing.

The sloshing effect in rotational motion pitch and transitional motion surge are treated slightly different. However, this brings the total added mass coefficient due to sloshing to

$$A_{i,j} = A_{i,j}^{filled} + A_{i,j}^{slosh} \tag{2.51}$$

2.7.1   Surge

In surge motion, the filled added mass term is given as the frozen liquid added mass acting as a solid body given as $A_{11}^{frozen} = A_{11}^{filled} = M_l$. Due to the free-surface inside the model, the linear sloshing added mass must be included. This is done by adding another added mass term which is called A_{11}^{slosh} given in equation (2.51). The sloshing terms are long and tedious and can therefore be found in Faltinsen and Timokha (2009) on page 209 and 210. They sum over the set of the roots of the derivative of the Bessel function.

2.7.2 Pitch

The pitch problem is similar to the surge problem which also includes a frozen and sloshing added mass. However, the frozen term is defined slightly different. In pitch motion, the water volume inside the structure cannot be treaded as a frozen liquid solely. Even with a fully filled tank, the water will move around in pitch motion. Therefore water cannot be treated as a rigid mass. To correct this, a so called Stokes-Joukowski term is added to A_{55}^{filled}.

$$
\begin{aligned}
A_{55}^{frozen} &= \sigma^{-2} M_l g z_g + I_{22}^0 \\
A_{55}^{filled} &= A_{55}^{frozen} + (J_{022}^1 - I_{22}^0) \\
A_{55}^{filled} &= \sigma^{-2} M_l g z_g + J_{022}^1
\end{aligned}
\tag{2.52}
$$

The last term is the Stokes-Joukowski potential which replaces the original stress tensor. As mentioned, the sloshing added mass terms can be found on page Faltinsen and Timokha (2009) on page 209 and 210.

Model Tests

One set of model tests was performed during the present work. The experiment was performed in October and November 2016 at NTNU's Lilletanken at Tyholt during the specialization project. The experiment consisted of a moored floating circular cylinder with water filled inside representing a closed fish farm structure. The model was subjected to incoming linear waves. The aim of the experiment was to investigate the effects of sloshing inside a closed fish farm structure for full scale range of periods $\in$ [3.6 - 7.2] s with three different steepness $H/\lambda = 1/30$, $1/45$ and $1/60$. This experiment sets a foundation for comparison of theoretical calculations and experimental results. The model was horizontally anchored to the side walls using linear spring as shown in Figure 3.2 which allowed the model to move ideally in only two degrees of freedom, namely surge and pitch. The purpose was firstly to investigate a full scale floating fish farm structure exposed to waves and secondly build a foundation for theoretical sloshing calculations using linear sloshing theory.
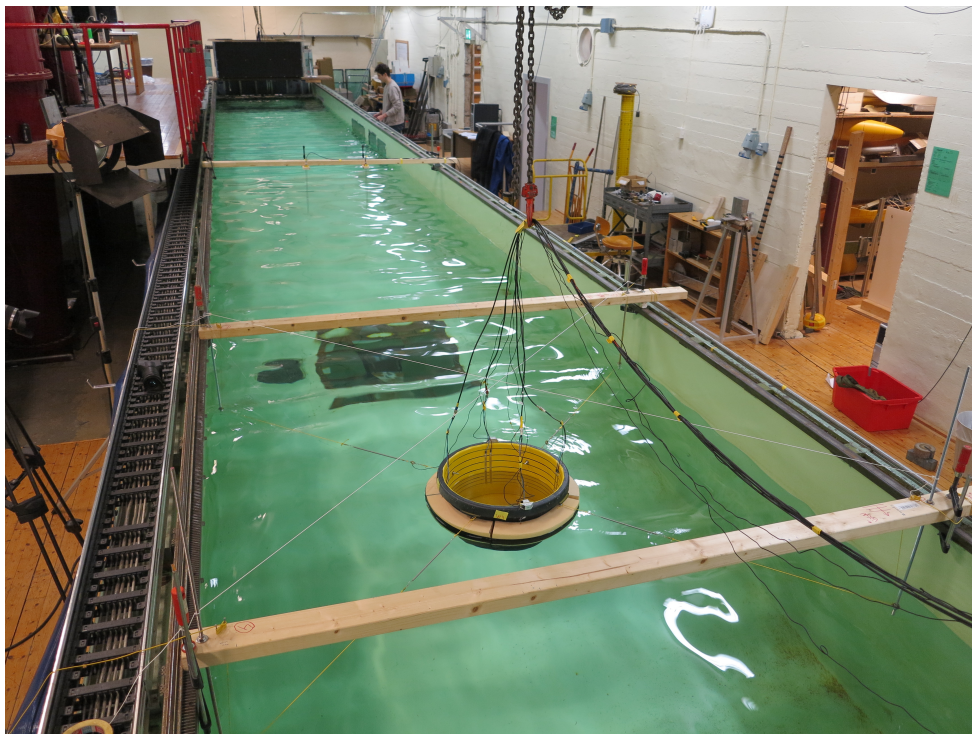
Figure 3.1: Illustration of final setup of the model test performed at NTNUs Lilletanken. The snapshot shows the model with a floating collar, anchoring and sensors as well as the wave maker at the far end of the basin.

The first section presents the performed model test in detail with a schematic drawing including all of the main dimensions. This is followed by a description of the instrumentation, modifications of the model, test matrix and conditions. Futher, a discussion of error sources including sensor errors and wall effects is presented. The procedure of data-acquisition from the model test to presentable results is also described. Lastly, the description of sensitivity analysis approach is explained.

3.1 Wave Excitation Experiment

The performed model test was conducted at the small towing tank called Lilletanken at Marine Technology Centre at NTNU. The model was chosen due to close approximation of a full scale closed structure and availability of materials. The full geometry of the tank and model are presented in table 3.1. The full scale period ran ranges from T ∈ [3.2 - 7.8]s corresponding to periods surrounding the eigenperiod of sloshing. The full scale comparison structure had a diameter of D ≈ 40 m and height H ≈ of 20 meter, giving a diameter to height ratio D/H ≈ 2. The bucket used as a model had a varying diameter along the height, which is neglected firstly. The depth of the tank in full scale corresponds to deep water approximation.
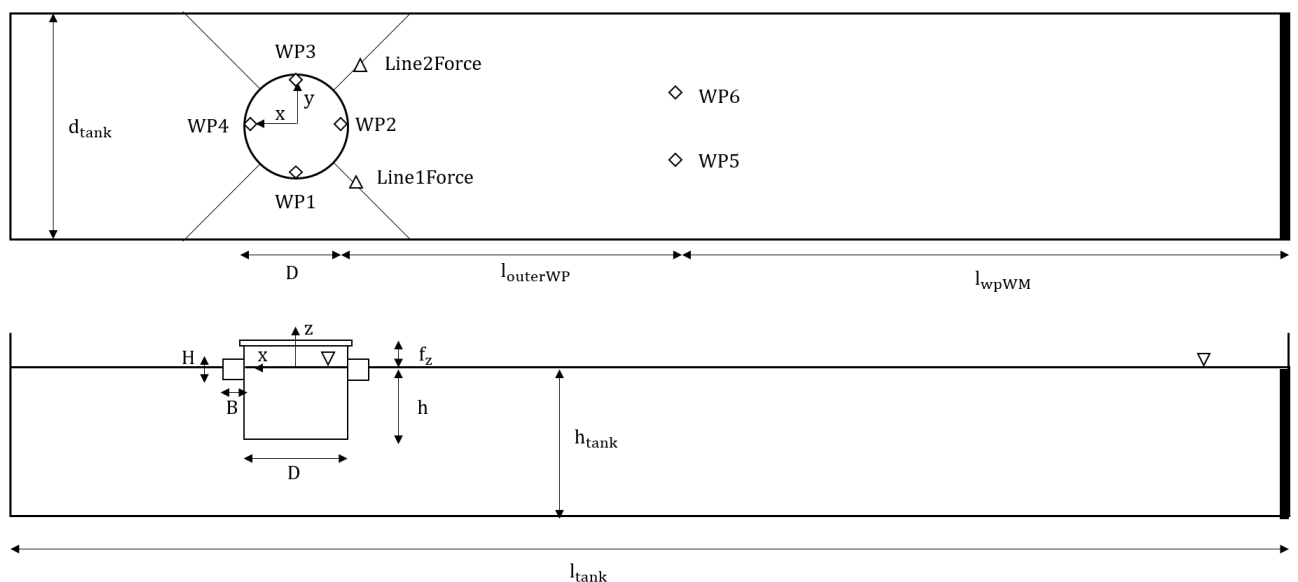
Figure 3.2: Schematic illustration of the model test performed in the towing tank Lilletanken from the side and top. The wave maker is illustrating with a thick black line at the right hand side of the schematics. See Table 3.1 for the full description of quantities and 3.3 for the description of sensors.

The model scale was chosen to be 1:81 due to approximation of a full scale unit and for convenience when operating with Froude time scaling $\sqrt{\lambda} = 9$ where λ is the scaling factor. The main parameters and tank dimensions are given in Table 3.1. The wave steepness and incoming wave period was varied during the test, with 100 waves for each given period. The model was placed on the far side of the wave maker to and moored at the free surface using a wooden structure shown in Figure 3.1.

Table 3.1: List of main dimensions of the full scale structure used in the model test given for full scale and model scale 1:81. Full scale dimensions are based on a typical size of fish farm structures on the market

Quantity	Term	Full scale	Model scale 1:81
Model diameter [m]	D	40.5	0.483
Water level [m]	h	19.2	0.237
Draught [m]	d = h	20	0.237
Freeboard [m]	f_z	11.58	0.143
Breadth collar [m]	B	6.5	0.08
Height collar [m]	H	6.5	0.08
Tank depth [m]	h_{tank}	81	1
Tank breadth [m]	d_{tank}	226.8	2.8
Tank length [m]	l_{tank}	2025	25
Basin wave probes to wave maker [m]	$l_{outerWP}$	482	5.95
Basin wave probes to center of model [m]	l_{WPWM}	1249	15.43
Total model weight [kg]	M	30983010	58.3

The experiment was performed in the towing tank by controlling the wave maker wave period and wave steepness input. The parameters were entered using a MATLAB-script that transform input data to a signal for the wave maker. Three steepnesses run with different periods are shown in the test matrix in Table 3.2 with values in full-scale. T is given in seconds.

3.1.1 Conditions, Measurement and Instrumentation

The model was constructed using a standard 65 L plastic bucket from the local hardware store. The model was retrofitted with anchoring hooks, painted yellow and fitted with floating collar to ensure stability. Two 5 kg steel blocks were placed at the bottom of the bucket to weight it down, lowering the center of gravity. With a floating collar and weights, the model draught was at half of the collar shown in Figure 3.1. The model is exposed to a series of wave

periods with 3 different wave steepnesses. In total, for each steepness, 81 series of periods ranging from T ∈ [3.2 - 7.8]s in fullscale consisting of 100 waves each were generated, making up 243 series. The total run-time was estimated to around 17 hours, with a logging frequency Hz = 50, the total length of the measuring vector consisting of around 3×10^6 values. The size of the model also ensured that natural sloshing period is within the wave makers threshold. The test matrix is shown in Table 3.2

Table 3.2: Test matrix used for the experiment showing all input data, including start period, end period, time step, steepness, steepness step, amount of waves per series and waiting time, to the wave maker in full scale. T is given in seconds.

	T_{start}	T_{end}	ΔT	$(H/\lambda)_{min}$	$(H/\lambda)_{max}$	$\Delta(H/\lambda)$	N_{waves}	T_{wait}
Setup	3.6	7.2	0.045	60	30	15	100	180

The input file included a ramp up of the wave maker which increased from 0 to a given amplitude linearly. It was chosen that the wave maker takes 10 periods before reaching the desired amplitude, with 100 oscillations before the ramp down was initiated. The time between the series was set to 180 seconds to let the tank water surface settle down before the next wave series was run.

The model was fitted with internal wave probes, accelerometers and force transducers at the anchoring lines listed in Table 3.3. The strain gauges are shown in the upper left of Figure 3.3, the wave probes inside the model are shown in the upper right part of Figure 3.3, the x- and z-accelerometers are shown in the lower left part and the wave probes outside the model are shown in the lower right part of Figure 3.3. The wave probes in front of the model were placed to measure the actual incoming wave height. With two probes, the average could be found. There were four probes inside the model, one starboard, one freeboard, one fore and one aft. The sensors were calibrated and tested by NTNUs staff beforehand and were kept like this for the entire experiment.
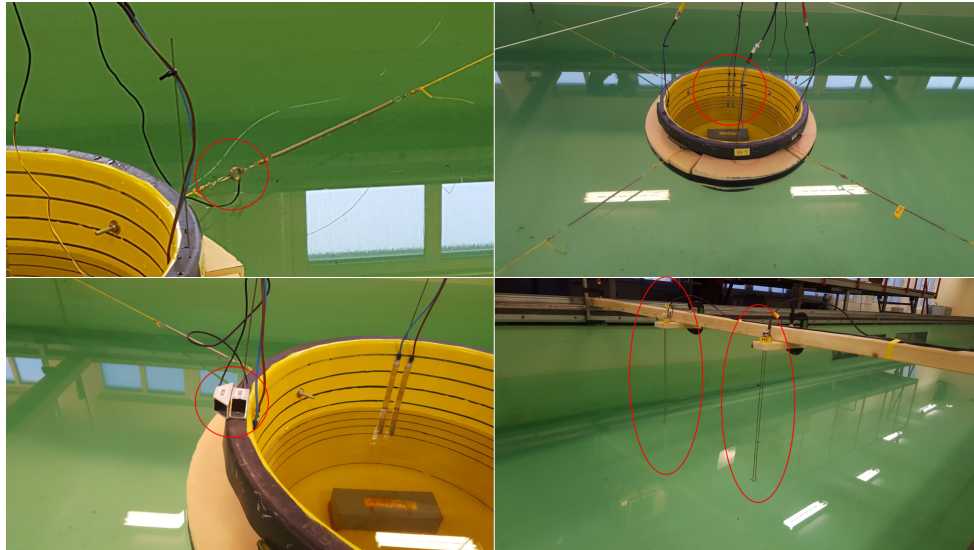
Figure 3.3: Upper left: Anchoring strain gauges. Upper right: Wave probes inside model. Lower left: Accelerometer in Z and X direction. Lower right: Wave probes in basin.

The sensor names in Figure 3.2 are listed in Table 3.3 describing all the measuring instruments. The acceleration gauges followed the body and are consequently evaluated in a body-fixed coordinate system.

Table 3.3: Strain gauges on mooring lines, wave probes inside and outside of the model and accelerometers in horizontal and vertical direction applied in the experiment.

Sensor name	Description
Line1Force	Fore anchoring line force starboard
Line2Force	Fore anchoring line force portside
WP1	Wave probe starboard
WP2	Wave probe front
WP3	Wave probe portside
WP4	Wave probe aft
WP1basin	Wave probe basin 1
WP2basin	Wave probe basin 2
AccZ1	Accelerometer front z-direction
AccZ2	Accelerometer back z-direction
AccX	Accelerometer x-direction

The sensors were calibrated by the NTNU staff beforehand. The calibration was done by measuring output voltage when applying known parameters like weight or water depth. The sensors were calibrated using linear relation $y = ax + b$ where a is the calibration factor which is gives a relation between the applied load or water depth and output voltage. b is just the zero-point which is used to reset the calibration.

The wave probe calibration was done by filling the model to a known water height and measuring the average voltage over time. With a couple of steps, a linear relation could be established such that one relates the output voltage to the water depth. The same was done with force transducers, only that know weights are applied. The accelerometers were borrowed from MARINTEK and precalibrated. This was done by NTNU staff and will not be written in detail in this report.

3.2 Error Sources

Tilted walls of the bucket vary the diameter from 48 cm to 42 cm, making up for 12.5 % in diameter difference. The question is whether this has an effect on the sloshing eigenfrequency and amplitudes of sloshing. The tilted walls can act as run-ups which may increase the amplitudes or introduce non-linearities.

As discovered in the specialization project, the attached collar height is 6.5 meters in fullscale, with the free surface at half of this height. The largest pitch motions correspond to 2 meters in pitch with a 2.65 meters dip at the collar edge. This means that incoming waves larger than 1.5 meters break over the collar, introducing non-linearities. Figure 3.4 illustrates the collar dipping at the rear of the model under the largest waves for steepness $H/\lambda = 1/30$.
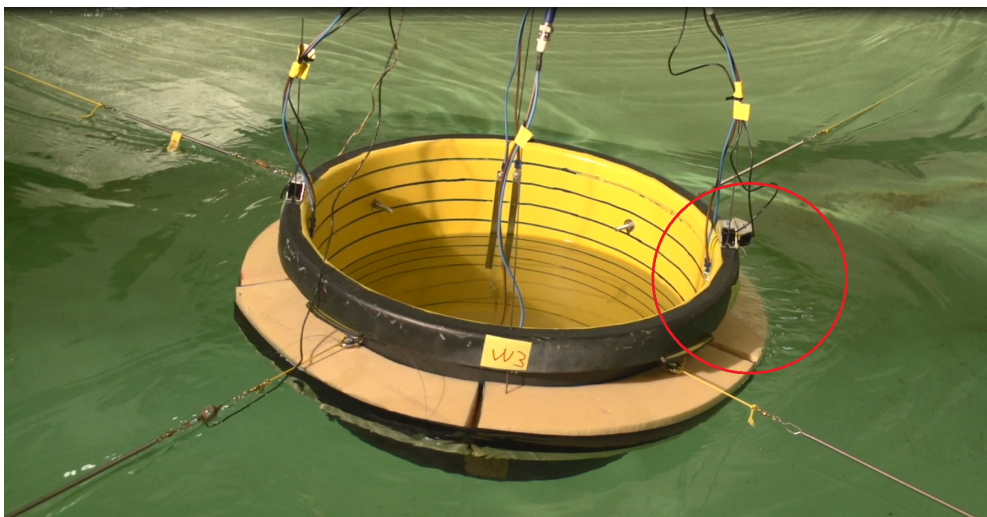
Figure 3.4: Model test for the longest wave period T = 7.2 full scale for steepness 3 ($H/\lambda = 1/30$). The incoming waves travel from left to right. There is visible collar dipping at the rear of the model hightlighted with a red ring.

The non-linear effect called swirling can occur if there is a slight offset of the movement along the longitudinal axis. The wave probes at starboard and port side can detect the swirling if there is a phase change between the fore and aft probes and side probes. Figure 4.18c in Chapter 4.5.1 shows indications of swirling. This will be further investigated in that Chapter.

Since the model has no constrictions of movement, it is in theory free to move in all 6 degrees of freedom, which can impact the assumptions of motions in only pitch and surge. For example, heave motion is excluded from linear sloshing theory and is connected to non-linearities. This will be discussed later under in the results in Chapter 4.

The incident waves are set by the input file to the wave maker, however they did not always match the given wave steepness, therefore the incident wave measured on the wave probes in the water are used which give a much more accurate reading.

We assume potential theory when estimating sloshing, however, due to sharp corners and sometimes large movements, vortex shedding at the corners or other viscous effects may occur.

The accelerometers and wave probes were only calibrated once before the experiment as well as only one successful run was performed. Therefore, it is unknown how accurate the measuring sensor are and if they somehow deviated from their original calibration. An example is the strain gauge, which is located between the anchoring line and spring modelling the anchoring stiffness near water free surface. For higher waves where the model pitched, it was noticed that the gauge dipped into the water, changing the temperature drastically. This might have an effect on the read-outs.

3.2.1   Wall Effects

Wall reflections are an important source of error. The wave reflecting from the model onto the walls and back can introduce unwanted excitation of the structure. Figure 3.5 shows the side of the collar dipping at the exposure to the largest wave for the highest steepness. Towards the ramp-down of the steepness and longest wave sequency as the model settled, a very noticable heave motion was excited.
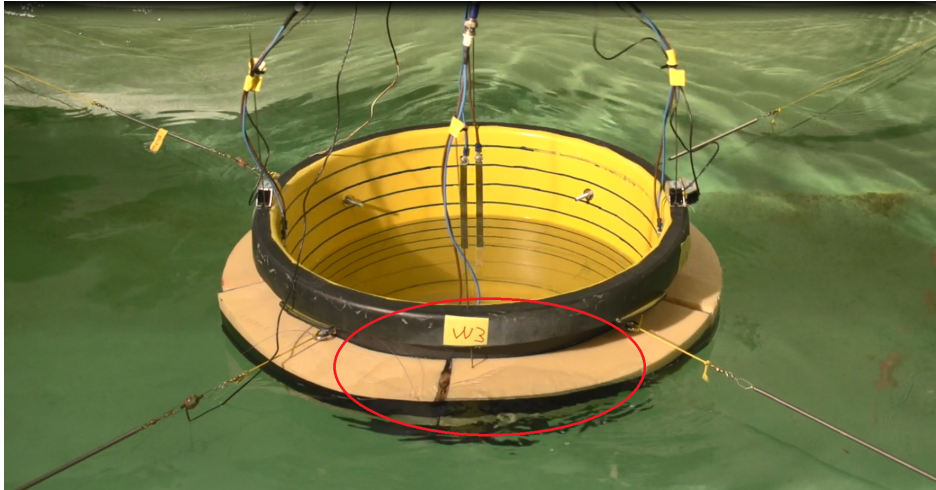
Figure 3.5: Model test for the longest wave period T = 7.2 full scale. The incoming waves travel from left to right. There is visible collar dipping at the side of the model hightlighted with a red ring. The reflected waves from walls induce heave motion

A similar model test was performed by SINTEF Ocean in Trondheim. The project is called SJØFLO and was funded by *The Norwegian Seafood Research Fund* (FHF) . The goal was to investigate sea characteristics of different types of closed fish farm structures (SINTEF, 2017). Per Christian Endresen performed a WAMIT analysis of a closed fish farm structure with and without tank walls to compare how the reflections would affect the heave RAO of the structure.
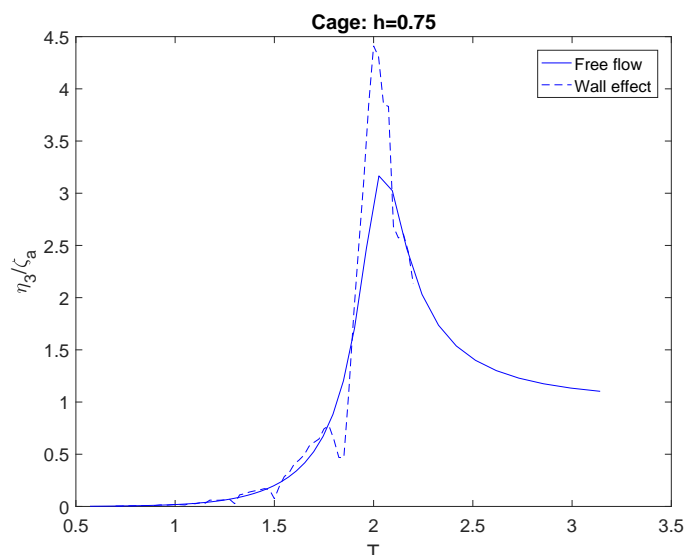
Figure 3.6: Heave RAO of a closed fish farm cage with model scale diameter D = 1.5 m and water depth h = 0.75 m, having the same D/h ratio as our model test. The RAO calculation was performed by Per Christian Endresen for the SINTEF SJØFLO project (SINTEF, 2017). His permission was given to include this plot in the thesis. The Figure is in model scale and T is given in seconds.

The presented heave RAO shows that wall effects have a considerable effect on the RAO, increasing the RAO from 3 to 4.5 at the period giving the largest response at around 2 seconds in model scale. Therefore, the reflecting waves from the wall can have an large effect on the RAO in our mode test, especially in heave.

3.3   Analysis Preparations

All data from the experiment is captured and stored. The data has to be extracted and processed in order to be prepared for analysis. The data from the experiment is extracted from a .bin file and sorted into vectors with specific names in MATLAB. The extracted data contains the time vector, accelerations in x- and z-direction, wave probe measurements and forces.

Each of the sensors presented in Table 3.3 collects data continuously over the course of the entire run, adding up to around 17 hours of data. The post-processing of raw data is performed using MATLAB. The purpose of this section is to describe and give the reader an understanding of the data processing and preparations of the results.

3.3.1   Time-Series

The model test was performed continuously measuring all 81 periods over 3 steepnesses. All of the channels measure continuously making it useful to visually inspect the data. The data is divided into 3 large sets for each steepness. Each set is sliced into 81 smaller time-series per period. From the sliced time-series, a range of 20-50 waves are considered. The evaluated range of the sliced time-series considers time of travel of the incoming waves based on its group velocity c_g. The amount of ramp up waves are also considered to extract the wanted waves.

Figure 3.7 illustrates the total time series of WP2 in full scale, showing an increasing amplitude at the same spot for the three steepnesses. Underneath we find the time series of the mean of WP5 and WP6 which are the wave probes in the basin. The linearly increasing wave amplitude for all three steepnesses is presented.
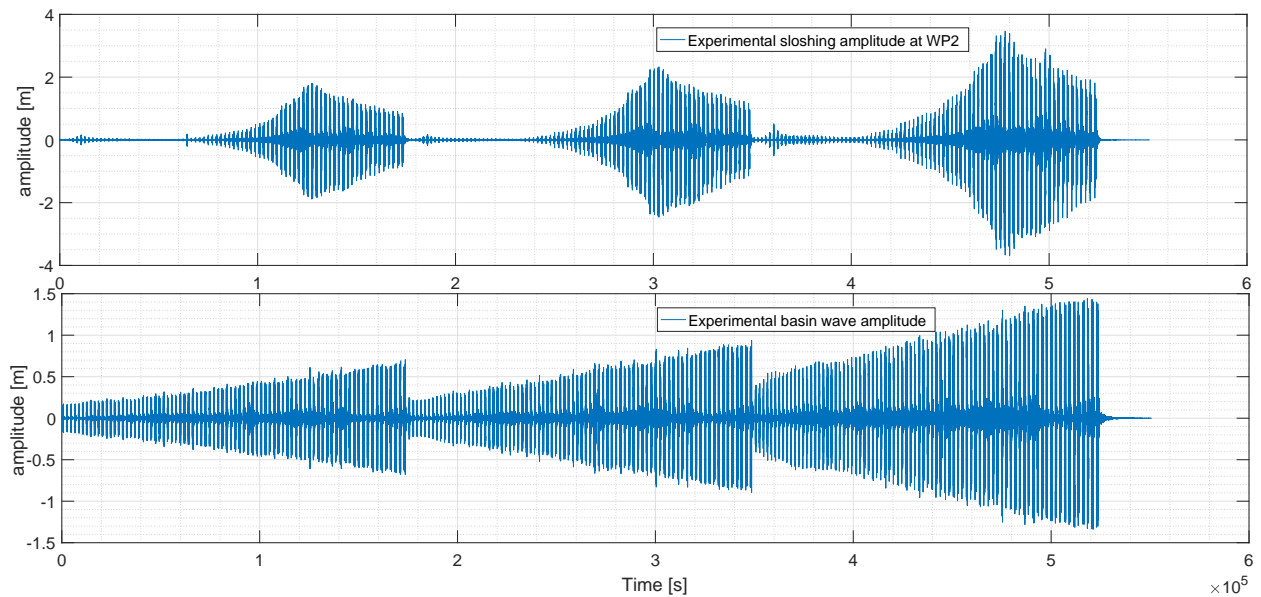
Figure 3.7: Above: Total time series of wave probe 2 over the course of 81 periods and 3 steepness in full scale. Below: Total time series of the mean of wave probes 5 and 6 over the course of 81 periods and 3 steepness in full scale.

3.3.2 Filtering

The raw data from the experiment is visually sound, which points towards low noise disturbance. However, the data seemed to wander off-center, meaning the data has to be moved to the zero point. This is solved by running the raw data through a digital filter in MATLAB.

The digital filter applied is a bandpass Butterworth filter, which solves the problem of phase shift occuring for real time filtering. Figure 3.8a show the filtered data where one can note the slight off-center wandering of the mean value.
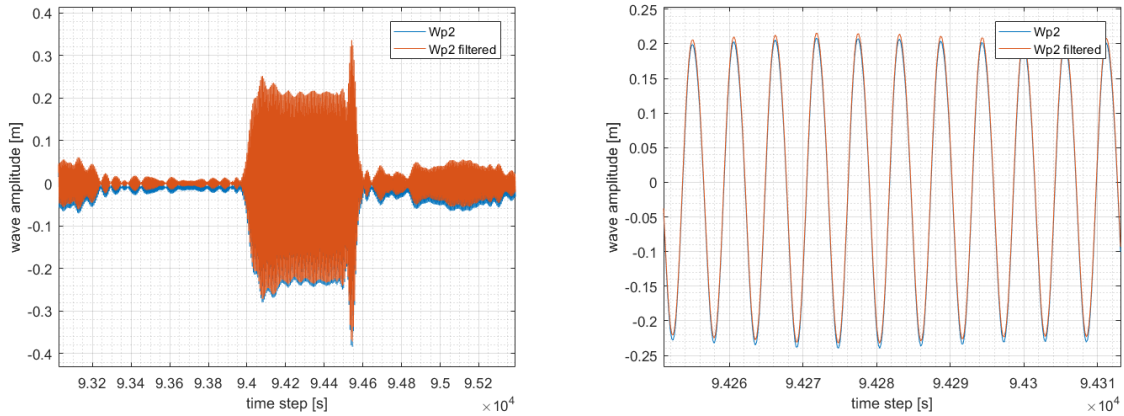
(a) The red shows raw data of sloshing amplitude at WP2, the blue shows filtered data of of sloshing amplitude at WP2 for a time-series.

(b) This Figure presentes a closer look at the filtered and non filtered data from the inner wave probe WP2. The filtering averages the data about 0.

Figure 3.8: An example of real data from the experiment showing how the data is filtered.

The Butterworth filter requires a normalized cutoff frequency which is combined with Nyquist frequency.

$$f_{nq} = \frac{f_{samp}}{2} = \frac{1}{2h} \tag{3.1}$$

where h is the time step of the unfiltered signal. The advantage of using the Nyquist filtering is that it gives a minimal amount of samples needed in order to avoid a phenomenon called fold-back.

The harmonics are extracted by performing a band pass filtering of Fast Fourier Transform (FFT) of the raw signal. An example showing extraction of the first harmonic from the FFT of the sloshing amplitude at the sloshing natural frequency $\omega = 0.93$ is shown in Figure 3.9. The FFT of the signal shows three distinct tops a the frequency 1.3 Hz, at the double frequency 2.6 Hz and a small top at the triple frequency Hz = 4.1. The red color represents the included Fourier components in the band pass filtering (marked with a green frame)
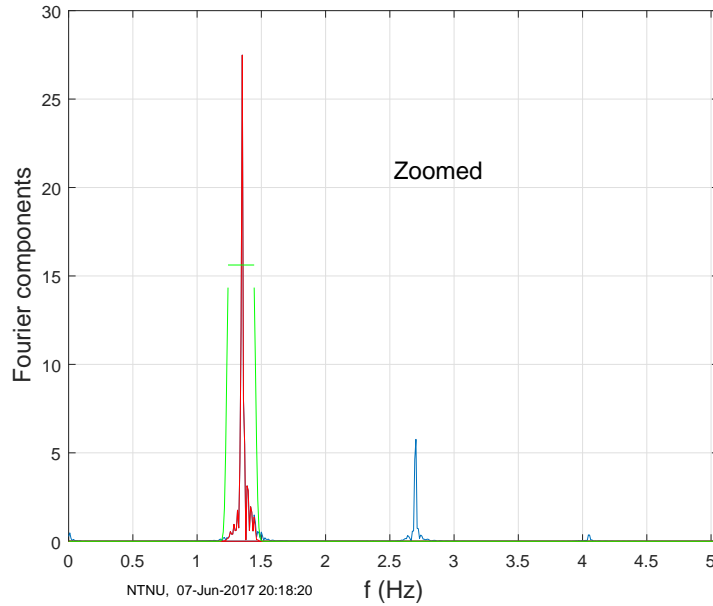
Figure 3.9: A Fast Fourier Transform (FFT) of the raw sloshing amplitude signal at the sloshing natural frequency $\omega = 0.93$. The x-axis is given in model scale Hz. The Figure shows the first, second and third harmonics as the tops for f, $2f$ and $3f$. The green frame illustrates the band pass filter around the first harmonic of the signal.

The three visible tops correspond to f, $2f$ and $3f$ which are the 1st, 2nd and 3rd harmonic of the signal. By performing the FFT, the second and third order effects can be detected as distinct tops at $2f$ and $3f$.

3.3.3   Rigid Body Motion

The total of three accelerometers where used to measure the accelerations of the model exposed to incoming waves. The accelerometers are shown in the scheme in Figure 3.10. Accz1 and Accz2 measure the vertical accelerations, while Accx1 measure the horizontal acceleration. Due to the placement of the vertical accelerometers being placed a certain distance from the rotational center, it was possible to calculate the pitch acceleration of the model as defined in the following equation

$$\ddot{\eta}_5 = \frac{acc_{z1} - acc_{z2}}{L_z} \tag{3.2}$$

Where L_z is the distance between the accelerometers. Using the vertical accelerometers, the heave acceleration can also be extraced by using

$$\ddot{\eta}_3 = \frac{1}{2}(acc_{z1} + acc_{z2}) \tag{3.3}$$

We assume that the motions and acceleration of the model are harmonic functions due to the model being exposed to harmonic incoming waves. This means that for an arbitrary harmonic function it is possible to extract the acceleration by the double derivative of the motions

$$\theta = a\cos(\omega t)$$
$$\ddot{\theta} = -a\omega^2 \cos(\omega t) \tag{3.4}$$

Where a is the amplitude. The angular motion is therefore found by multiplying the acceleration with $-\omega^2$, which then leads to the corrected horizontal acceleration of the model given in equation (3.6).

3.3.4 Coordinate System Correction

The accelerometers are fitted at the top collar of the model with the two accelerometers pointing upwards measuring pitch acceleration, and one at the aft pointing with the wave direction in order to measure surge acceleration as shown in Figure 3.10.
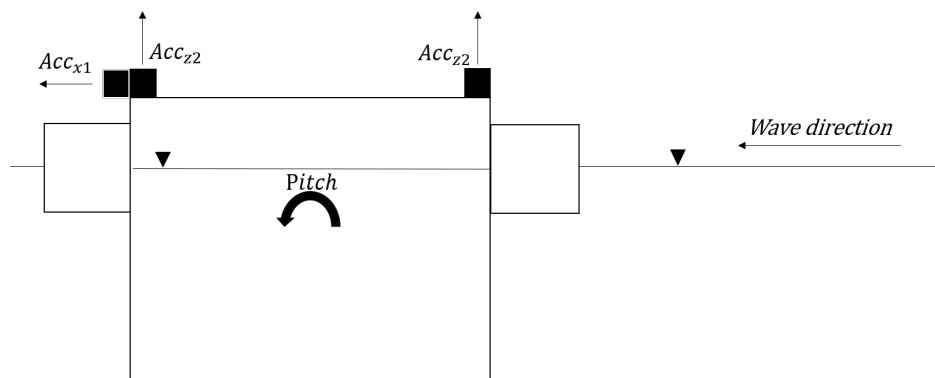
Figure 3.10: All three accelerometers and their measurement direction are given in the schematics. The waves travel from right to left. The pitch is defined as positive in counterclockwise direction.

The accelerometers are attached to the model at the top of the collar. In order to compare

experimental data with the numerical calculation, we have to use the same coordinate system. Therefore, the coordinate system had to be moved as shown in Figure 3.11, meaning the rotational direction has to be reversed as well as the surge direction as presented in equation (3.5). We are still operating in body-fixed coordinates.
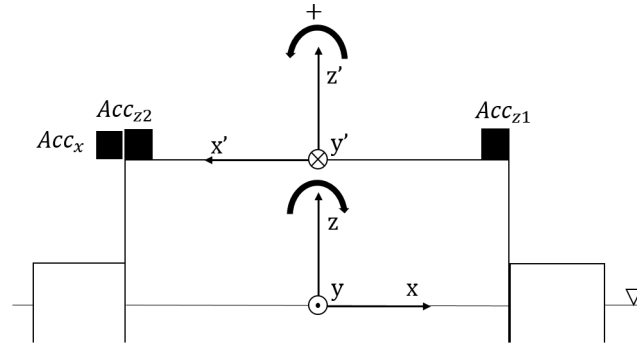
Figure 3.11: The coordinate system is turned around and moved downwards to the free surface inside the model in order to match the coordinate system presented in the sloshing theory. This makes the comparison of experimental and numerical data much easier.

The corrections are presented in equation (3.5), where *exp* are the measured values and *corrected* the corrected values. After this section, the corrected surge and pitch values will only be referred to as $\ddot{\eta}_1$, $\ddot{\eta}_5$ and η_5.

$$\eta_{5corrected} = -\eta_{5exp}$$
$$\ddot{\eta}_{5corrected} = -\ddot{\eta}_{5exp} \quad (3.5)$$
$$\ddot{\eta}_{1corrected} = -\ddot{\eta}_{1exp}$$

The coordinate system for the theoretical calculations is placed at the free surface inside the model. Therefore, the surge acceleration in the new coordinate system is smaller due to a shorter distance from the rotational axis, and has therefore to be corrected as shown in Figure 3.11. Another correction has to be added due to the gravitational acceleration that the acceleration sensor measures when tilted.

$$\ddot{\eta}_{1corrected} = \ddot{\eta}_{1exp} + g\eta_5 - f_z\ddot{\eta}_5 \quad (3.6)$$

where g is the gravitational acceleration and f_z is distance between the free surface and top of the model. Figure 3.12 shows how the g-term contributes to an altered surge acceleration.
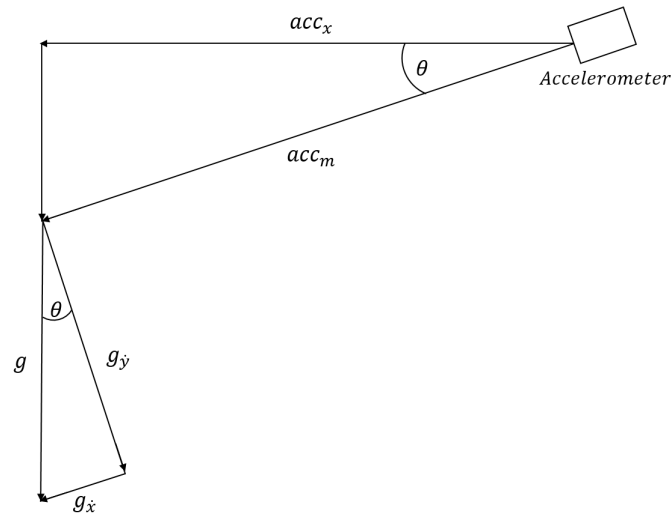
Figure 3.12: Figure shows the added acceleration due to gravity and how it is removed from the measured surge acceleration. θ is the pitch angle.

3.3.5   RAO and Phases

Once the motions are recorded and obtained, it is possible to calculate the transfer function for the model properties and sloshing. All RAOs and phase angles are evaluated for the incoming wave amplitude. The pitch RAO was made dimensionless by adding the dispersion relation k in the denominator of the equation. The following formulas are used to calculate the RAOs for heave, surge, pitch and sloshing amplitude at wave probe 2 (WP2) respectively

$$
\begin{aligned}
H_1(\omega_j) &= \left| \frac{\eta_1}{\zeta_a} \right| \\
H_3(\omega_j) &= \left| \frac{\eta_3}{\zeta_a} \right| \\
H_5(\omega_j) &= \left| \frac{\eta_5}{k\zeta_a} \right| \\
H_{slosh}(\omega_j) &= \left| \frac{\zeta_{slosh}}{\zeta_a} \right|
\end{aligned}
\tag{3.7}
$$

where η_1, η_3, η_5, ζ_a and ζ_{slosh} are found using methods described in the previous subsections.

The phase angle between the theoretical sloshing amplitude found using linear sloshing theory, and the measured sloshing amplitude at WP2 is calculated using a Fourier transform, where complex argument of the signal is the phase offset from the regular sinusoid for that

signal. By applying this method to both signals, the phase difference between them is possible to find.

3.3.6 ODE45

To solve the ordinary differential given in equation (2.29) for β, a MATLAB ODE-solver is used which uses 4th-5th order Runge Kutta numerical method. This is the ODE45 solver which is a nonstiff differential equation solver. The solver requires a first order differential equation input. Since our β is a second order differential equation, we transform the second order equation into a first order equation. To recap, the modal function in question is

$$\ddot{\beta}_{1,j,1} + \sigma_{1,j}^2 \beta_{1,j,1} = -P_j(\ddot{\eta}_1(t) - g\eta_5(t) - S_j\ddot{\eta}_5(t)) \tag{3.8}$$

where we rewrite it into a first order equation and set the right-hand side of the equation to $RHS = -P_j(\ddot{\eta}_1(t) - g\eta_5(t) - S_j\ddot{\eta}_5(t))$ for convenience

$$\begin{aligned}
\ddot{\beta} + \sigma_n^2 \beta &= RHS \\
\beta_1' &= \beta_2 \\
\beta_2' &= RHS - \sigma_n^2 \beta_1
\end{aligned} \tag{3.9}$$

Due to the limitations of linear modal theory, a beating pattern may occur. Therefore, the third equation in used equation (3.9) is given as

$$\beta_2' = RHS - \sigma_n^2 \beta_1 - 2\sigma_n \xi \beta_2 \tag{3.10}$$

Where we set the damping ratio ξ to 0.01 which is 1 % of the critical damping. By introducing this factor, the beating signal will be damping and a steady state solution will be reached.

The solver regulates the time step by itself, meaning some of the solutions can be in between the logging steps of 50 Hz. To compensate for this, a linear interpolation function is added which interpolates between the logged values if needed, as illustrated in an example in Figure 3.13. These values are not taken from the experiment, they are only generated to show the interpolation scheme.
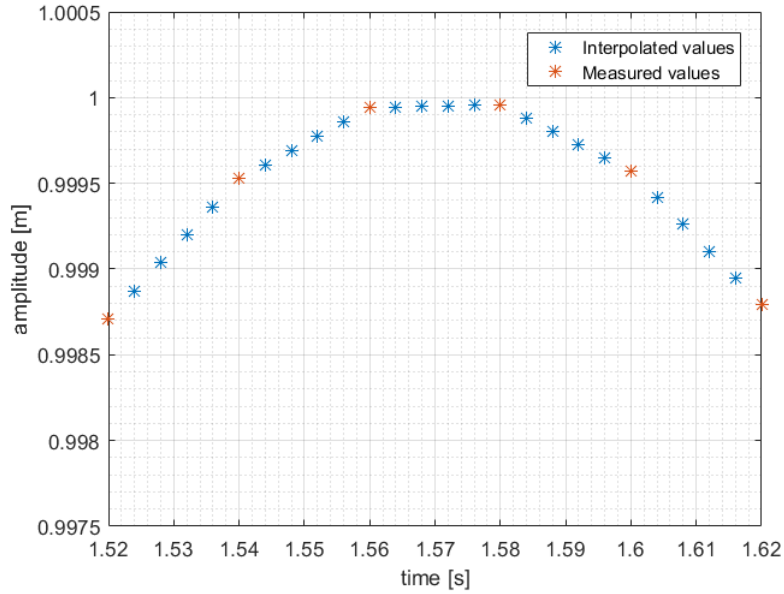
Figure 3.13: An illustrative example shows the linear interpolation of values needed for ODE45 in blue between the measured values from the model test in red. These values are only taken as an example and are not representative for the real values

Due to the the fact that the computing time of the ODE45 function increases non-linearly, the time series is split into smaller time-series so that the ODE45 ran separately on each period. The computing time for 81 periods for 1 steepness took about 8 hours, while when sliced, the computation is done in under 5 minutes. The calculation initiates at boundary conditions = 0, which is not correct, but is irrelevant if start of the calculation is far away from the evaluated range. The calculation is set to start one length of the evaluated range infront and one length behind as shown in Figure 3.14.
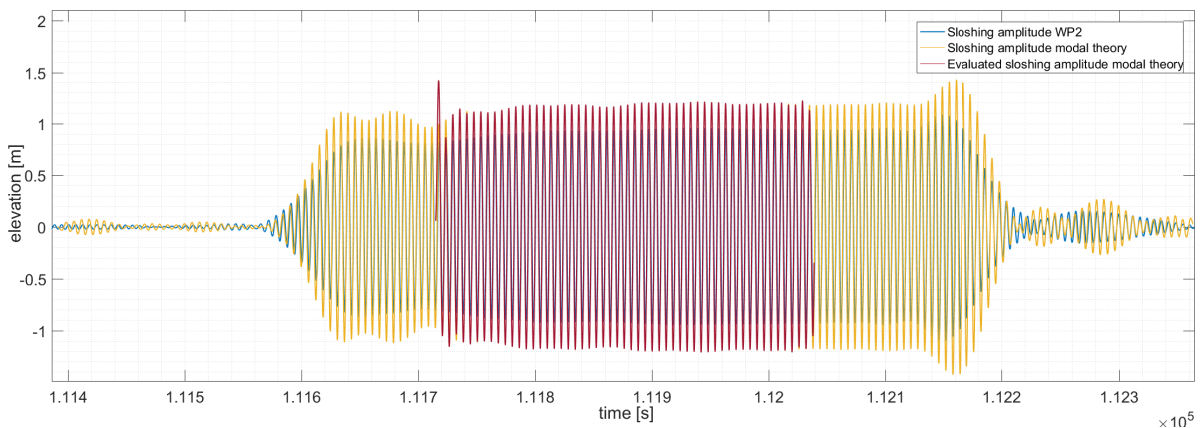
Figure 3.14: A slice of one of the evaluated time ranges. The blue color shows the measured sloshing amplitude at WP2, the yellow shows the range chosen to evaluate in ODE45 and red shows the actually evaluated range.

3.3.7 Scaling

In order to scale from model size to full scale, Froude scaling is used. Froude number is the ratio between inertia and gravity forces, and can be used for scaling using the dynamic similarity requirement between model and full scale. The equality of Froude number in model and full scale ensures that gravity forces are scaled correctly. See Appendix A for different scaling factors for parameters like time or length.

3.4 Sensitivity Analysis

An investigation of parameters is performed to inspect how the solutions of the sloshing amplitude varies along the frequency with varying input parameters in the modal function given in equation (3.8). The investigation is performed due to possibility of faulty accelerometers, calibration factors or geometrical measurements. The sensitivity study will show how small variations can influence the calculated sloshing amplitude for the first mode. The first variation consists of change in f_z, which is the distance between mean free-surface inside the model and z-accelerometer. f_z alters the corrected surge acceleration in equation (3.6). The second parameter is the surge acceleration. A multiplication factor ranging from 0.7 to 1.3 will be applied to inspect the possibility of erroneous surge acceleration sensor. The goal of the sensitivity analysis is to inspect if the variation of parameters can lead to a better compliance between the calculated and experimental sloshing amplitude.

Since the motion in surge and pitch is found using the acceleration signals, the surge and pitch acceleration signal are the two governing parameters used in the modal function solved by the ODE45 solver. The utilized multiplication factor and variation of f_z is given in Table 3.4. The parameter study is performed only for wave steepness 1 ($H/\lambda = 1/60$).

Table 3.4: The range of f_z and the multiplication factor used in the sensitivity study is given in both model and full scale values.

Quantity	Term	Range in model scale	Range in full scale scale
Distance from free-surface to z-acc. [m]	f_z	[0.123:0.06:0.160]	[10:0.5:13]
Multip. factor of surge acc. [-]	η_{1ratio}	[0.7:0.1:1.3]	[0.7:0.1:1.3]

3.4.1 Variation of f_z

The distance between the accelerometer in surge and the mean free-surface inside the model is measured to be 0.143 meters in model scale, corresponding to 11.58 meters in full scale. However, due to the measuring uncertainties, it is not known if these values were correct. Therefore, f_z is varied in order to inspect the sensitivity of the sloshing amplitude. When varying f_z, the corrected surge acceleration $\ddot{\eta}_1$ given in equation (3.6) will change. As this is one of the input parameter of the ODE45 function, the calculated sloshing amplitudes will change. f_z is varied from 9 to 12 meters with $\Delta f_z = 0.5$ m in full scale. The inspected incoming wave frequency range is shortened from the original $\omega \in [0.86 - 1.5]$ to $\omega \in [0.86 - 1.2]$ due to a large ratio spike at $\omega \approx 1.3$. The spike appears when the amplitudes approach 0 for long wave frequencies, and small changes gives very large ratios. We only inspect the first sloshing mode as well, meaning there will be no calculated response around the second sloshing mode at $\omega = 1.63$.
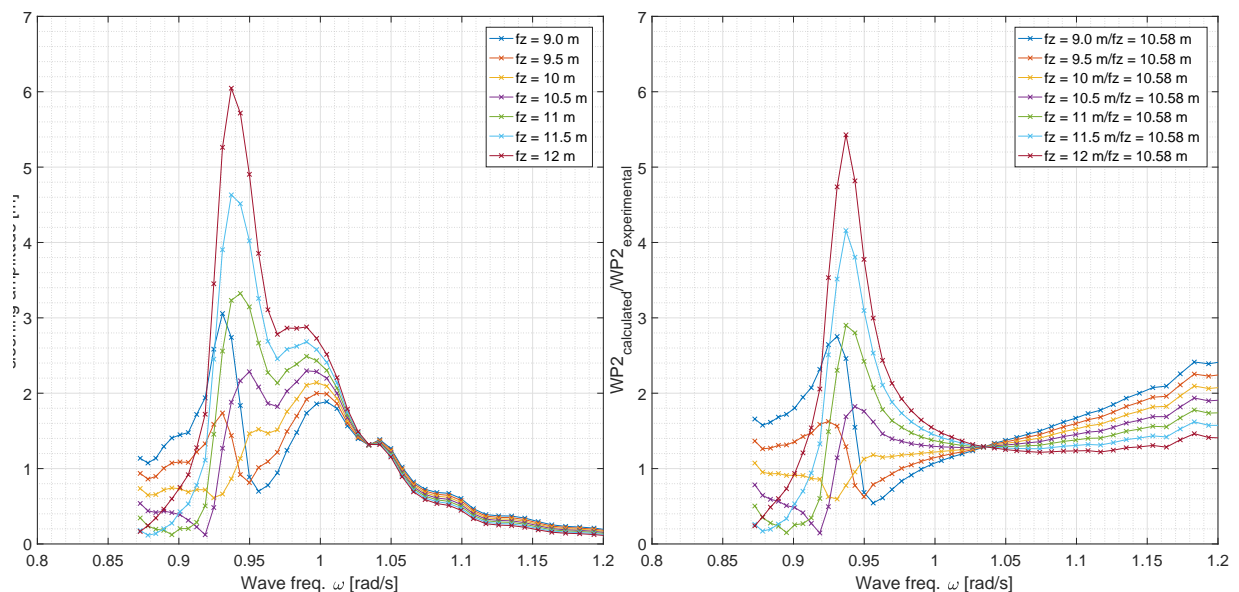
Figure 3.15: Left: Calculated sloshing amplitude with varying f_z ranging from 9 to 12 meters. Right: The ratio between the calculated sloshing amplitude and the measured sloshing amplitude. The denominator is the originally measured $f_z = 11.58$ meters in full scale. The calculation is performed for steepness 1 ($H/\lambda = 1/60$)

The calculation with varying f_z shows that small variations in f_z give large amplitude differences, especially at the natural frequency of sloshing at $\omega = 0.93$ rad/s. At this frequency, the amplitude varies from 0.6 to 5.4 meters with a corresponding ratio variation of 0.6 to 8

when varying f_z from 9 to 12 meters. In the right figure, there is point of intersection where all of the curves meet at $\omega = 1.03$. The amplitude at the intersection point is the same for all curves, meaning the corrected η_1 in equation (3.6) is constant when f_z is varied. This means that $\ddot{\eta}_5$, and consequently η_5, have to be zero at this frequency. This indicates that at the frequency $\omega = 1.03$ solely surge motion is excited.

3.4.2 Surge Multiplication Factor

The calculation of varying sloshing amplitude due to the surge multiplication factor yields similar trends as in Figure 3.15. Surge acceleration, $\ddot{\eta}_1$, is also one of the prescribed motions inserted into equation (3.3.6) used in the ODE45 function. Figure 3.16 presents the calculated sloshing amplitude when introducing a multiplication factor to $\ddot{\eta}_1$ ranging from 0.7 to 1.3.
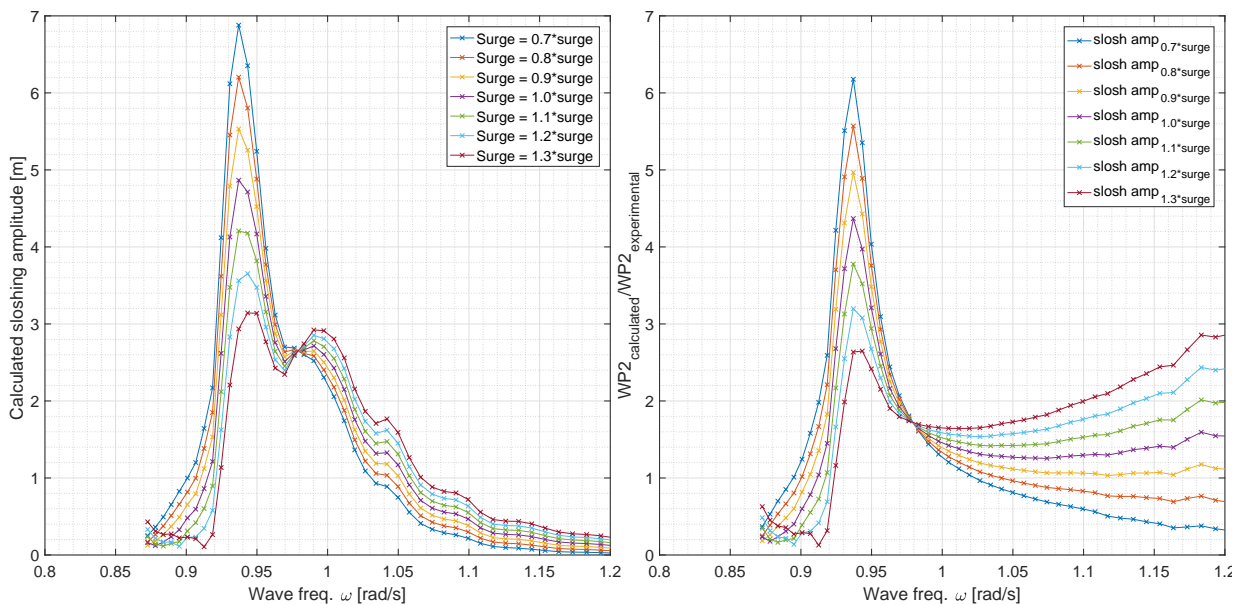
Figure 3.16: Left: Calculated sloshing amplitude with a varying surge multiplication factor ranging from 0.7 to 1.3. Right: The ratio between the calculated sloshing amplitude and the measured sloshing amplitude. Run is performed for steepness 1 ($H/\lambda = 1/60$)

As with the variation of f_z in Figure 3.15, there is a large spreading of sloshing amplitudes when varying the surge acceleration from 0.7 to 1.3. The amplitudes varies from 3.2 to 6.9 meters, with a corresponding ratio variation of 2.6 to 6.2 at the natural sloshing frequency $\omega = 0.93$. Similar to the f_z variation, an intersection point at $\omega = 0.98$ rad/s is occurring. This

intersection is at another frequency than for the f_z variation. Since there is no change in sloshing amplitude when varying the surge acceleration at this frequency, we assume that solely pitch motion is present.

3.4.3 Variation of f_z with Corrected Surge

The ratios at the two points of intersection on the right hand side of Figure 3.15 and 3.16 are 1.3 and 1.75 in size respectively. In order to get the ratios closest to 1 over the wave frequency range, we have to adjust one of the parameters to see how the other reacts. By chosing the surge multiplication factor to 0.8, the sloshing amplitude below $\omega = 0.98$ is significantly reduced. We perform a new calculation of varying f_z with the new corrected surge acceleration.
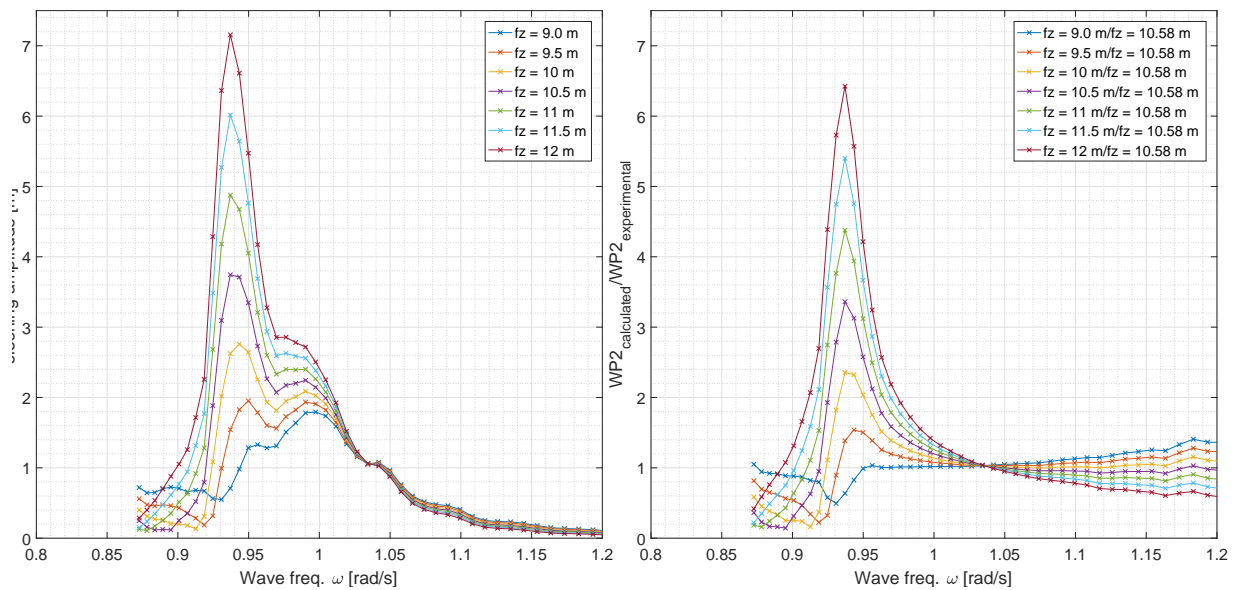
Figure 3.17: Left: Calculated sloshing amplitude with varying f_z ranging from 10 to 13 meters with surge = 0.8 of measured surge. Right: The ratio between the calculated sloshing amplitude and the measured sloshing amplitude with surge = 0.8 of measured surge. Run is performed for steepness 1 ($H/\lambda = 1/60$)

The new calculations presented in Figure 3.17 display much lower sloshing amplitudes compared to the calculations performed with original surge value, presented in Figure 3.15. The point of intersection at $\omega = 1.03$ is now close to 1, which means that at this frequency the calculated sloshing amplitude is close to the measured sloshing amplitude. Using the new

calculations, a fitting f_z can be found which gives the sloshing amplitude ratio closest to 1 over the given frequency range. The chosen f_z is set to 9.3 meters, which gives the best values given the circumstances. The resulting amplitude for $f_z = 9.3$ meters and RAO with the corrected parameters will be presented in Chapter 4 followed by a discussion around the new RAO.

Results from Experiments and Numerical Calculations

The following chapter will present observations and findings from the experimental study described in Chapter 3. The presentation is organized by giving a description of results followed by a brief discussion of the findings. The results are presented in a graphical manner in a large variety of graphs. The theoretical calculations will be compared to the experimental values where fit in order to analyze the results.

The results from experimental and theoretical calculations are presented in full scale using Froude scaling and geometrical similarities with either time extracted from the model test time series or incoming wave frequency. The incoming wave is taken as a mean of the two tank basin wave probes. The coordinate system is also body fixed, meaning all references to the coordinate system is in body fixed coordinates.

This sections starts off by presenting the re-analyzed results from the specialization project from the Fall of 2016, due to lack of a correction factor of the surge motion which was discovered in the analysis this Spring. The data has also been switched from Earth-fixed to body-fixed to be able to compare with theory. The plots will show the RAOs for the three steepnesses of $H/\lambda = 1/30$, $1/45$ and $1/60$ of surge, pitch and internal waves compared to the incoming wave amplitude. Further, the results from numerical calculation will be presented and compared to the experimental results.

A detailed study will be performed to check the sensitivity of variables in order to further investigate the deviation of experimental and theoretical calculations. Finally, a non-linearity analysis where 1st, 2nd and 3rd harmonics are extracted as well as the severity of swirling considered.

Note, all references to ω have the unit [rad/s].

4.1 Re-analysis of the Model Test Data

This section reanalyses the results from the specialization project from the Fall of 2016 due to an added correction value for surge as well changing to body-fixed coordinates. This enables comparison with theoretical calculations which are based on a body-fixed coordinate system. The following section will show the RAOs of the internal fore wave probe WP2, aft wave probe WP4, heave, surge and pitch motion followed by a short presentation and discussion of the anchoring forces.

The main natural frequency values are defined in Table 3.1 including the theoretical calculated ones and the coupled system frequency found from the experiment.

Table 4.1: All of the natural frequencies for sloshing first and second mode and coupled motion are shown.

Quantity	Term	Value
Natural sloshing frequency of 1st mode [rad/s]	σ_{1n}	0.936
Natural sloshing frequency of 2nd mode [rad/s]	σ_{2n}	1.635
Coupled system natural frequency [rad/s]	$\sigma_{1,\omega}$	1.0

4.1.1 RAO from Model Test

The RAO for the internal wave probe WP2 makes it possible to compare the internal wave amplitude to the incoming wave amplitude at each given frequency. The RAO is found for all three steepnesses $H/\lambda = 1/60, 1/45$ and $1/30$ for the full scale wave frequency $\omega \in [0.87, 1.75]$ corresponding to the full scale periods $T \in [3.6, 7.2]$ s. The steepnesses will be referred to as steepness 1, 2 and 3 respectively, for convenience. The RAO for WP2 in Figure 4.1a indicates that the largest sloshing amplitude ζ_{slosh} occurs at $\sigma_{1,\omega} = 1$ rad/s which differs from the theoretical natural sloshing frequency for the first mode at $\sigma_{1n} = 0.93$ rad/s illustrated with a black vertical line. The natural sloshing frequency is about 10 % off the coupled system frequency. The second natural frequency of sloshing is also marked with σ_{2n} due to a top occurring for the higher frequency $\omega = 1.65$ for WP2 in Figure 4.1a. The observed frequency is 1 % off the theoretical natural sloshing frequency of the second mode $\sigma_{2n} = 1.635$ rad/s. Figure 4.1a also suggests that the amplitude ratio at the peak $\omega = 1$ varies for the three steepnesses.

The RAO for steepness 1 is 3.4 at the coupled resonance top, while it is 4.1 for steepness 3.
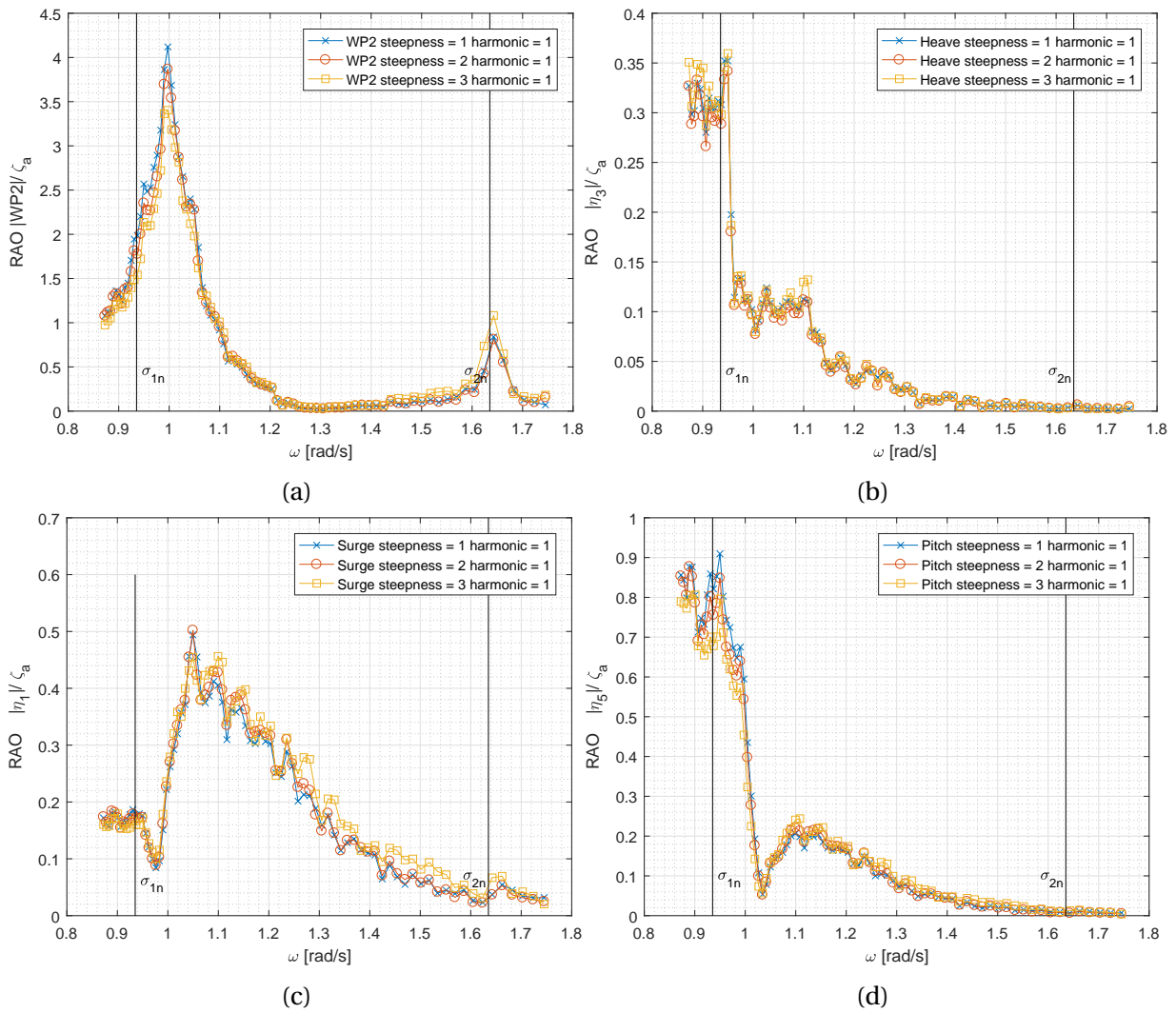
Figure 4.1: RAO of the first harmonic for WP2 (a), heave (b), surge (c) and pitch (d) in full scale for all steepnesses $H/\lambda = 1/60, 1/45$ and $1/30$. The black vertical lines represent the first and second natural sloshing frequency.

The RAO of WP2 in Figure 4.1a shows a non-insignificant dependence on the wave steepness, which indicate non-linearities caused by a dipping collar shown in Figure 3.4 in Chapter 3.2 or by the sloshing amplitudes reaching the linear approximation limit. The same dependence on wave steepness is seen at the second natural sloshing frequency. The RAOs for the three steepnesses are similar at all the other frequencies.

The collar height is 6.5 meters in full scale with the water line at half of the collar height at 3.25 meters. The largest pitch is measured towards the lower incoming wave frequencies $\omega \in [0.87, 0.95]$ for steepness 3 in full scale, corresponds to 2 meters at the wall of the model

and 2.65 meters in pitch at the edge of the collar. This leaves 0.6 meters of dry collar at the maximum pitch tilt for the steepest waves. If there is a small phase shift between the pitch motion and incoming waves so that a wave crest meets the collar at its lowest position, there is a chance of washing over the collar, introducing non-linearities. Figure 3.4 shows water washing over the edge of the collar at the highest period T = 7.2 s in full scale.

The largest peak of the sloshing amplitude is not triggered at the theoretical sloshing frequency for the first mode. Considering a rigid-body motion in two degrees of freedom, we get a coupling of motions giving two equations including coupling terms. By combining these equations, a new coupled motion system eigenfrequency emerges as explained in Chapter 2.7. This is why the coupled system sloshing frequency is not at the sloshing natural frequency. Another parameter affecting the eigenfrequencies is the liquid mass that sloshes which evaluated as a frequency dependent added mass. Therefore, there will be also a difference between considering the fluid volume as a liquid or solid mass.

The RAOs for surge and pitch shown in Figure 4.1c and 4.1d have a distinguishable drop in response at two different frequencies. The RAOs have their minima on each side of the coupled resonance top in 4.1a. The surge and pitch RAO are similar for the three steepnesses over the total frequency range. For higher frequencies $\omega > 1.6$ both RAOs go to zero.

The RAO for heave motion in Figure 4.1b shows that the heave motion has an amplitude up to 0.35 of the incoming wave amplitude with little dependence on wave steepness. In linear theory, heave motion cannot induce sloshing. However, heave can induce sloshing according to non-linear sloshing theory. The figure in Appendix E shows the total heave time series for all steepnesses and periods. The heave motion is most prominent at the higher periods when the model is exposed to the longest waves.

4.1.2 Comparison of WP2 and WP4

The measured amplitudes of first harmonic of the fore and aft wave probe WP2 and WP4 as function wave frequency are shown in Figure 4.2. The comparison is performed for wave steepness 1. Both amplitudes are similar for the whole frequency range with the same maximum at the coupled system frequency. There is a small difference in amplitudes around ω

= 1.22, but since the RAO values at this frequency are very small compared to the RAO at the system coupled frequency, we do not consider this as a significant inequality.
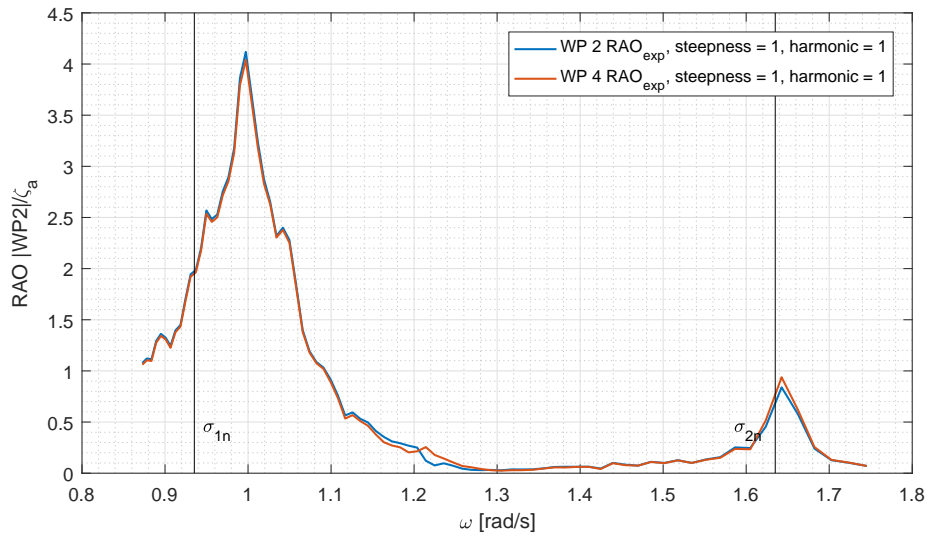
Figure 4.2: The comparison of RAOs for WP2 and WP4 in the same figure, for the first harmonic for steepness 1.

A time-series at the natural sloshing frequency (left) and coupled system natural frequency (right) of the fore and aft wave probe WP2 and WP4 are displayed in Figure 4.3. Even though non-linearities are present in the left hand side of Figure 4.3b, the phase shift between the wave probes is 180 degrees. The same phase shift is also seen in the right hand side of Figure 4.3b.
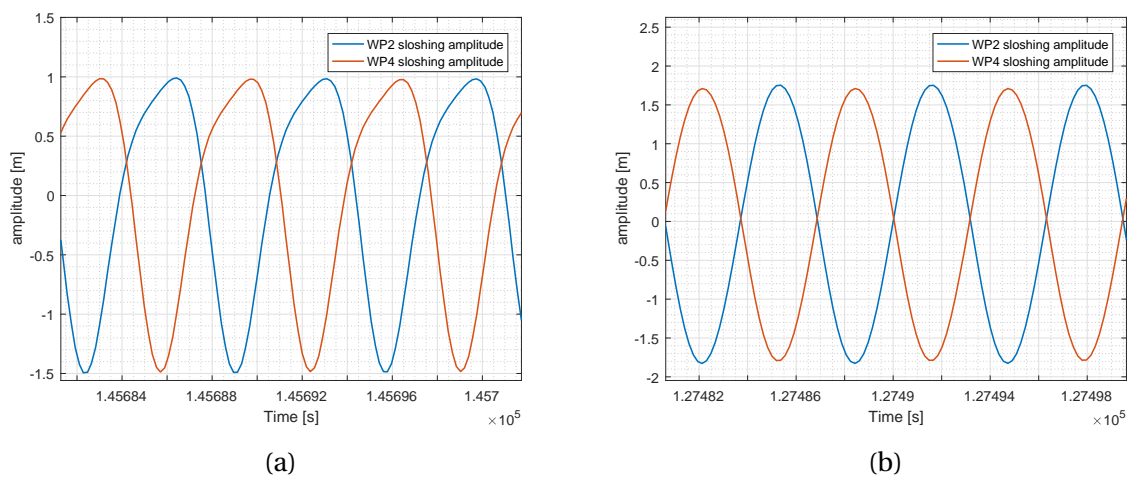
Figure 4.3: A time-series for the sloshing amplitudes around the natural sloshing frequency $\omega = 0.93$ (a) and the coupled natural sloshing frequency (b) $\omega = 1.0$

The non-linearities are noticeable due to the altered shape of the curve compared to the curve in Figure 4.3b. The sloshing amplitudes as a function of time in Figure 4.3a do not oscillate about the 0 mean and the amplitudes and form of wave crest and wave through are not equal. Non-linearities will be discussed further in Section 4.5.

4.1.3 Force Measurements

The force is measured using two strain gauges attached between the fore anchoring lines and the model. The strain gauges measure a pretension of 10 N in model scale corresponding to 513 kN in full scale. Figure 4.4 presents the total force amplitudes in x-direction excluding the pretension force. The Figure also presents the sloshing amplitudes for direct comparison.
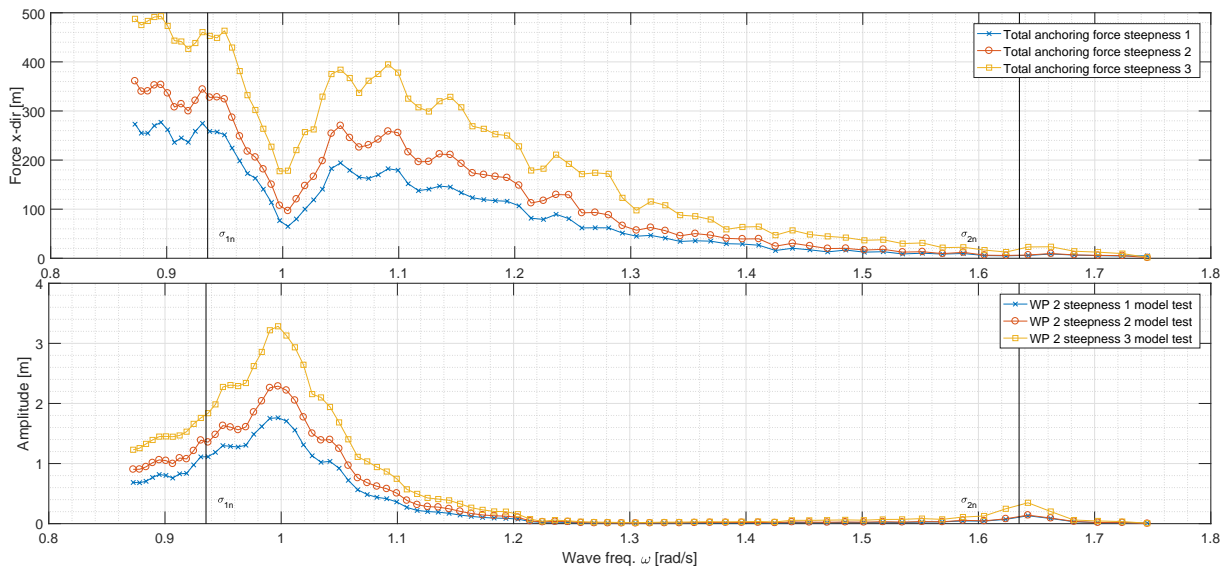
Figure 4.4: Total anchoring force in x-direction for each period and steepness $H/\lambda = 1/60, 1/45$ and $1/30$. The corresponding sloshing amplitude at WP2 is shown in the lower figure. All data is in full scale

The plot shows a cancellation of force at the coupled system eigenfrequency where the sloshing amplitude is the largest. The interesting fact is that the cancellation of force amplitude is different than the cancellation frequency of surge and pitch shown in Figure 4.1c and 4.1d, and does not show any reactions to these frequencies. A simple estimate of the decrease in force magnitude due to the cancellation is shown in Figure 4.5 where linear interpolation between the frequencies $\omega = 0.95$ and 1.05 at each side of coupled system frequency for steepness 3 is used.
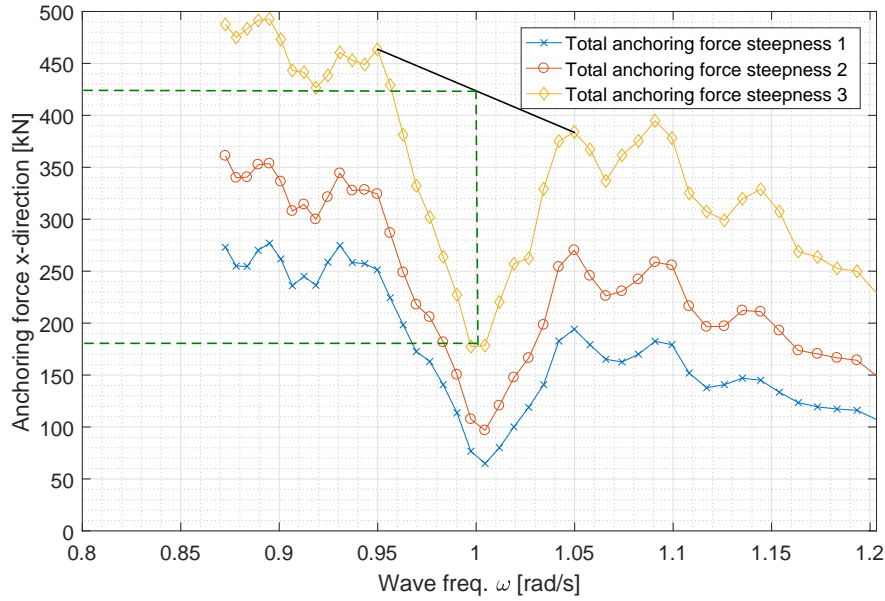
Figure 4.5: Total anchoring force in x-direction for each period and steepness $H/\lambda = 1/60, 1/45$ and $1/30$ for frequency $\omega \in [0.87, 1.2]$. The linear interpolation is marked with a black line and the extracted values are marked with striped green lines.

The cancellation at the coupled system frequency for steepness 3 decreases the force from 425 kN to 180 kN, corresponding to a 58 % difference. The same procedure is applied for for the two other steepnesses, and the results are summarized in Table 4.2 below.

Table 4.2: Anchoring forces for steepness 1, 2 and 3 are presented at the coupled system frequency $\omega = 1$ and the forces for the interpolated values extracted as shown in Figure 4.5. The percentage due to the cancellation effect is also presented.

Steepness	Force at sys. freq. [kN]	Int. Pot. Force [kN]	Difference in %
$H/\lambda = 1/30$	60	200	70
$H/\lambda = 1/45$	100	230	57
$H/\lambda = 1/60$	180	425	58

The cancellation leads to a significant decrease of up to 70 % at the coupled system frequency. Although further investigation into anchoring dynamics and detailed calculations of the experiment are interesting, this will not be pursued further due to the objectives of this thesis.

4.2 Results from Numerical Calculations

The following section presents the amplitudes of the time-series for each of the periods as well as the ratio between calculated sloshing amplitude and the measured model test amplitude. The presented results are taken from the body motion with no added correction factor, which will be investigated in the sensitivity analysis in Section 4.4.

The results from the numerical calculations are performed using the ODE45 scheme as described in Chapter 3.3.6. The total time series of each measurement is split into smaller time-series for each wave period in the model test to save time on computation. The modal function solved by the ODE45-function uses the input values of η_1, $\ddot{\eta}_1$ and $\ddot{\eta}_5$. In order to stabilize the beating of the undamped system, a damping factor of 0.01 was added in order to remove the transient. The time-series of the sloshing amplitudes from the model test with 3 wave steepnesses each with 81 periods is presented in Figure 4.6. The blue color represents the theoretical calculations, while the red color represents the actual measured sloshing amplitude at WP2.
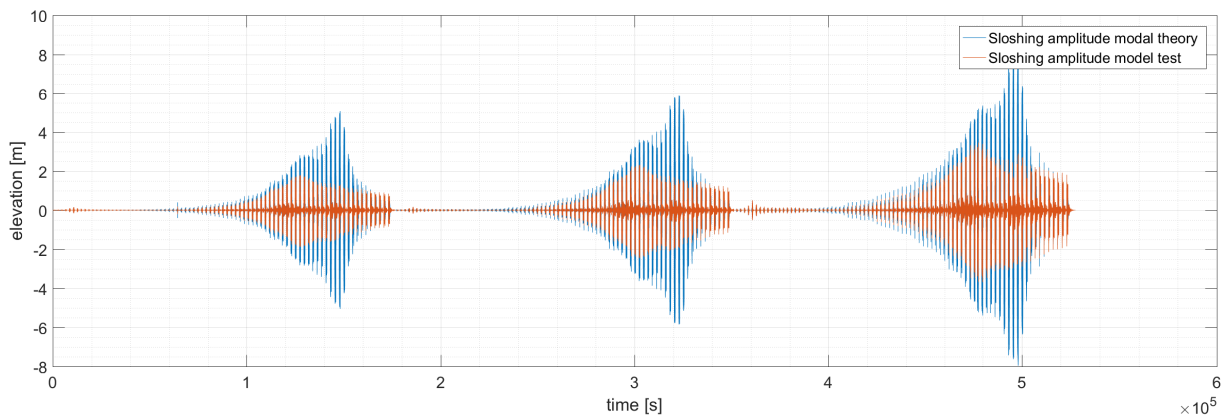
Figure 4.6: Time series plot of the all steepness $H/\lambda = 1/60, 1/45$ and $1/30$ for all of the periods T = [3.6, 7.2] s. The blue color shows the modal theory calculations for each period and the red shows the measured sloshing amplitude at WP2. All results are given in full scale.

There is clearly a higher amplitude of the calculated sloshing period throughout all of the periods, but especially towards the ends of each steepness. The large tops occur close to the theoretical natural sloshing frequency which will be discussed further when presenting Figure 4.9. The concentration of red color around the mean 0 is only due to the model coming to rest between each run and the scaling of the Figure.

The calculated RAO in Figure 4.7 shows a large top at $\omega = 0.94$ which is close to the theoretical natural frequency of sloshing of the first mode $\sigma_{1n} = 0.93$. At $\omega = 1$, a smaller top appears which complies with the system natural frequency peaking at $\sigma_{1,\omega} = 1$ rad/s as presented in Figure 4.1a. The highest amplitudes of sloshing for the three wave steepnesses at $\omega = 0.94$ vary in ratio showing a dependence on the wave steepness. The first steepness $H/\lambda = 1/60$ reaching a ratio of 9 followed by 7.8 for the second steepness $H/\lambda = 1/45$ and 6.8 for the third steepness $H/\lambda = 1/30$. The second top at the system natural frequency $\omega = 1$ has ratios ranging from 6 to 5.4 for each steepness respectively.
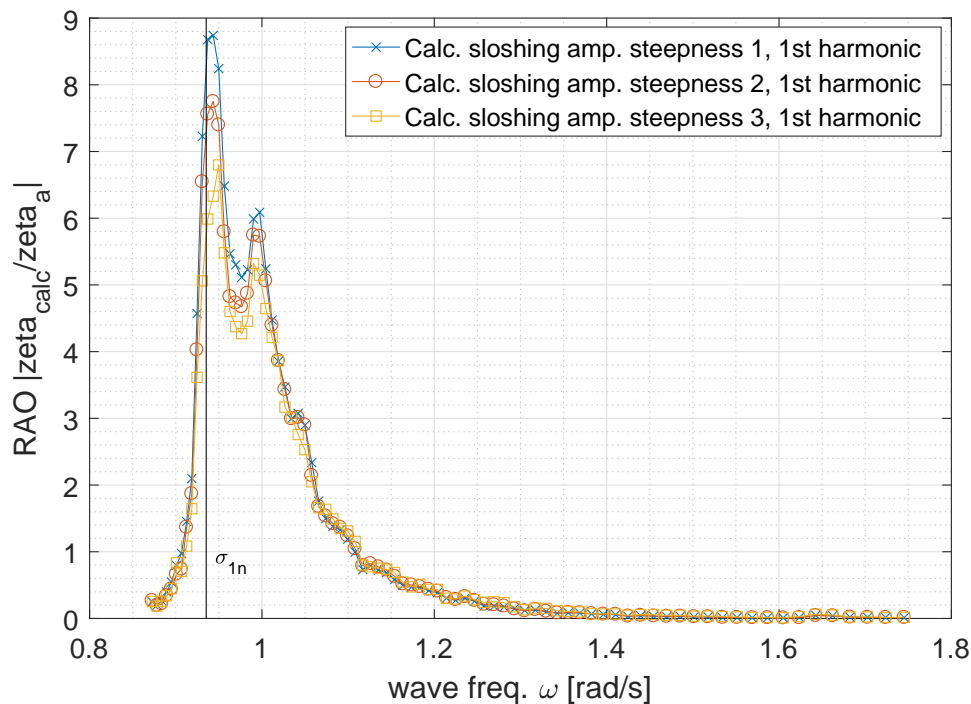
Figure 4.7: RAO of the theoretical first harmonic for sloshing amplitude in full scale for all steepnesses $H/\lambda = 1/60, 1/45$ and $1/30$. The black vertical lines represent the first sloshing frequency.

The calculations only include the first natural sloshing mode, not giving any response at the second natural sloshing frequency $\sigma_{2n} = 1.63$ rad/s. The RAO at the system eigenfrequency for the three steepnesses are close to each other, which was expected due to linear theory. However, the large amplitudes at the sloshing natural frequencies dominate which is not correct with the observed results from the model test.

4.3   Comparison Between Experiment and Theory

As presented in section 4.2, the experimental results do not coincide with the theoretical calculations as wanted. In particular, there is a distinct difference around the sloshing natural frequency. The coupling of motions and additional added mass terms from the moving liquid with a free surface combine into one fourth order polynomial. The solution to this polynomial is the natural frequency of the system, which will differ to the natural frequencies of each individual natural frequency for the sloshing, surge and pitch.

To visually inspect the time series at the coupled system frequency and natural sloshing frequency, a time-series of the calculated sloshing amplitude and experimental sloshing amplitude is compared in Figure 4.8a, 4.8b and 4.8c. The time-series are presented for the frequencies $\omega = 0.93$, $\omega = 1$ and $\omega = 0.872$ respectively. All three plots are for the steepness 1 ($H/\lambda = 1/60$).
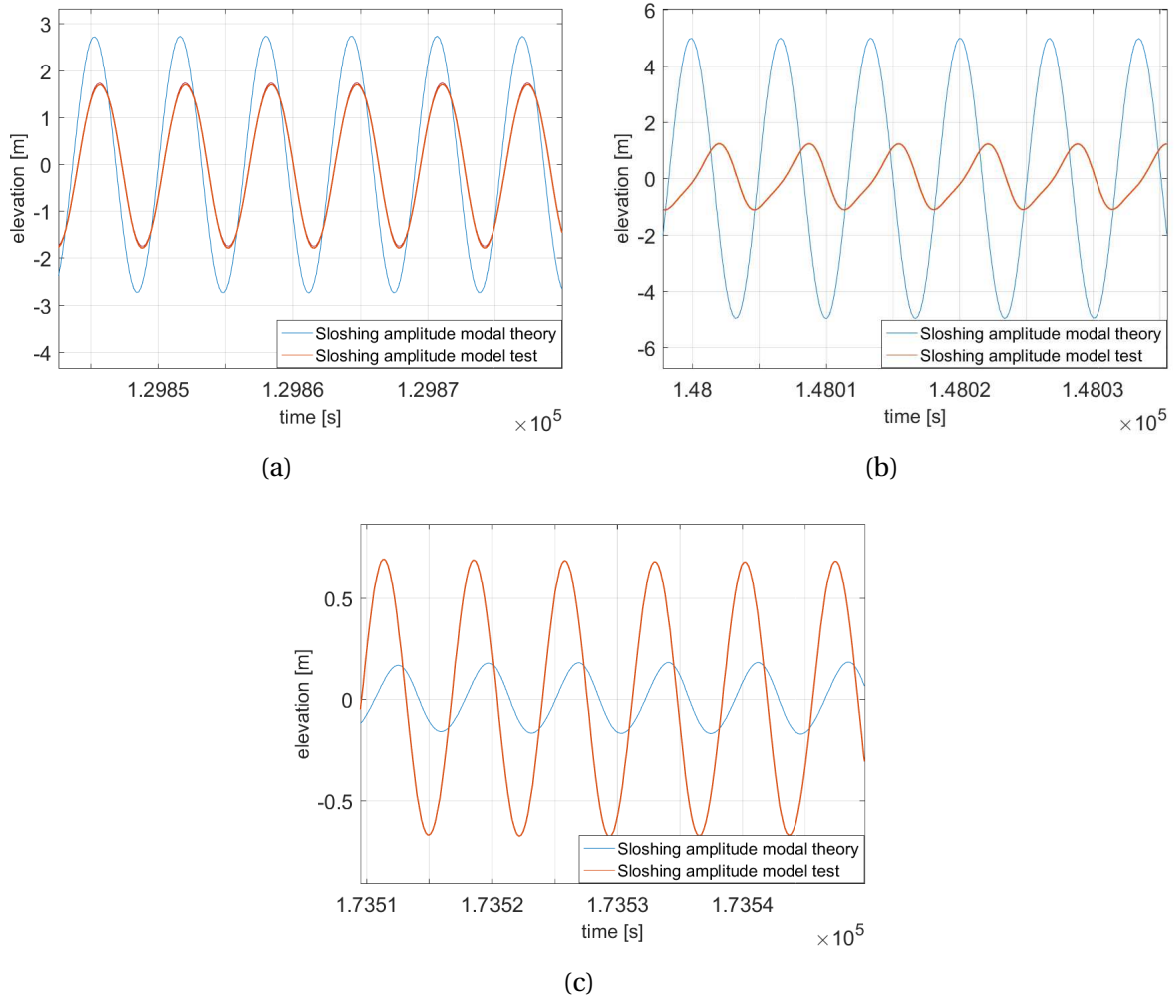
Figure 4.8: Time series of three different wave periods (a) system natural frequency, (b) sloshing natural frequency, (c) shortest frequency $\omega = 0.872$ rad/s. All figures include both the theoretical sloshing amplitude and the calculated sloshing amplitude. All plot are run at steepness 1.

Figure 4.8b shows clear nonlinearities for the model test sloshing amplitude, whereas the calculated amplitudes are higher in comparison. This indicates that there is transfer of energy to higher modes taking place in the model test. The Figure shows the time-series for the lowest steepness $H/\lambda = 1/60$, which points towards even higher nonlinearities at the larger steepnesses. The non-linearities will be further discussed in Section 4.5.

We compare the amplitudes of theoretical and experimental sloshing amplitude in Figure 4.6. The Figure shows some differences like a distinct top for the calculated sloshing amplitude for each steepness which is occuring near the sloshing eigenfrequency $\omega = 0.93$. Further, we compare the sloshing amplitudes to the calculated sloshing amplitudes presented

in Figure 4.9 for all three steepnesses.
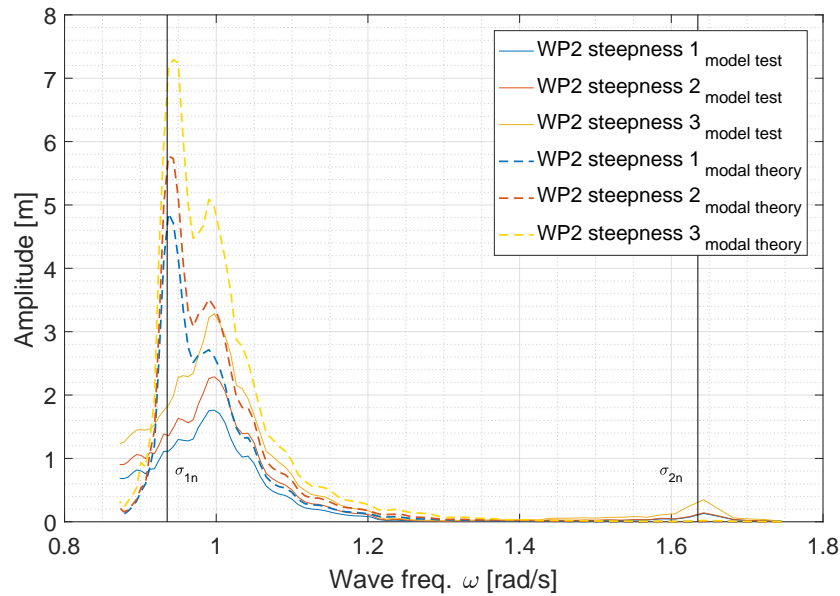
Figure 4.9: Amplitude comparison for calculated sloshing amplitude and experimental sloshing amplitude for all three steepnesses. The black vertical lines represent the first and second natural sloshing frequency.

The comparison indicates that linear modal theory has difficulties in calculating the sloshing amplitude around the eigenfrequency. The linear modal theory is applicable for non-resonant sloshing and gives in theory an unlimited sloshing amplitude at the resonance top. However, the prescribed motions in surge and pitch used to calculate the sloshing amplitude are taken directly from the experiment. Since the modal function we use to calculate the sloshing amplitude uses prescribed accelerations and motions taken directly from the model test, it was not expected to see the sloshing react as greatly at the natural sloshing frequencies.

4.3.1 Phase Angles

Apart from the clear discrepancies in the amplitudes, phase differences are also observed. Ideally, the phase difference should be equal 0 in order to have no phase difference between the calculated and experimental sloshing amplitudes. Figure 4.10 shows the phase difference for the whole range of ω.
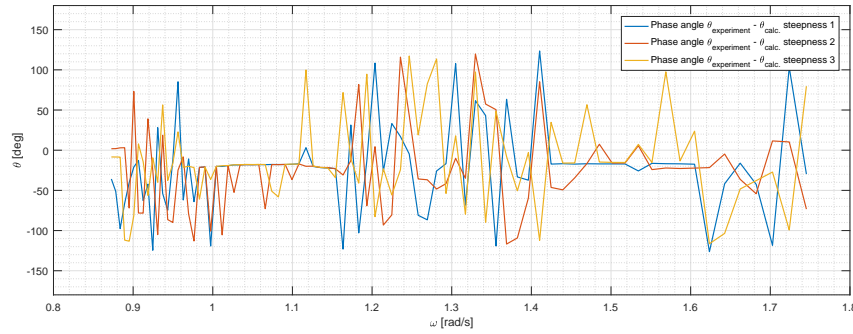
Figure 4.10: Phase angles between the experimental and calculated sloshing amplitudes for steepness 1, 2 and 3. Some erroneous phase angles are presented due to the large jumps, but the main trend at -20 degrees is seen.

At no point does the phase difference cross 0, with a minimum of -20 degrees $\omega = 1.03$. There is also a 180 degree shift at around the natural sloshing frequency.

4.4 Re-analysis of Sloshing

The following section presents a re-analysis of the sloshing amplitude time-series and time-series with the newly adjusted distance between the free-surface and accelerometers and new surge multiplication factor as presented in Chapter 3.4.1. The sensitivity analysis inspects the variation in sloshing amplitude when altering the input parameters of the modal function solved using the ODE45-function. The two governing factors that have been chosen are inserted into the modal function and run to investigate the possibility of faulty accelerometers, calibration factors or geometrical measurements. The re-analysis is only run for wave steepness 1 with a shortened frequency range of $\omega \in [0.87, 1.2]$.

4.4.1 Sloshing Amplitudes with Adjusted Parameters

The adjusted parameters applied in order to find the new calculated sloshing amplitudes are presented in Table 4.3. Both the original parameter and the adjusted parameters for f_z and surge multiplication factor are presented in model scale and full scale.

Table 4.3: Original and adjusted parameters used for the sensitivity analysis. The adjusted distance from the free surface to the z-accelerometer f_z is given for the original and adjusted in model scale and full scale. The original surge factor and adjusted surge multiplication factor is also given as $\eta_{1,times}$.

Quantity	Term	Model scale original	Model scale adjusted	Full scale original	Full scale adjusted
Distance [m]	f_z	0.143	0.117	11.58	9.5
Multiplication factor	$\eta_{1,times}$	1	0.8	Same as model scale	

By inserting the adjusted values into the modal function, new calculated sloshing amplitudes are found. The top which was prominent for the original values at the sloshing natural frequency around $\omega = 0.93$ is now reduced to 1.7 meters in full scale, corresponding to a ratio between the calculated and experimental sloshing amplitude of just 1.3.
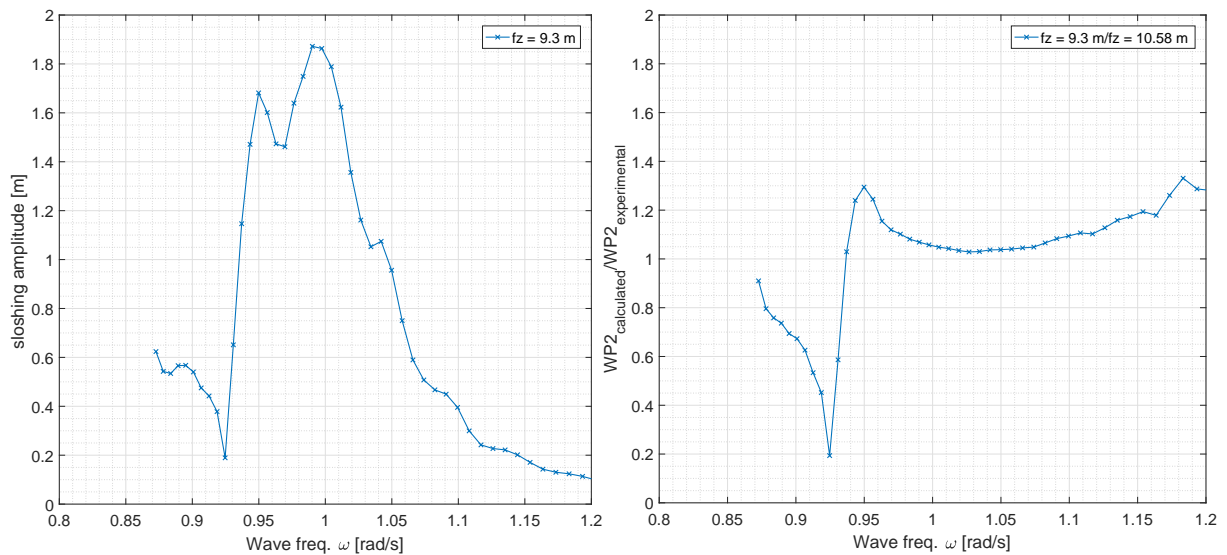
Figure 4.11: Left: Calculated sloshing amplitude with $f_z = 9.3$ meters with surge = 0.8 of measured surge. Right: The ratio between the calculated sloshing amplitude and the measured sloshing amplitude with adjusted parameters. The results are shown for steepness 1 with $H/\lambda = 1/60$

The calculated sloshing amplitudes using the adjusted values indicate much smaller differences between the calculated and experimental sloshing amplitudes. As the amplitude at the sloshing frequency has been significantly lowered, a new minimum at $\omega = 0.925$ has appeared. The ratio plot in the right hand side of Figure 4.11 also show a large difference between $\omega = 0.87$ to right after the natural sloshing frequency at about $\omega = 0.95$. The ratio is close to 1 from $\omega = 0.95$ to the limit at $\omega = 1.2$.

The RAO of the calculated sloshing amplitude with the corrected values is presented in Fig-

ure 4.12. The RAO at the natural sloshing frequency $\omega = 0.93$ is reduced from 6.8 down 2. The RAO looks more correct compared to RAO based on the experimentals results only. The RAOs from $\omega = 0.94$ and outwards are much closer, but still experiences non-similarities from $\omega = 0.87$ to about 0.97.
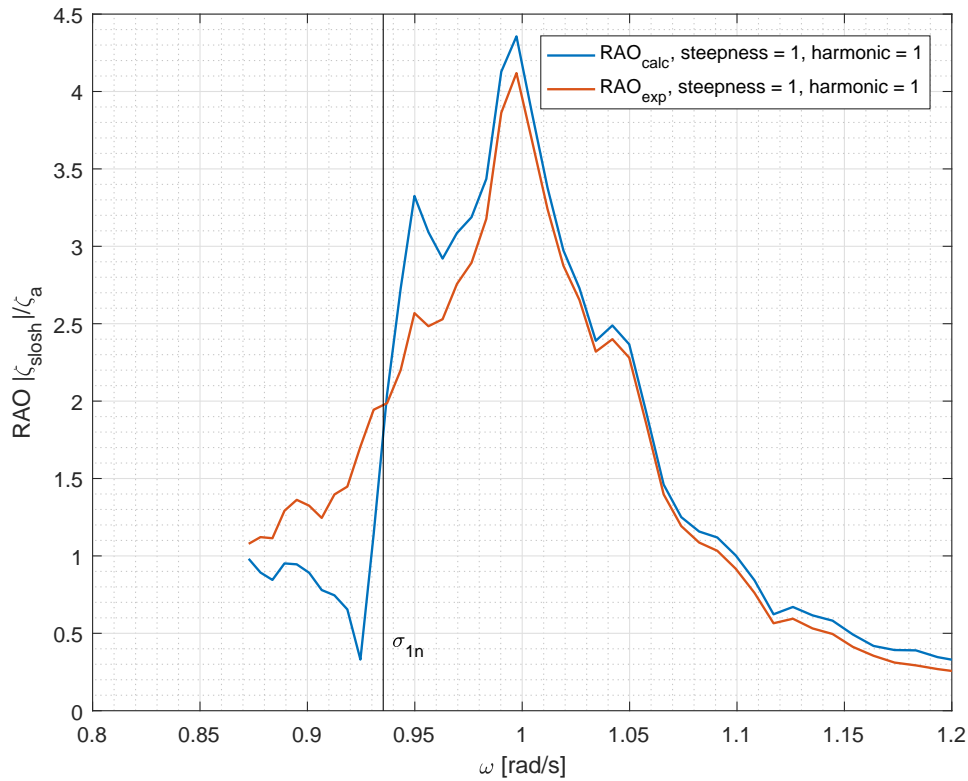
Figure 4.12: RAO of the theoretical first harmonic for sloshing amplitude in full scale for 1st steepnesses with corrected f_z and surge ratio compared to the experimentally found sloshing RAO. The black vertical lines represent the first natural sloshing frequency.

The calculated RAO follows the trends of experimental RAO much closer with the adjusted parameters. However, around the natural sloshing frequency, there are still some differences. As inspected, the sloshing amplitudes around the natural sloshing frequency are very sensitive to the input parameters of the modal function, and small changes can lead to large differences.

To inspect the sloshing amplitudes with the adjusted parameters, the time-series of the newly calculated sloshing amplitude and experimental sloshing amplitude between $\omega \in [0.8, 1.2]$ are presented in Figure 4.13.
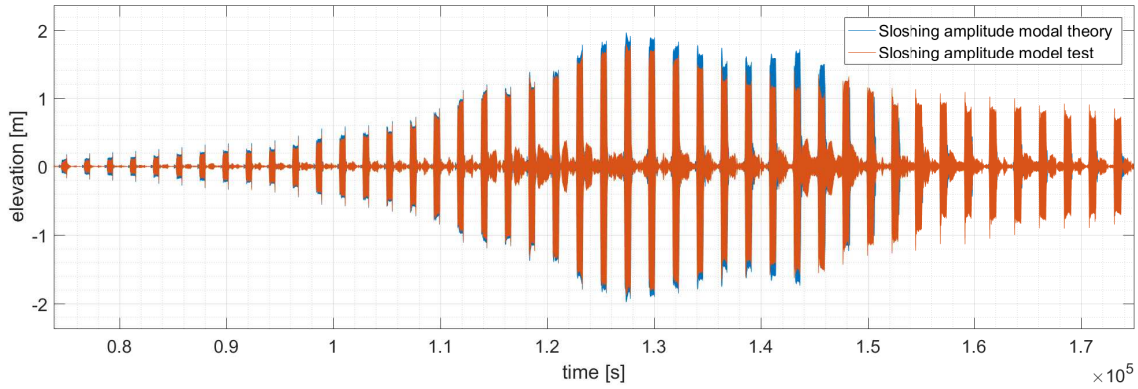
Figure 4.13: Time series for the wave periods corresponding to the RAO given in Figure 4.12. The red plot shows the sloshing amplitude from the model test and the blue shows the calculated sloshing amplitude with the adjusted values. The time-series is presented for steepness 1 only.

As the RAO pointed out, the sloshing is much closer in amplitudes, with still slightly higher amplitudes around the sloshing natural frequency. The natural sloshing frequency is occurring where difference between the blue and red color are the largest at around 1.45×10^5 seconds on the x-axis. Since the amplitudes are closer to each other with the adjusted values, the phase angles between the calculated sloshing amplitude and measured sloshing amplitude are inspected. These are presented in Figure 4.14.
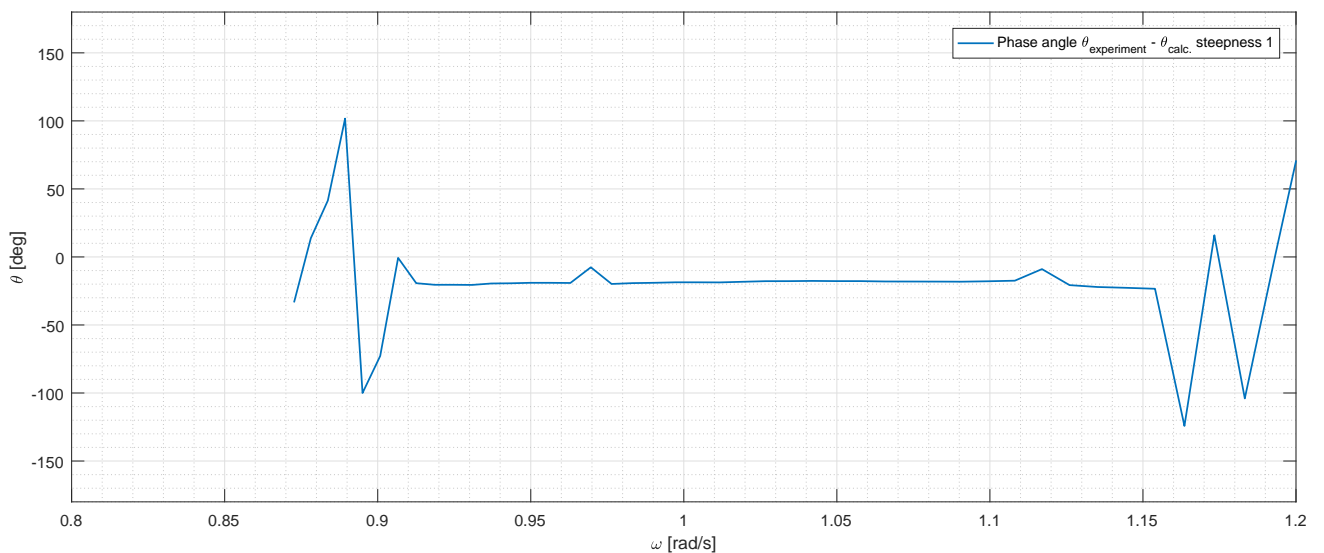
Figure 4.14: Phase angles between the experimental and calculated sloshing amplitudes with adjusted f_z and surge multiplication factor for steepness 1. The phase angles remain at -20 degrees at best, with a discontinuity at the sloshing natural frequency.

The phase angle are slightly improved over the original phase angles shown in Figure 4.10, but phase difference between the experimental and calculated sloshing amplitude is -20 degrees at best. Around the natural sloshing frequency, a discontinuity is noticeable.

4.5 Non-linear Analysis

At the sloshing frequency we observe non-linearities. These may be one the reason for why the linear sloshing theory predicts too high amplitudes. The non-linearities dampen the sloshing amplitude by transfering energy to higher modes, which is indicated in figure 4.15a, 4.15b and 4.15c. The plots show time-window of total time series around the natural sloshing frequencies for the three steepnesses.

(a)

(b)

(c)
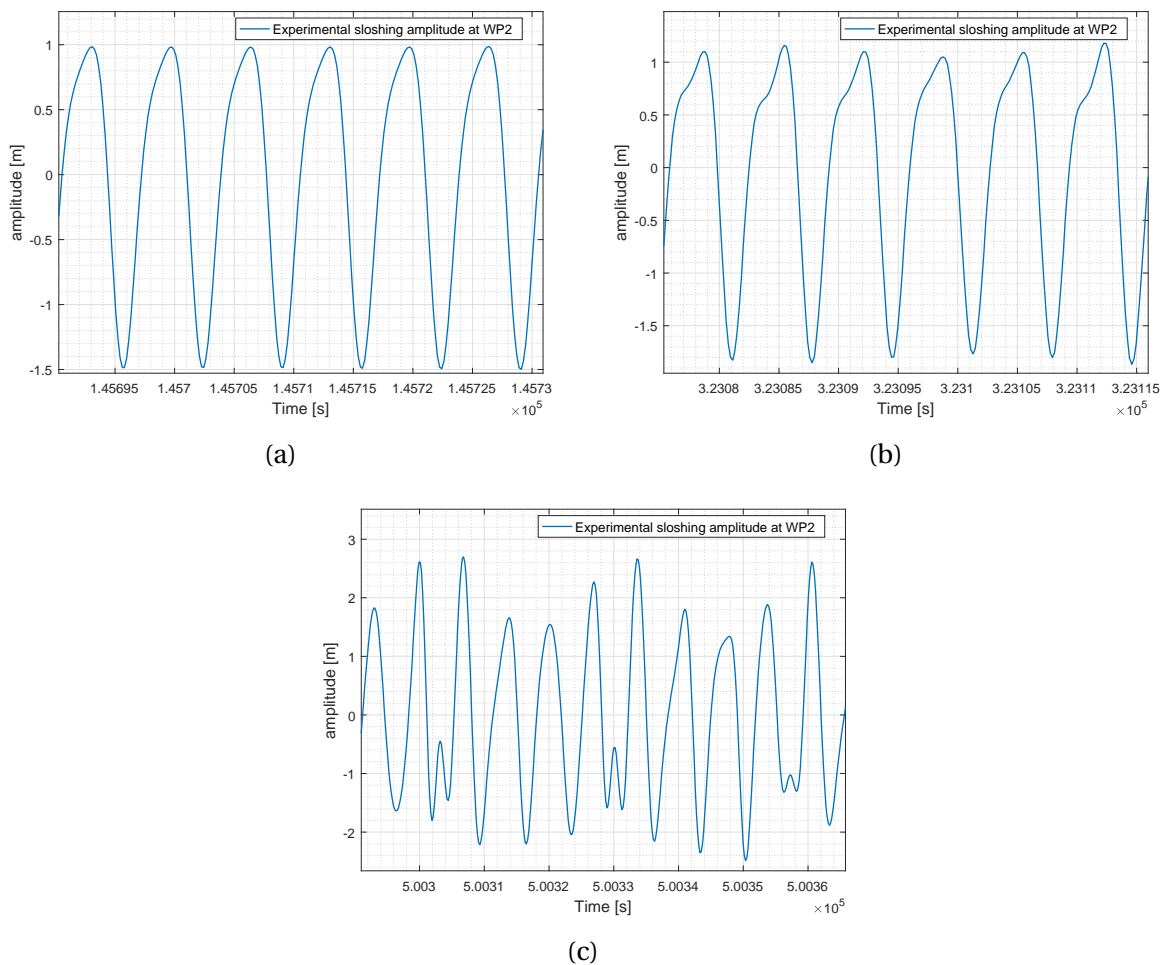
Figure 4.15: Time series plot around the natural sloshing frequency $\omega_n = 0.93$ rad/s for all three steepnesses $H/\lambda = 1/60$ (a), $1/45$ (b) and $1/30$ (c). Plot (c) for last steepness is slightly longer due to more inconsistent wave patterns.

The non-linearities are distinguishable due to their shape at the wave crest and wave through. For a normal harmonically oscillating linear wave, as the incoming wave is, the wave is symmetric about the x-axis. The non-linearities intensify for the increasing steepness due to the sharper wave through and skewed wave crest comparing (a) with (b). In (c), the higher order terms are even more prominent. All of the maximum of the time-series are inconsistent and differ from each other.

By filtering the data for different harmonics, we can extract the 1st, 2nd and 3rd harmonics of the model test data to inspect the non-linearities of the runs. The RAO for steepness 1, 2 and 3 are plotted independently with the three harmonics divided by the amplitude of the first harmonic of the incoming wave in order to compare magnitudes.
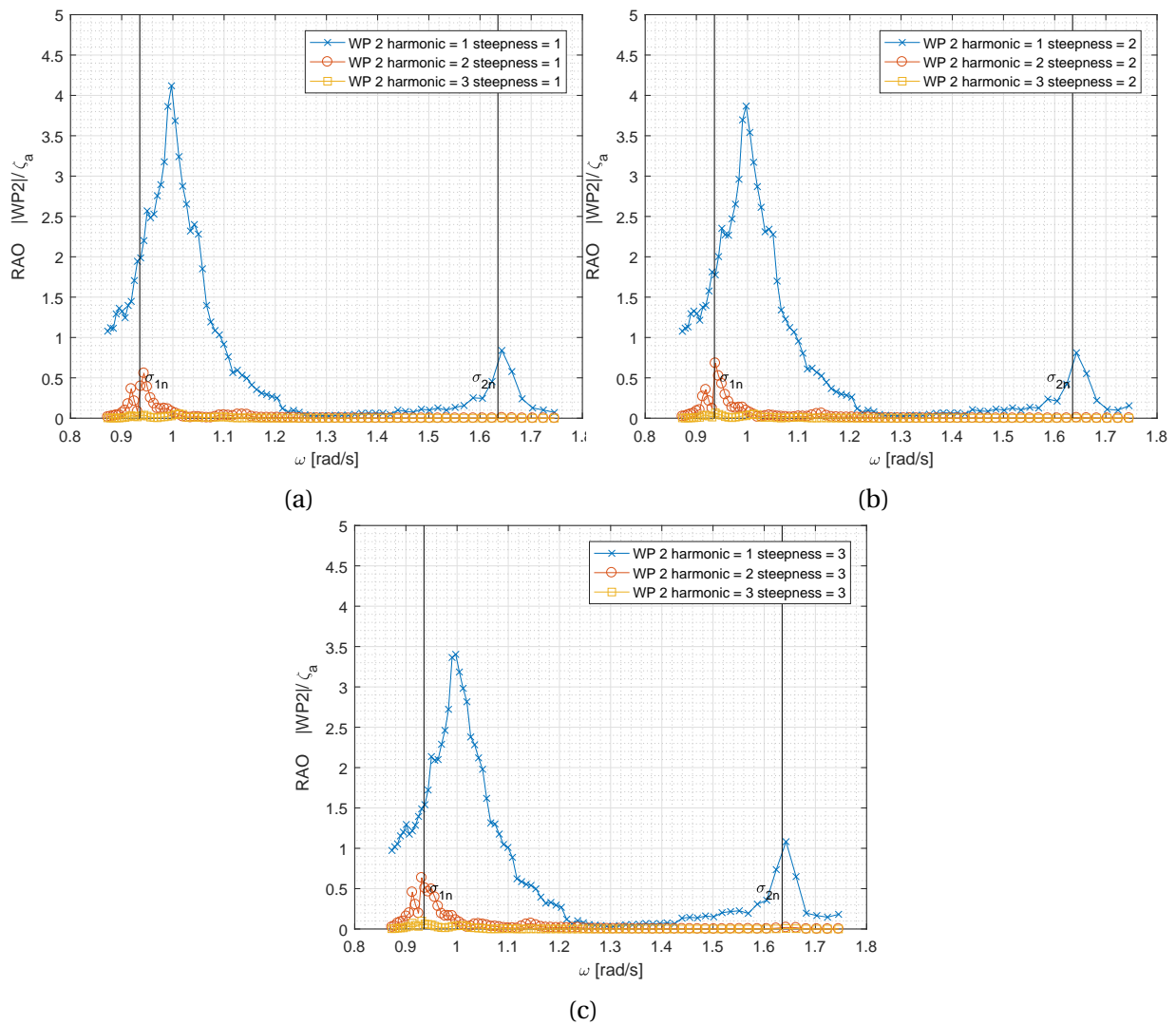
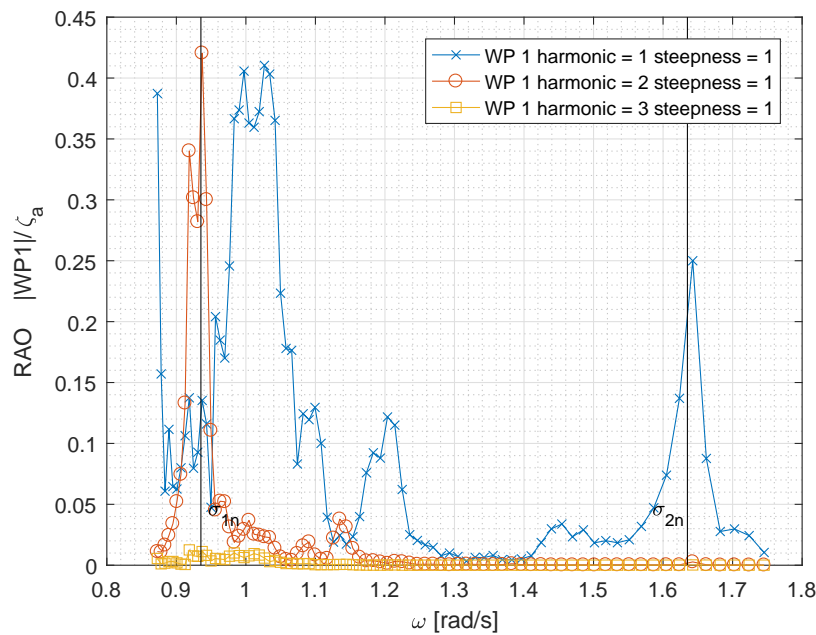Figure 4.16: RAO for internal wave probe WP2 in full scale for 1st, 2nd and 3rd harmonics for (a) steepness 1: $H/\lambda = 1/60$, (b) steepness 2: $H/\lambda = 1/45$ and (c) steepness 3: $H/\lambda = 1/30$. The black vertical lines represent the first and second modal natural sloshing frequency.

The RAOs show a varying ratio between 4.2 and 3.5 for all of the steepness, with the same trends seen in all three plots. The yellow line representing the 3rd harmonic is approximately 0 for the whole frequency range. The red line shows a 2nd harmonic response at the sloshing eigenfrequency with a value of 0.5 for steepness 1 to 0.7 for steepness 3. The amplitude of the 2nd harmonic for steepness 3 is almost as large as the incoming wave amplitude, which indicates that some significant non-linearities are taking place at the sloshing eigenfrequency where linear modal theory over-predicts the sloshing amplitude. Therefore, there are reasons to believe that the non-linearities are of such significance that the linear modal theory cannot predict the correct amplitudes around the natural sloshing frequencies.

The same plots in Figure 4.17 are plotted anew in one plot to directly compare the RAO of the first and second harmonic.
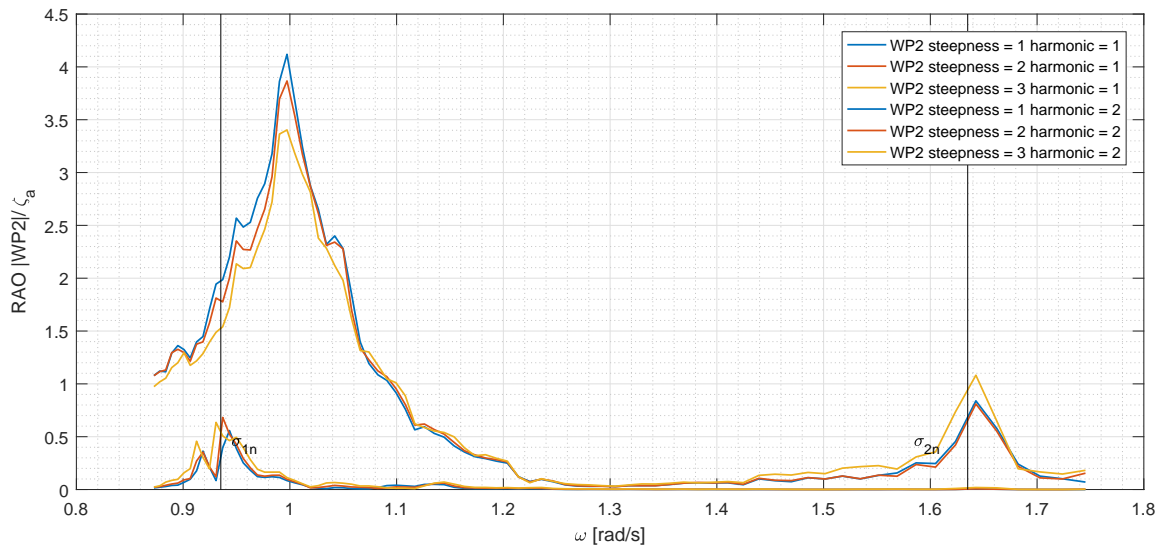
Figure 4.17: RAO for internal wave probe WP2 in full scale for 1st, 2nd for steepness 1 ($H/\lambda = 1/60$), steepness 2 ($H/\lambda = 1/45$) and steepness 3 ($H/\lambda = 1/30$) all in the same plot. The steepness for the 1 st and 2nd harmonic have matching colors. The black vertical lines represent the first and second modal natural sloshing frequency.

4.5.1 Swirling

Swirling is a wave motion in the angular direction in a circular tank (Faltinsen and Timokha, 2009). Ideally our model only moves in two motions namely surge and pitch, but due to no solid constraints in the other four degrees of freedom, 3D motions are present. This means that small movements off center of the longitudinal x-axis, or roll motion about the x-axis can

cause the water inside the structure to swirl which is a non-linear phenomenon. Therefore, a time-series range is inspected containing all 4 of the wave probes inside the model. If there is a phase difference between the side probes and fore and aft, swirling may be occurring. Figure 4.18a, b and c presents time-series for selected wave frequencies $\omega = 0.93$ around the natural sloshing frequency, the coupled system frequency $\omega = 1$ and shortest frequency $\omega = 0.87$. The fore and aft wave probes indicated by red and purple lines in the upper left figure are 180 degrees out of phase, which is as expected for the first linear sloshing mode. The blue and yellow lines show the amplitudes of the side probes which are also 180 degrees out of phase from each other, and slightly shifted with the fore and aft wave probes. Figure 4.18b shows both indications of non-linearities at fore and aft wave probes, but now the side probes oscillate with twice the frequency, with approximately 0 phase between them.

(a) $\omega = 1$
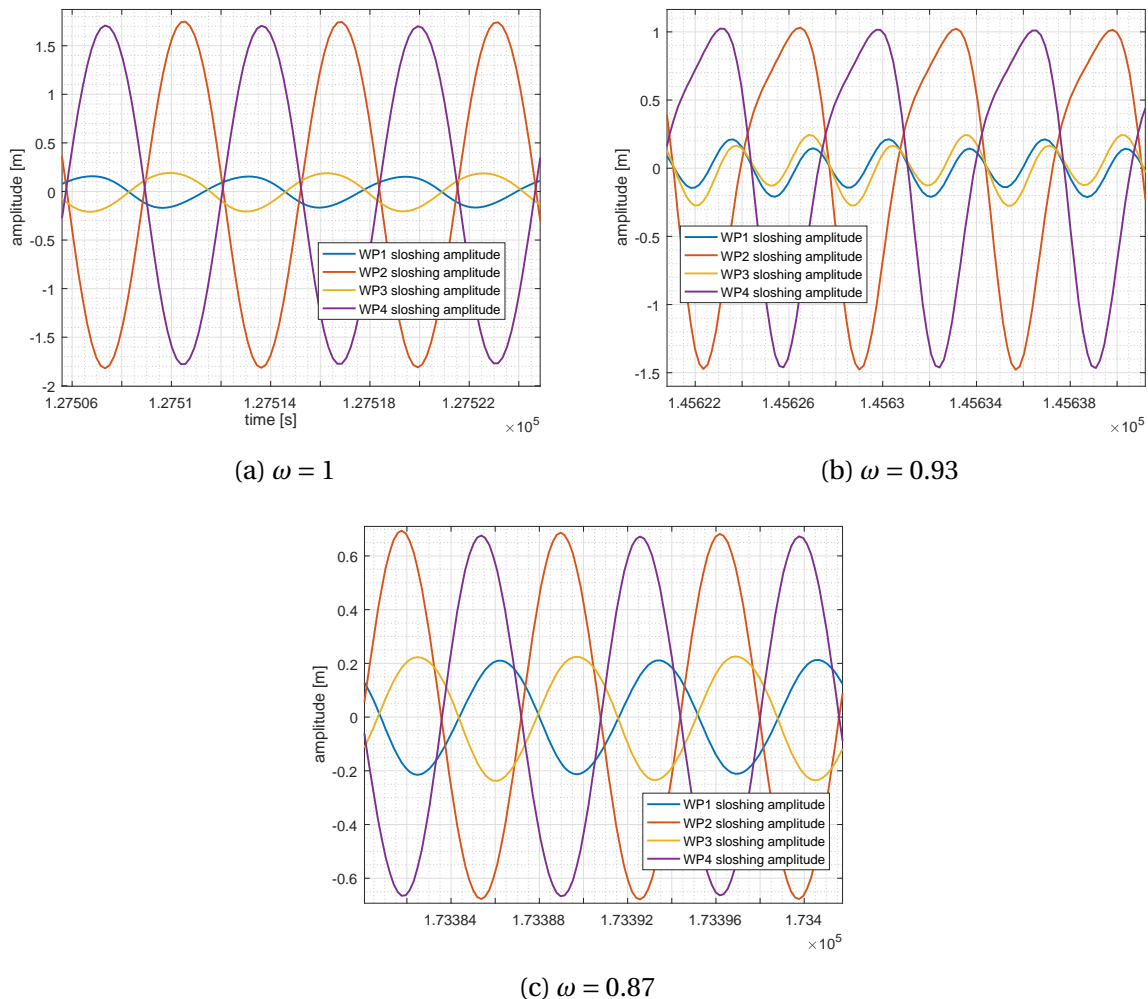
(b) $\omega = 0.93$

(c) $\omega = 0.87$

Figure 4.18: Figure showing a time-series for the three selected wave frequencies (a) $\omega = 1$, (b) $\omega = 0.93$ and (c) $\omega = 0.87$ for the first wave steepness ($H/\lambda = 1/60$) including all of the wave probes WP1, WP2, WP3 and WP4 inside the model. Data given in full scale

Figure 4.18b shows that the frequency of the side probes is 2ω compared to the fore and aft WP2 and WP4. The amplitudes of the side probes alternate which has the largest amplitude indicating to some additional lower frequency standing wave occuring. For the shortest frequencies, we see clear indications of swirling since all four wave probes in Figure 4.18c show crests over one period of WP2. Further swirling indications are seen when comparing the first, second and third harmonics of the side wave probe WP1 for steepness 1. Figure 4.19 presents the RAO of the side probe WP1 showing all three harmonics for steepness 1.

Figure 4.19: RAO for internal wave probe WP1 in full scale for 1st, 2nd and 3rd harmonics for steepness 1 ($H/\lambda = 1/60$)

At the coupled system frequency $\omega = 1$, the first harmonic has its maximum and is also dominating at the second natural sloshing frequency. These effect are more prominent for steepness 2 and 3, which can be seen in Appendix. The second harmonic, which is connected to non-linearities, is clearly dominant at the sloshing frequency $\omega = 0.93$ for the side internal wave probe WP1 which is visible in the time-series of previous Figure 4.18b. The third harmonic is close to zero for the whole frequency range with a tiny increase around natural sloshing frequency.

General Discussion

The theoretical calculations did not reproduce the experimentally obtained RAO for sloshing. The sloshing amplitude at the sloshing eigenfrequency is very prominent in the calculations, whereas this does not show up as a distinct local maximum in the model test. In the experimental results, near the sloshing eigenfrequency, non-linearities are both visible in the time-series as well as seen present in the 2nd and 3rd harmonics of fore wave probe WP2. The sensitivity analysis also shows that the sloshing calculations are very sensitive to small changes and can give significant amplitude differences by altering the parameters slightly. The sensitivity is observed specially around the sloshing frequency, where a change from 11 to 12 meters of f_z in full scale, increasing the calculated sloshing wave elevation by almost a factor of two from 3.4 to 6.1 meters.

The new RAO calculated with the adjusted values $f_z = 9.3$ meters in full scale and surge multiplication factor 0.8 is much closer to the experimental sloshing RAO. The calculated sloshing amplitudes are highly affected by the input parameters. This means that minor errors in the measuring sensors, inaccuracies in geometrical measurements like f_z or diameter D can lead to large uncertainties in the predicted sloshing amplitudes. The phase angle between the calculated and experimental sloshing amplitude with the adjusted parameters is at -20 degrees as the nearest value. This was unexpected, but reason for this was not found due to lack of time.

This has to be seen in the light of only one test performed. Ideally, multiple repetitions of the model test should be done in order to have a statistical basis for performing an uncertainty analysis and finding standard deviation of the measured parameters like surge or sloshing amplitude. As the sensitivity analysis showed is sensor calibration of significant importance for the theoretical calculations of sloshing using prescribed motions.

The model test showed that even with harmonic regular linear waves and linear rigid-body motions, the sloshing can act non-linearly which cannot be predicted using linear sloshing theory. Figure 4.12, which includes the adjusted parameters, suggests that the calculated

sloshing amplitudes are well predicted from around $\omega = 0.97$ and outwards. The frequencies close to natural sloshing frequency are very sensitive to the input parameters, and will not give correct calculated sloshing amplitudes, even if the accelerations and motions used in the modal function are of linear nature.

However, outside the natural sloshing frequency, linear sloshing theory with few natural modes in practice has shown adequate accuracy when computing surface waves and hydrodynamic loads (Faltinsen and Timokha, 2009). Therefore, if more natural modes would be included, the calculate RAO outside the natural frequency may be even closer to the RAO based on the model test. This means that great care must be taken when predicting the sloshing amplitudes using linear modal theory implemented in a numerical program or by doing theoretical calculations. The sloshing can be over-predicted, especially around the sloshing eigenfrequency.

In our experiment, the largest sloshing amplitude occurred at a frequency 10 % higher than for the theoretical first sloshing natural frequency. The two largest amplitudes where clearly visible for the calculations. However, a dangerous situation may occur if the natural sloshing frequency and the coupled system frequency are close to each other, leading to an amplification of the calculated sloshing wave elevation. If one does not have total control over the different natural frequencies when using linear sloshing theory, discarding the calculations around the natural sloshing frequency, the sloshing at coupled system frequency will be disregarded as well. This will lead to an under-prediction of the sloshing amplitudes. On the other side, if one does not pay attention to the natural sloshing frequency and calculates the sloshing at the coupled system frequency, an over-prediction of the sloshing amplitudes will occur.

The linear modal equation does not include heave motion, however heave motion is coupled to non-linear sloshing. By inspecting the RAO of heave motion, there is actually heave present, probably causing non-linear sloshing modes.

Conclusive Summary and Recommendations for Further Work

In this thesis, the sloshing hydrodynamics inside a floating closed circular cylinder has been inspected. A literature study on the aquaculture industry and sloshing phenomenon was performed, followed by a discussion of potential flow and spectral problem leading to the modal equation which is used to find the theoretical sloshing surface elevation. Further, the dynamics of a rigid-body moving in two degrees of freedom was described. Lastly, a brief approach to the implementation of sloshing in the coupled equation of motion was presented.

The next objective was to present and re-analyze the model test performed in the Fall of 2016 due to added corrections factors and change from Earth-fixed to body-fixed coordinate system. The re-analysis was utilized to compare the calculated sloshing amplitude to the experimental sloshing amplitude. The preliminary results showed that the largest sloshing amplitude occurred at the coupled system frequency $\omega = 1$ which is off by ≈ 10 % from the theoretical first sloshing mode at frequency of $\omega = 0.93$.

The sensitivity analysis performed for the first steepness $H/\lambda = 1/30$ indicated that the calculated sloshing amplitudes are significantly sensitive to the input parameters like surge acceleration and distance between the mean free-surface on the inside of the model and the placement of the accelerometer. The largest variations were visible around the sloshing natural frequency, but also at the coupled system frequency. The adjusted values of $f_z = 9.3$ meters in full scale and surge multiplication factor of 0.8 lead to a closer resemblance between the experimental and calculated RAO of the experiment. The large amplitude at the sloshing frequency was lowered, but the results still showed some variations between the two RAOs at that frequency. Even if the RAOs were much closer to each other, the phase angles between the calculated and experimental sloshing amplitudes were still 20 degrees off.

Further, the non-linear analysis showed a that the time-series of the sloshing wave elevation

was affected by non-linearities around the sloshing natural frequency. The non-linearities were clearly visible in the time-series plot as well as in the RAO for the 1st and 2nd harmonic. The frequencies that did not give any 2nd harmonic response further away from the natural sloshing frequencies showing a closer resemblance between the calculated sloshing amplitudes and experimental sloshing amplitudes. The RAO of the side wave probe inside the model showed a large amplitude for the second harmonic at the natural sloshing frequency, which was also visible from the time-series plot of the sloshing amplitudes.

The last objective concerning the coupled analysis of the eigenvalue problem was not reached due time spent on investigating the differences and finding reasons for why calculated and experimental results did not coincide. This did not leave any more time for further analysis of the coupled system.

6.1   Recommendations for Further Work

Even though a great effort has been made to explore the sloshing dynamics of a closed fish farm structure, further studies should be done regarding both numerical and experimental tests.The recommendations for further work are presented point-wise below

- Carry out additional model test runs with additional accelerometers in x-direction to perform statistical analysis of data and calculate precision error.

- Since linear conditions were applied for the outer problem, linear response was expected for the inner problem. The model test did show non-linearities for the inner problem. Therefore, further investigation into non-linear sloshing theory is recommended.

- Perform additional model tests with varying diameter to investigate if and how the sloshing problem can be controlled and handled in the design phase.

- Carry out additional experiment with solid mass to determine RAOs without sloshing for comparison.

- Continue looking in to the eigenvalue problem of coupled motion.

References

(2016). The state of world fisheries and aquaculture 2016. *Food and Agriculture Organization of the Unites Nations, Rome.*

Abramson, H. N. (1966). *The Dynamic Behavior of Liquids in Moving Containers, with Applications to Space Vehicle Technology.* United States, Hoboken, NJ, 1st edition.

Bass, R. L., Bowles, J. E. B., Trudell, R. W., Navickas, J., Peck, J. C., Yoshimura, N., Endo, S., and Pots, B. F. M. (1985). Modeling criteria for scaled lng sloshing experiments. *Journal of Fluids Engineering,* 107(2):272–280.

Brugère, C. and Ridler, N. (2004). Global aquaculture outlook in the next decades: an analysis of national aquaculture production forecasts to 2030.

Chakrabarti, S. K. (1993). Internal waves in a large offshore storage tank. *Journal of Energy Resources Technology,* 115(2):133–141.

Crawford, C. and MacLeod, C. (2009). *Predicting and assessing the environmental impact of aquaculture,* pages 679–747. CRC Press.

(DKNVS), D. K. N. V. S. and (NTVA), N. T. V. (2016). Verdiskaping basert på produktive hav i 2050. `https://www.sintef.no/globalassets/upload/fiskeri_og_havbruk/publikasjoner/verdiskaping-basert-pa-produktive-hav-i-2050.pdf/`. [Accessed Online: 21.11.2016].

Edwards, P. (2015). Aquaculture environment interactions: Past, present and likely future trends. *Aquaculture,* 447:2 – 14. Research for the Next 40 Years of Sustainable Global Aquaculture.

Faltinsen, O. M. (1974). A nonlinear theory of sloshing in rectangular tanks. *Journal of Ship Research,* 18(4):224–241.

Faltinsen, O. M. (1990). *Sea Loads on Ships and Offshore Structures.* Cambridge University Press.

Faltinsen, O. M. and Timokha, A. N. (2009). *Sloshing*. Cambridge University Press.

Fiskedirektoratet.no (2016). Oversikt over søknader om utviklingstillatelser per 24. august 2016. [Accessed Online: December 12, 2016].

Helling, K., Hausmann, S., Clarke, A., and Scherer, H. (2003). Experimentally induced motion sickness in fish: Possible role of the otolith organs. *Acta Oto-Laryngologica*, 123(4):488–492.

Kyst.no (2016). Satt ut smolt i lukket merd. [Accessed Online: 6. June, 2017].

Laksefakta.no (2016). Norsk havbrukshistorie. `https://laksefakta.no/`. [Online; accessed November 16, 2016].

Larsen, C. M. (2014). *TMR 4182 Marine Dynamics*. Department of Marine Technology, .pdf format.

Miles, J. W. (1974). Harbor seiching. *Annual Review of Fluid Mechanics*, 6(1):17–33.

Monteiro, P. V. and Salvador, R. (2014). *Main challenges facing the aquaculture sector: From a worldwide insight to a regional perspective*, pages 165–174. CRC Press.

Olsen, Y., Otterstad, O., and Duarte, C. M. (2008). *Status and Future Perspectives of Marine Aquaculture*, pages 293–319. Springer Netherlands, Dordrecht.

Rafiee, A., Pistani, F., and Thiagarajan, K. (2011). Study of liquid sloshing: numerical and experimental approach. *Computational Mechanics*, 47(1):65 – 75.

Rognebakke, O. F. and Faltinsen, O. (2003). Effects of sloshing on ship motions. *Journal of Ship Research*, 47(3):208–221.

Shainee, M., Ellingsen, H., Leira, B., and Fredheim, A. (2013). Design theory in offshore fish cage designing. *Aquaculture*, 392–395:134 – 141.

SINTEF (2016-2017). SjØflo – sjøegenskaper og forankring til flytende lukkede oppdrettsanlegg. `http://www.sintef.no/prosjekter/sjoflo/`. [Accessed Online: June 1, 2017].

Solaas, F. (1995). Analytical and numerical studies of sloshing in tanks. *(Trondheim : trykt utg.) 1995:103 ; MTA (trykt utg.) 1995:107*.

SSB.no (2016). Eksport av laks, veke 48 2016. `http://www.ssb.no/utenriksokonomi/statistikker/laks/uke/2016-12-07#content`. [Online; accessed December 12, 2016].

Sveälv, T. (1988). Inshore versus offshore farming. *Aquacultural Engineering*, 7(4):279–287. cited By 15.

Appendix A: Froude Scaling Laws

Table A.1: Froude Scaling Laws. λ is given as the scale, ρ_F and ρ_M are the densities for model and full-scale respectively.

Physical Paramers	Unit	Multiplication factor
Length	[m]	λ
Structural mass	[kg]	$\lambda^3 \frac{\rho_F}{\rho_M}$
Force	[N]	$\lambda^3 \frac{\rho_F}{\rho_M}$
Moment	[Nm]	$\lambda^4 \frac{\rho_F}{\rho_M}$
Acceleration	[m/s^2]	$a_F = a_M$
Time	[s]	$\sqrt{\lambda}$
Pressure	[N/m^2]	$\lambda \frac{\rho_F}{\rho_M}$

Appendix B: First Steps in Numerical Modelling

In this chapter we look at numerical modelling. There are numerous of commercial programs which can be used for this application. As we are looking at linear sloshing and sloshing in general, we do not consider viscous forces as they are negligible in magnitude. To model and evaluate the structure hydrodynamically in this case, DNV GL's SESAM package is used. Within this package, the hydrodynamic coefficients of the structure can be generated using HydroD's WADAM with a generated mesh from GeniE. From WADAM we get the hydrodynamic coefficients of the outer problem. Table B.1 presents the main parameters used for the model. We assume the enclosed water volume to be solid.
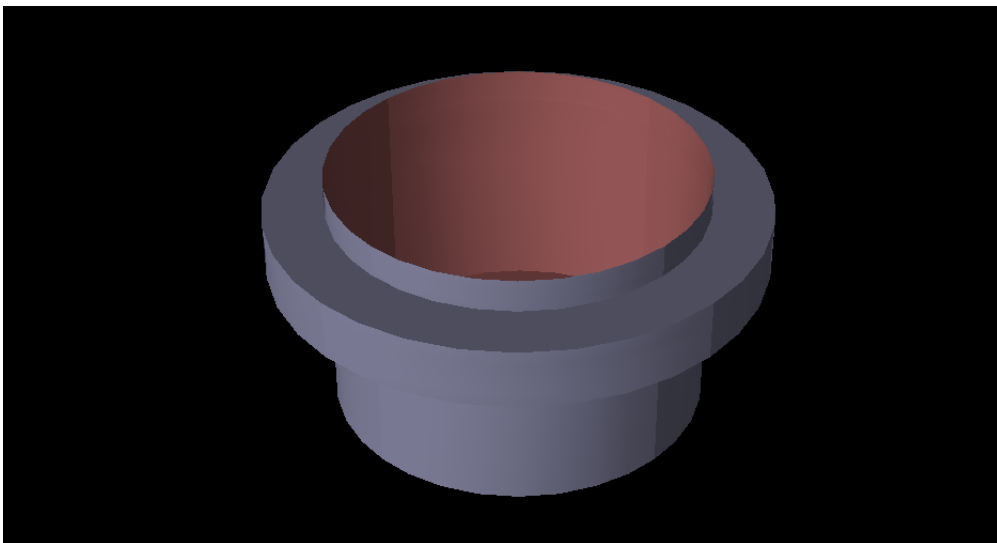
Figure B.1: Geometrical model as shown in GeniE. The red and blue distinguish the direction of the normal vector. The floating collar is also attached.

Table B.1: List of dimensions of the full scale structure used for comparison to experimental results

Symbol	Value	Dimensions
H	22	[m]
h	16.7	[m]
R_0	4.5	[m]
D	1	[m]
V	1	[m^3]
ρ	1025	[kg/m^3]

B.1   Meshing

After the geometrical properties are established, the cell size can be investigated. The mesh is chosen so that the computational time is within reason without sacrificing too much accuracy of the results. The mesh is uniformly distributed. The amount of mesh grids was also limited by the numerical calculations of WADAM, which did not run with more than about 15 000 cells. Therefore, it was important not to exceed this value, however still get desirable results. For the meshing of the structure, SESAM GeniE is used to define the boundaries used for further hydrodynamical analysis. Mesh chosen mesh is 1.0 m as reference, although a mesh refinement analysis will be applied in order to secure quickest computing time with an adequate accuracy.
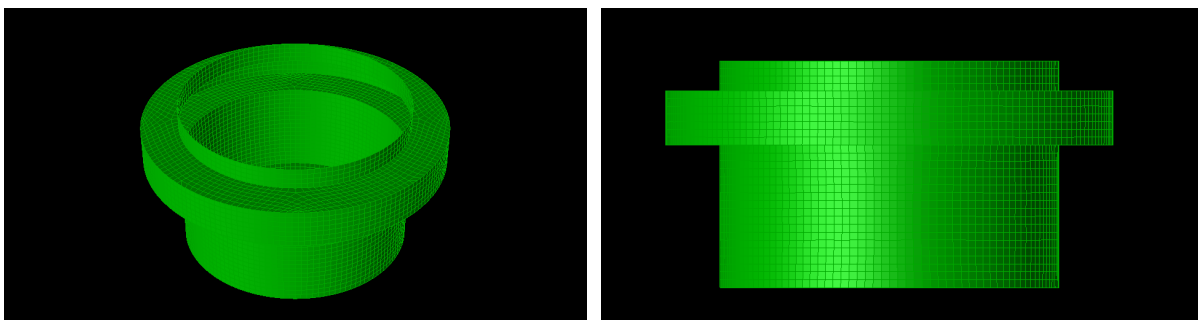
(a) Geometry with collar with mesh size 1 m.   (b) Same geometry from side view.

Figure B.2: Meshed structure from two points of view.

B.1.1   WADAM

HydroD is a SESAM package for hydrostatic and hydrodynamic analysis. The hydrodynamic analysis is performed by calculating hydrodynamic coefficients, excitation forces, accelerations etc. WADAM is based on Wave Analysis Masaschussetts Institute of Technology (WAMIT) which uses plane quadrilateral panels and constant strength sources over each panel. For further details, see WADAM user manual. WADAM calculations are performed in frequency domain.

From HydroD we fant to find the frequency dependant added mass and restoring forces WADAM is used for hydrodynamic analysis without forward speed is able to calculate the hydrodynamic coefficients calculated using potential wave theory and sink/source techniques. A frequency domain run is performed in order to calculate all of the needed coefficients, including $A_{11}, A_{15}, A_{51}, A_{55}$ as well as the mass matrix and restoring matrix.

Appendix C: Time-Series Pitch
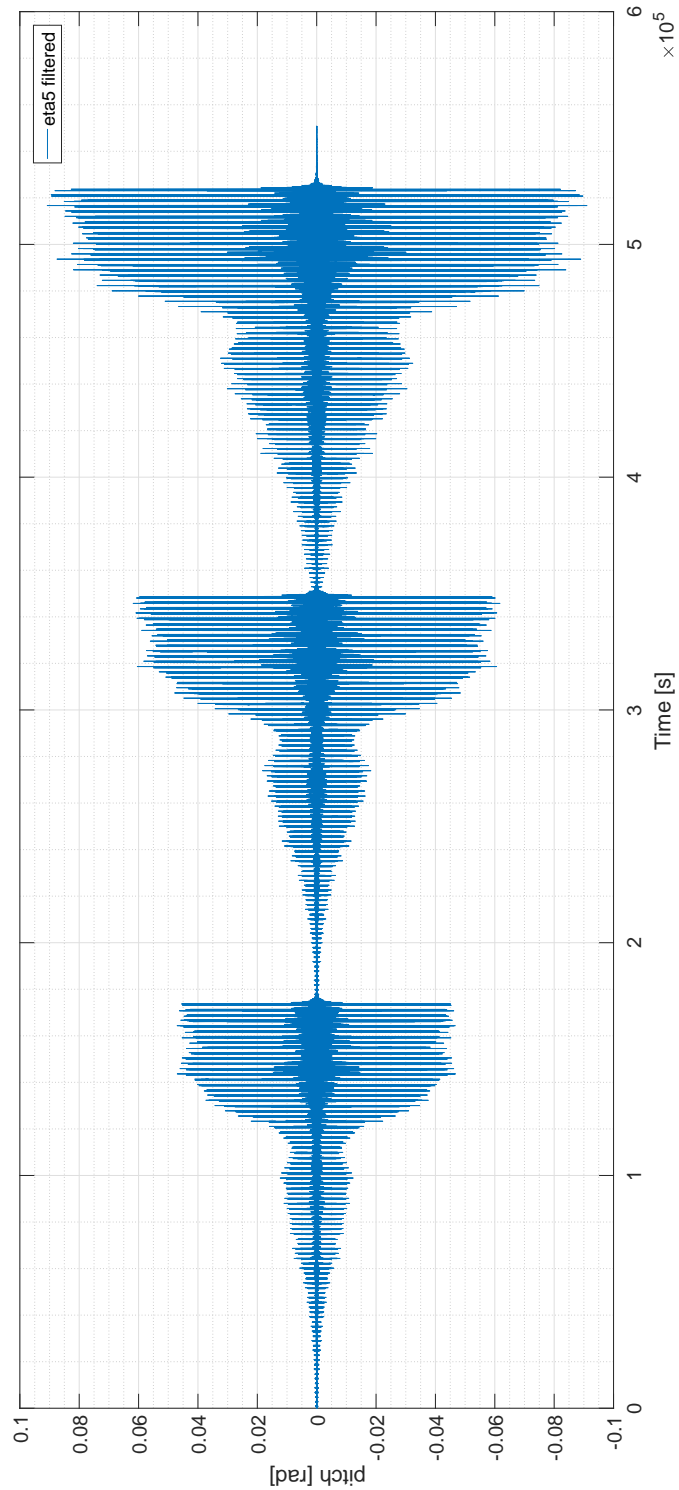
Figure C.1: total time-series of pitch given in full scale. The test is performed for 3 steepnesses H/λ = 1/30, 1/45 and 1/60. The period ranges between T ∈ [3.6, 7.2] s in full scale.

Appendix D: Time-Series Surge
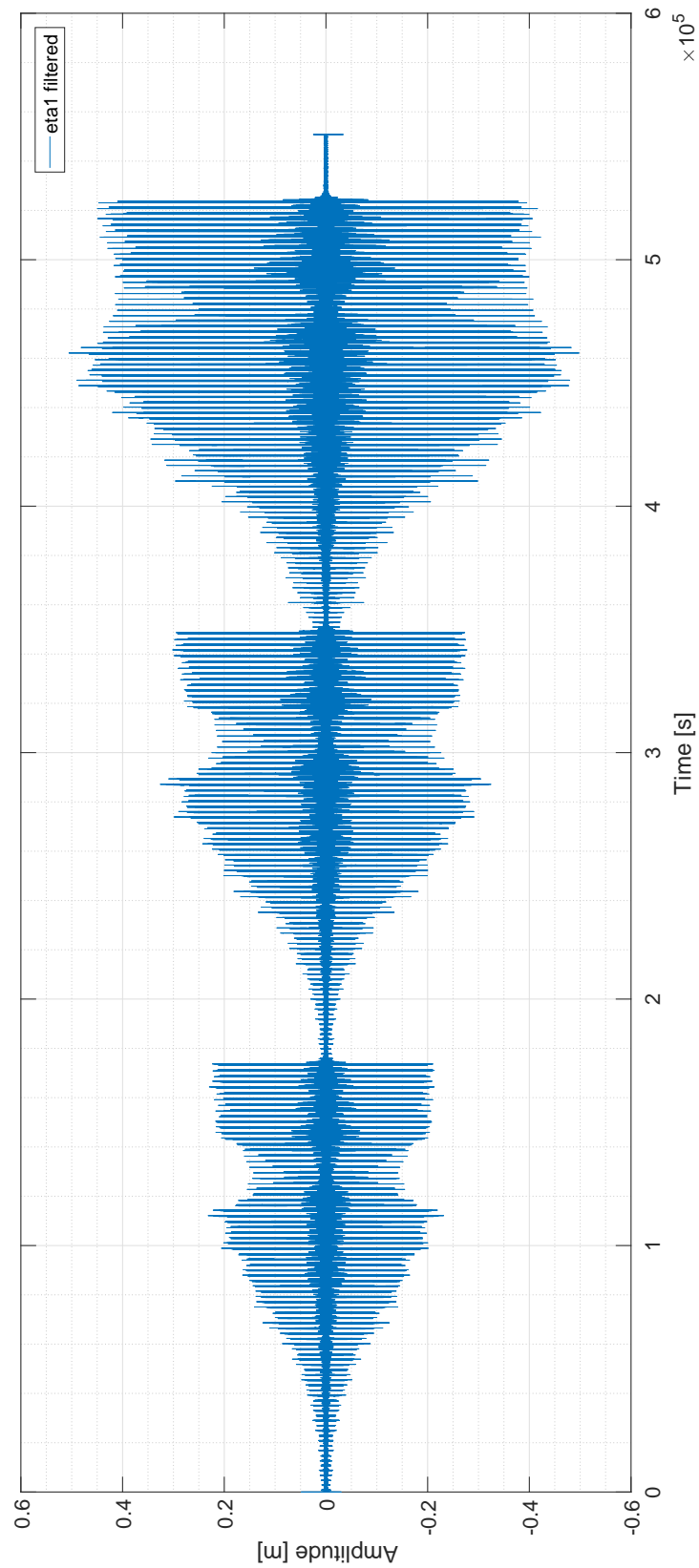
Figure D.1: total time-series of surge given in full scale. The test is performed for 3 steepnesses H/λ = 1/30, 1/45 and 1/60. The period ranges between T $\in$ [3.6, 7.2] s in full scale.

Appendix E: Time-series Heave
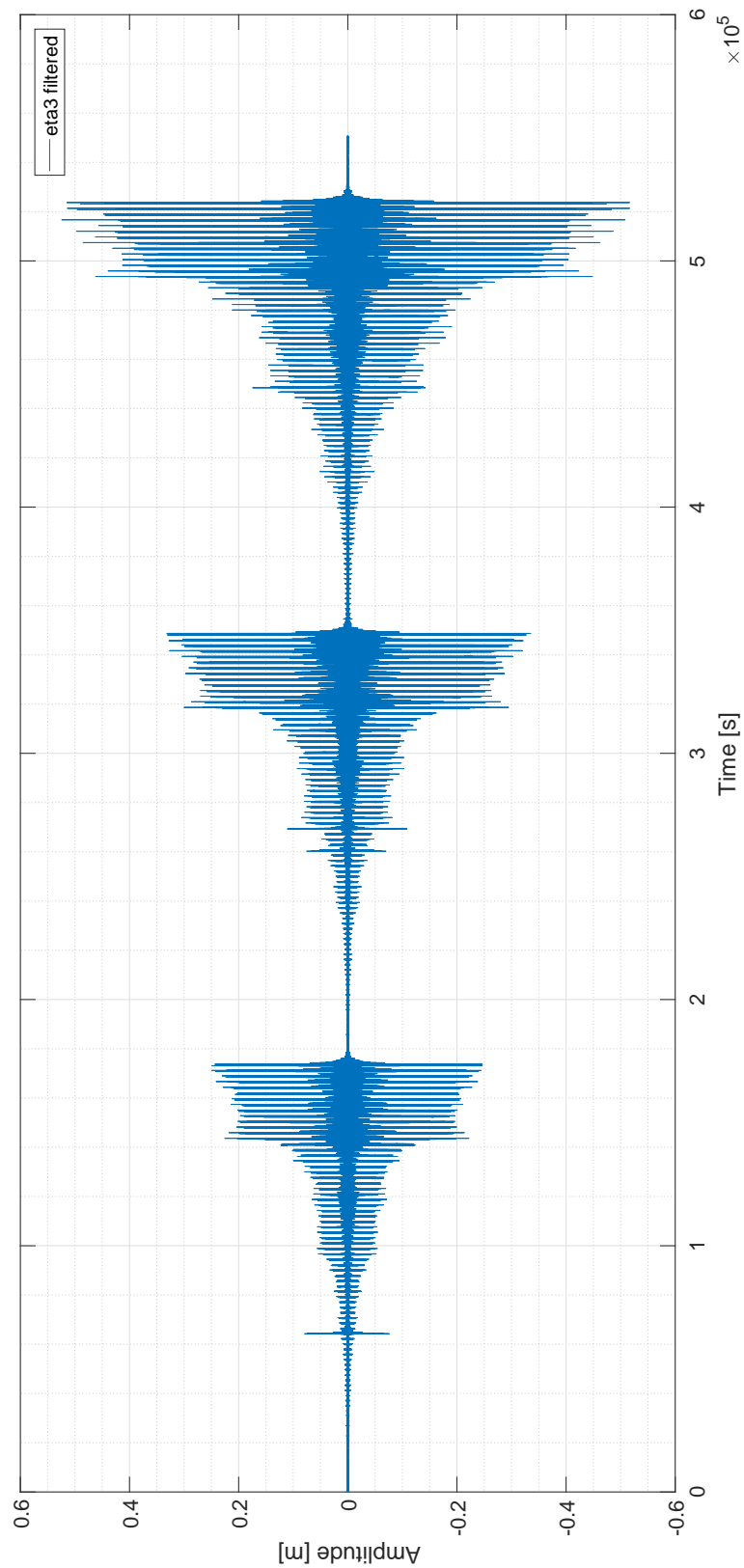
Figure E.1: total time-series of heave given in full scale. The test is performed for 3 steepnesses H/λ = 1/30, 1/45 and 1/60. The period ranges between T ∈ [3.6, 7.2] s in full scale.

Appendix F: Remaining Results

F.1 1st, 2nd and 3rd Harmonics for WP1-4 for Steepness H/λ = 1/60, 1/45 and 1/30
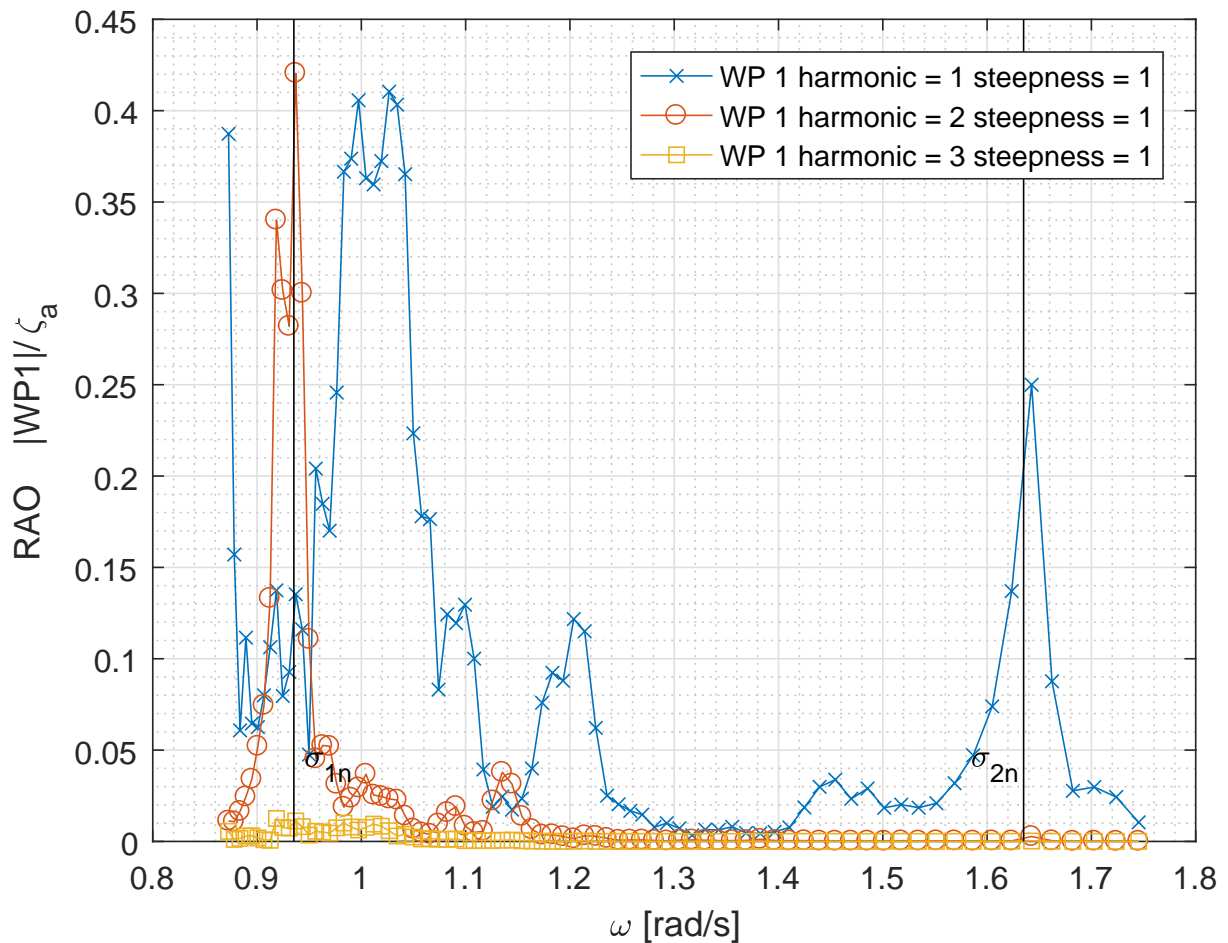
Figure F.1: RAO for internal wave probe WP1 in full scale for 1st, 2nd and 3rd harmonic for wave steepness $H/\lambda = 1/60$. The black vertical lines represent the first and second modal natural sloshing frequency.
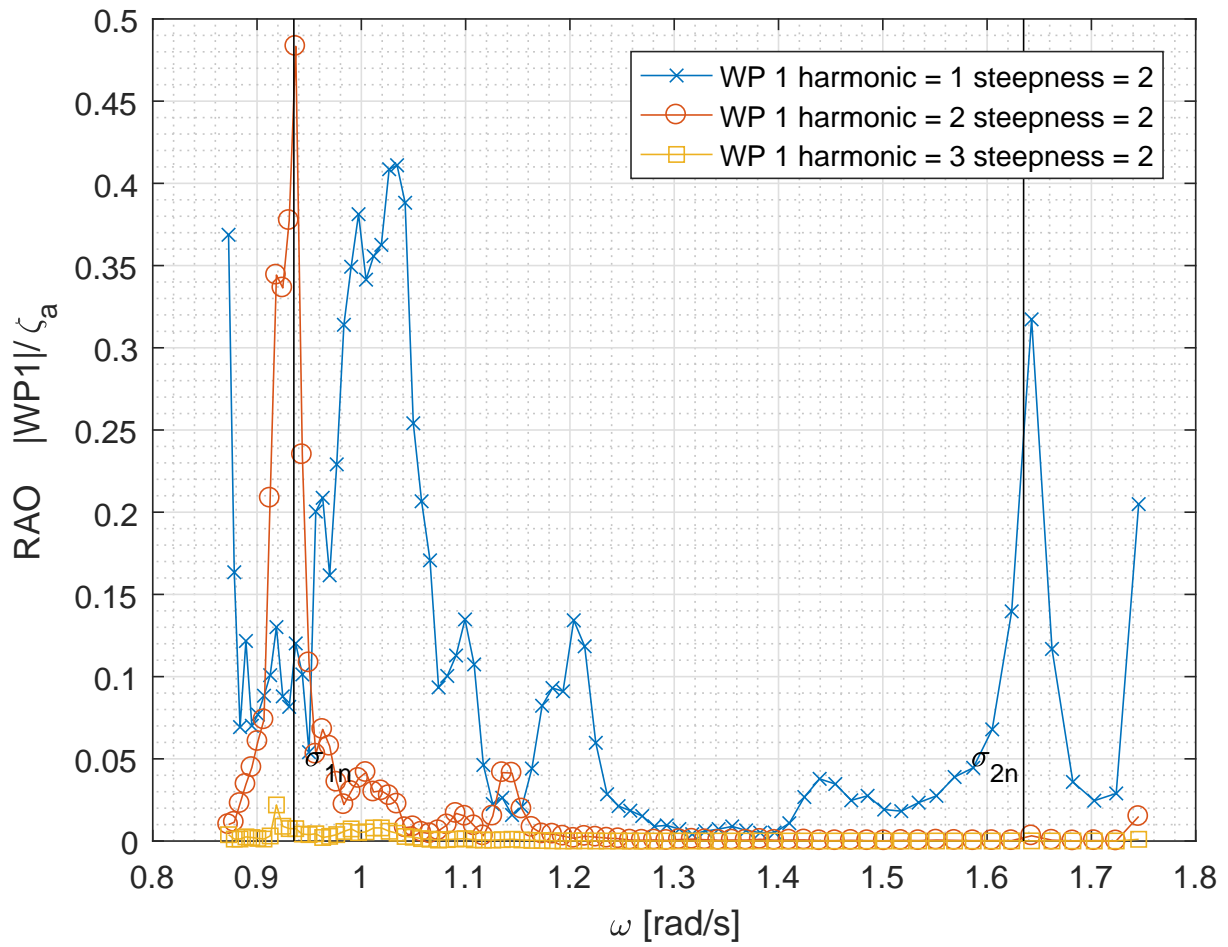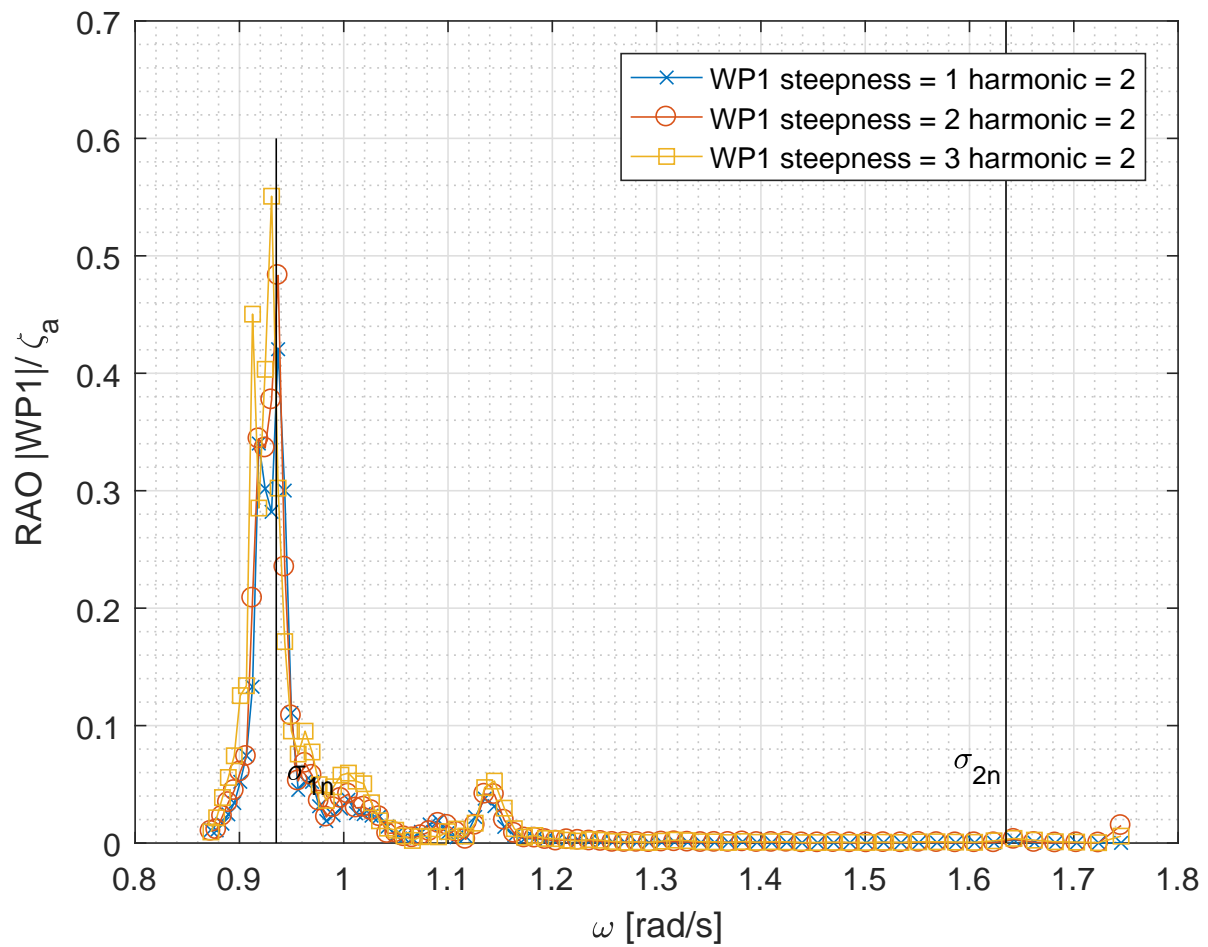
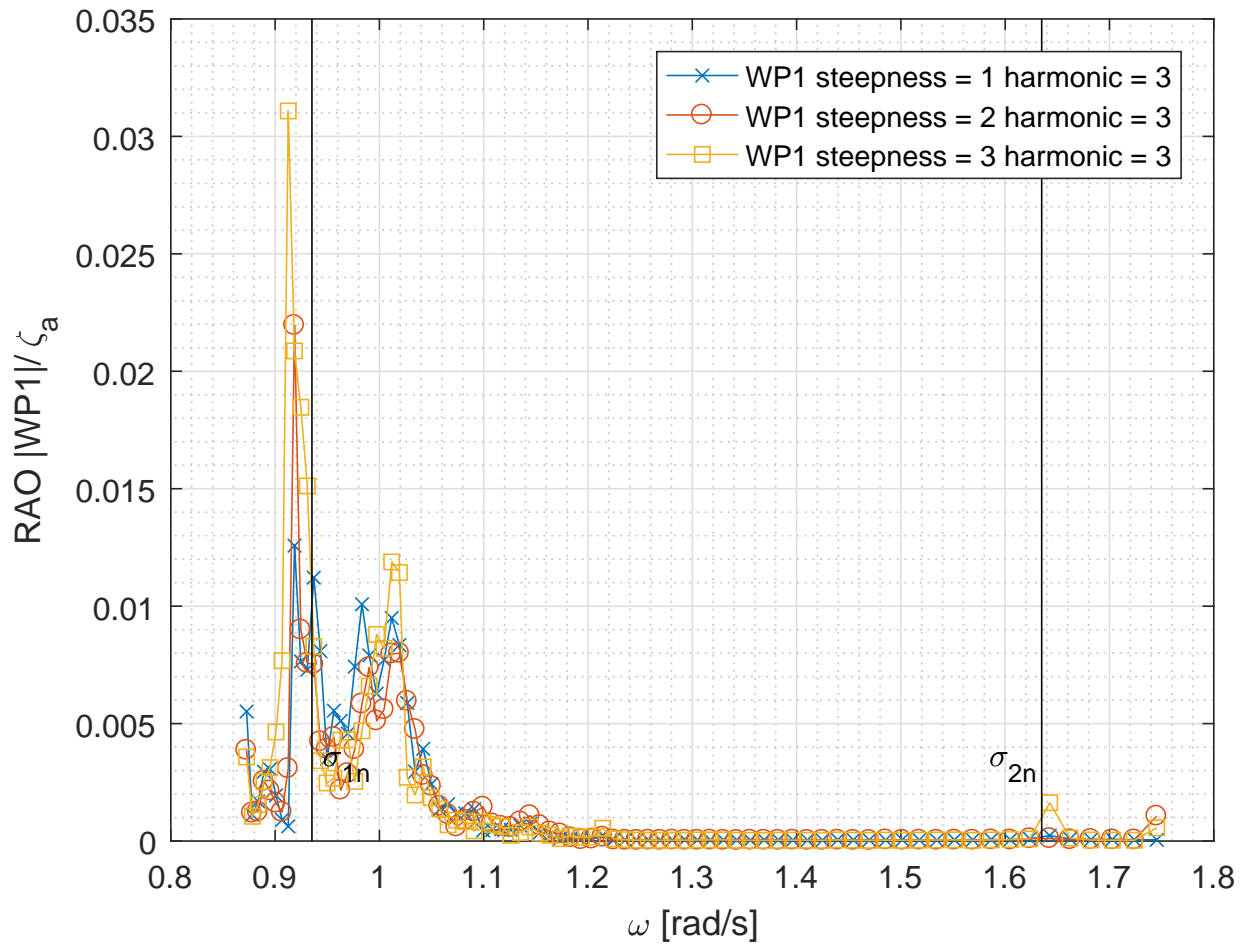Figure F.2: RAO for internal wave probe WP1 in full scale for 1st, 2nd and 3rd harmonic for steepness 1 ($H/\lambda = 1/45$). The black vertical lines represent the 1st and 2nd modal nat. sloshing freq.
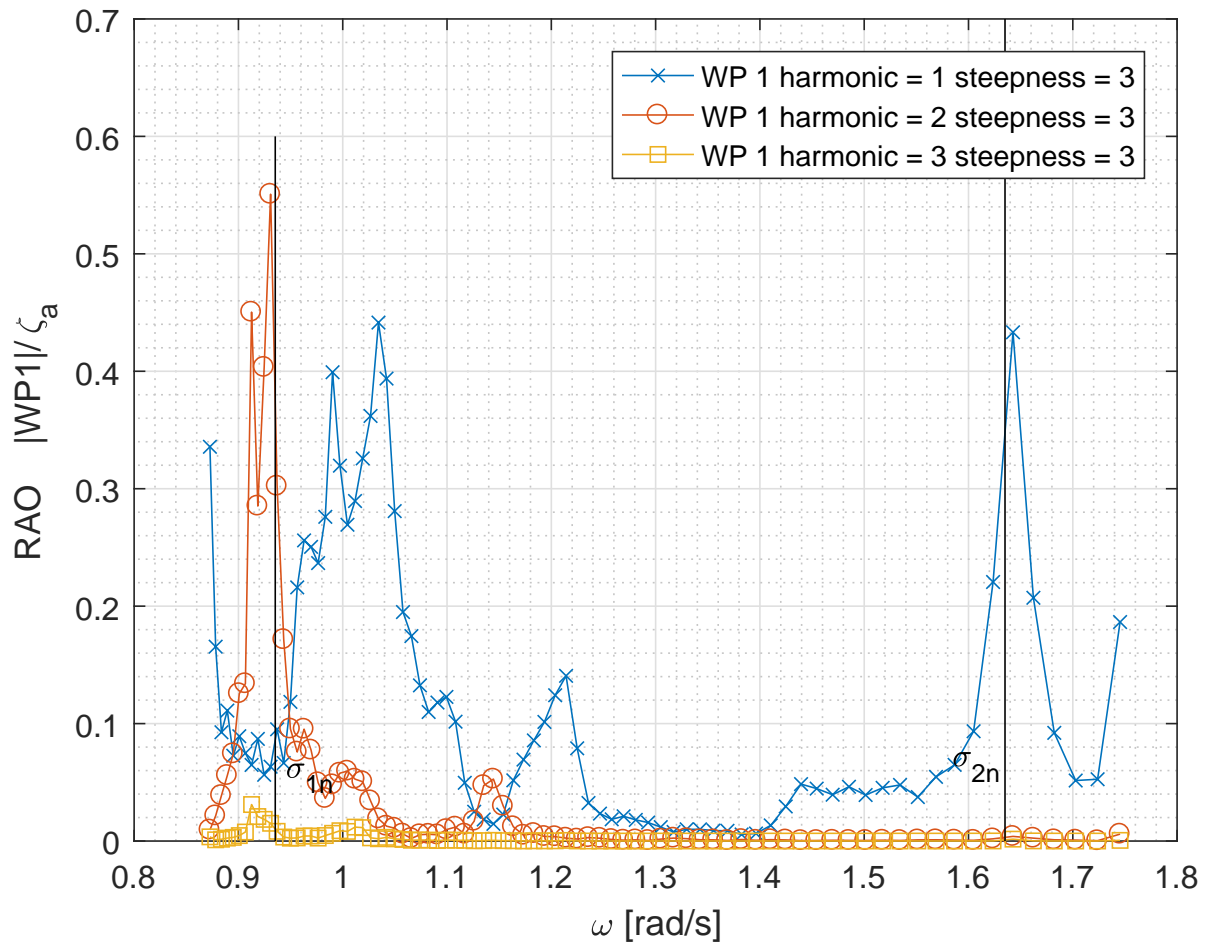
Figure F.3: RAO for internal wave probe WP1 in full scale for 1st, 2nd and 3rd harmonic for wave steepness $H/\lambda = 1/30$. The black vertical lines represent the first and second modal natural sloshing frequency.
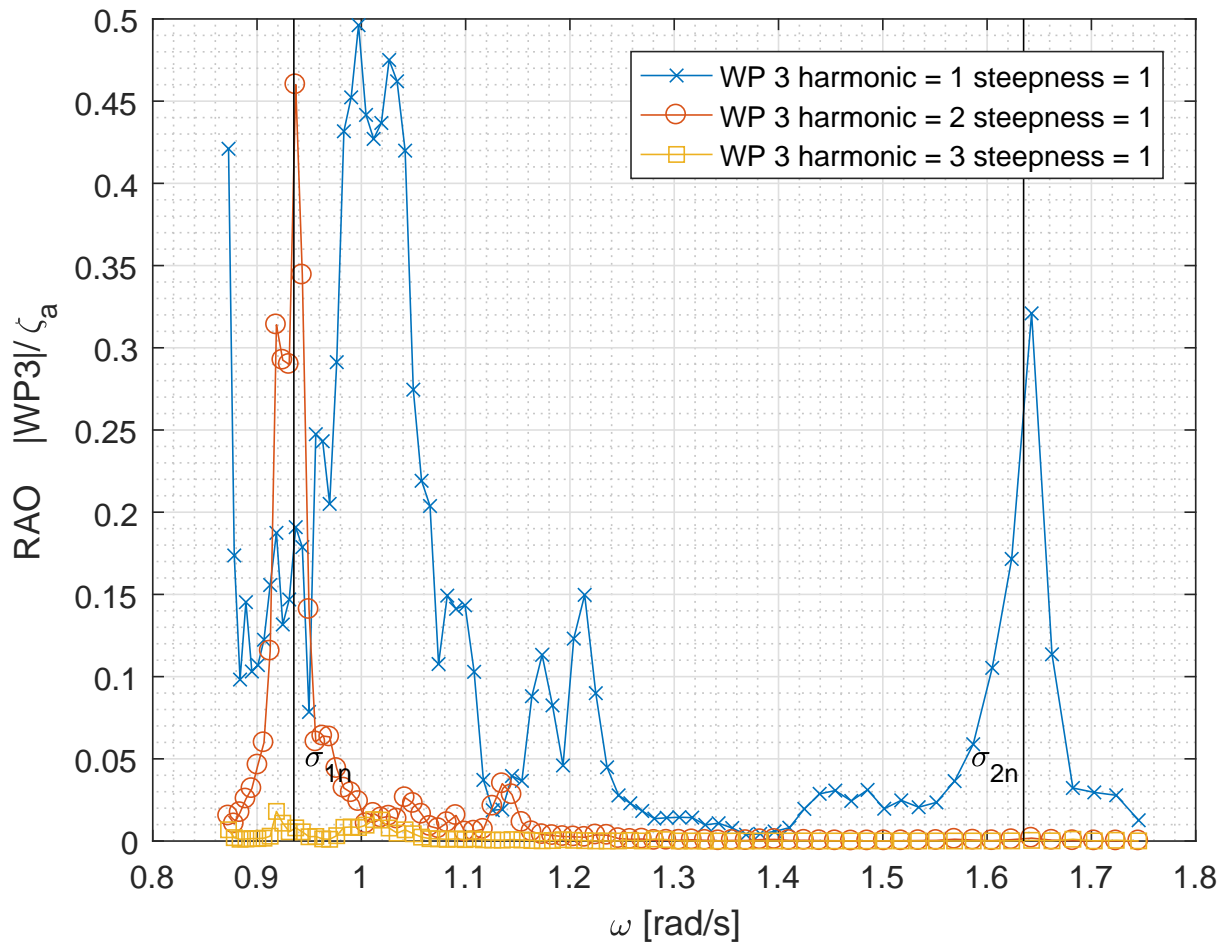
Figure F.4: RAO for internal wave probe WP3 in full scale for 1st, 2nd and 3rd harmonic for wave steepness $H/\lambda = 1/60$. The black vertical lines represent the first and second modal natural sloshing frequency.
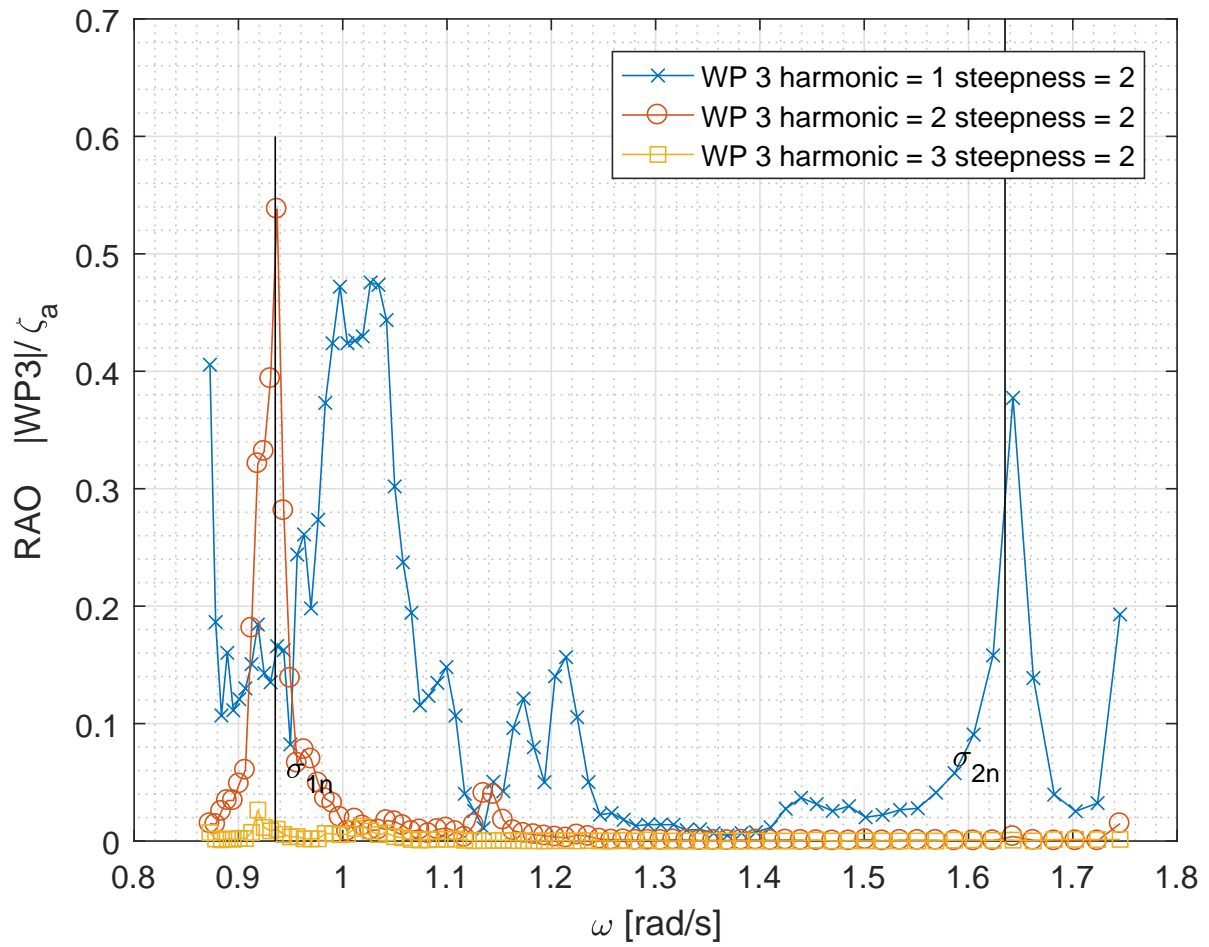
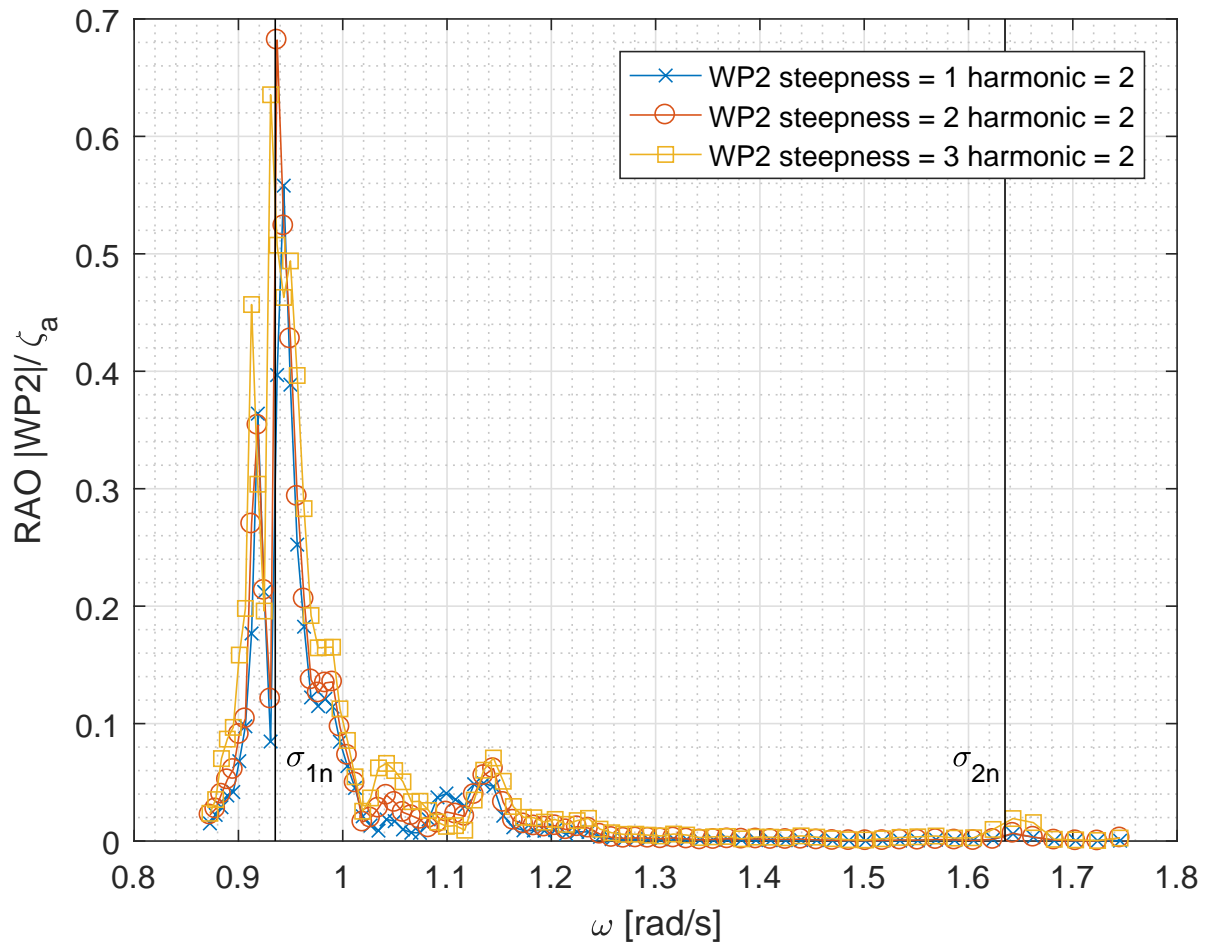Figure F.5: RAO for internal wave probe WP3 in full scale for 1st, 2nd and 3rd harmonic for wave steepness $H/\lambda = 1/45$. The black vertical lines represent the first and second modal natural sloshing frequency.
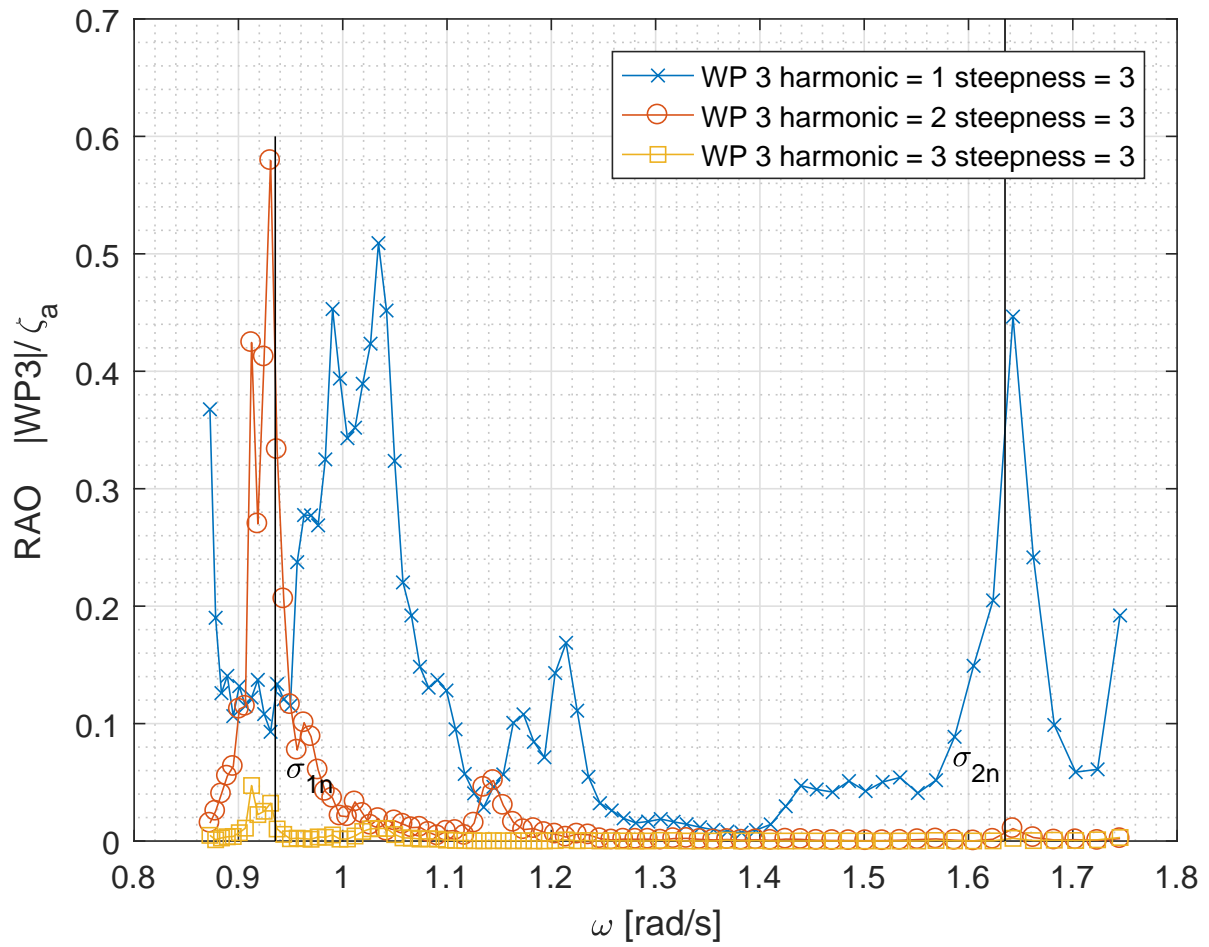
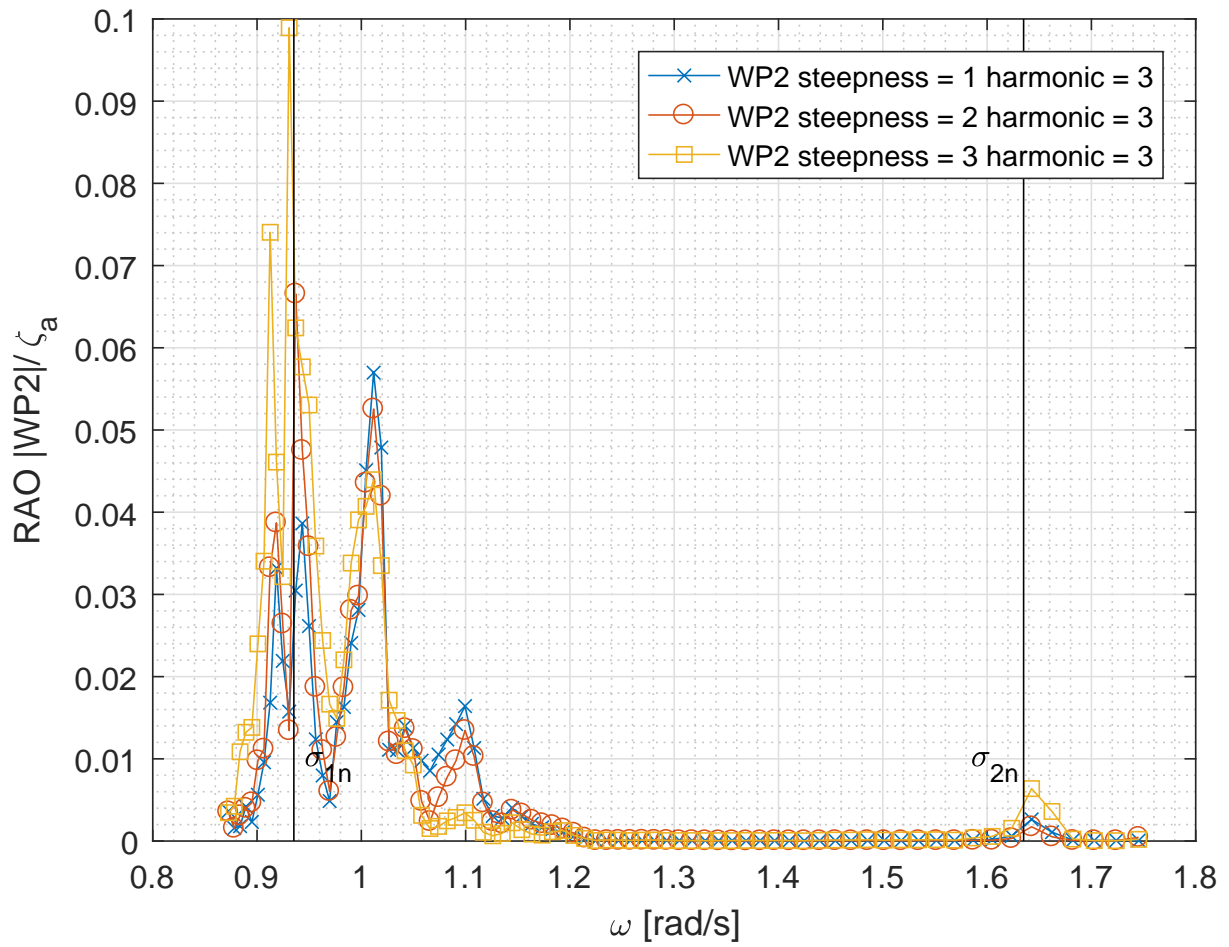Figure F.6: RAO for internal wave probe WP3 in full scale for 1st, 2nd and 3rd harmonic for wave steepness $H/\lambda = 1/30$. The black vertical lines represent the first and second modal natural sloshing frequency.

Figure F.7: RAO for internal wave probe WP4 in full scale for 1st, 2nd and 3rd harmonic for wave steepness $H/\lambda = 1/60$. The black vertical lines represent the first and second modal natural sloshing frequency.

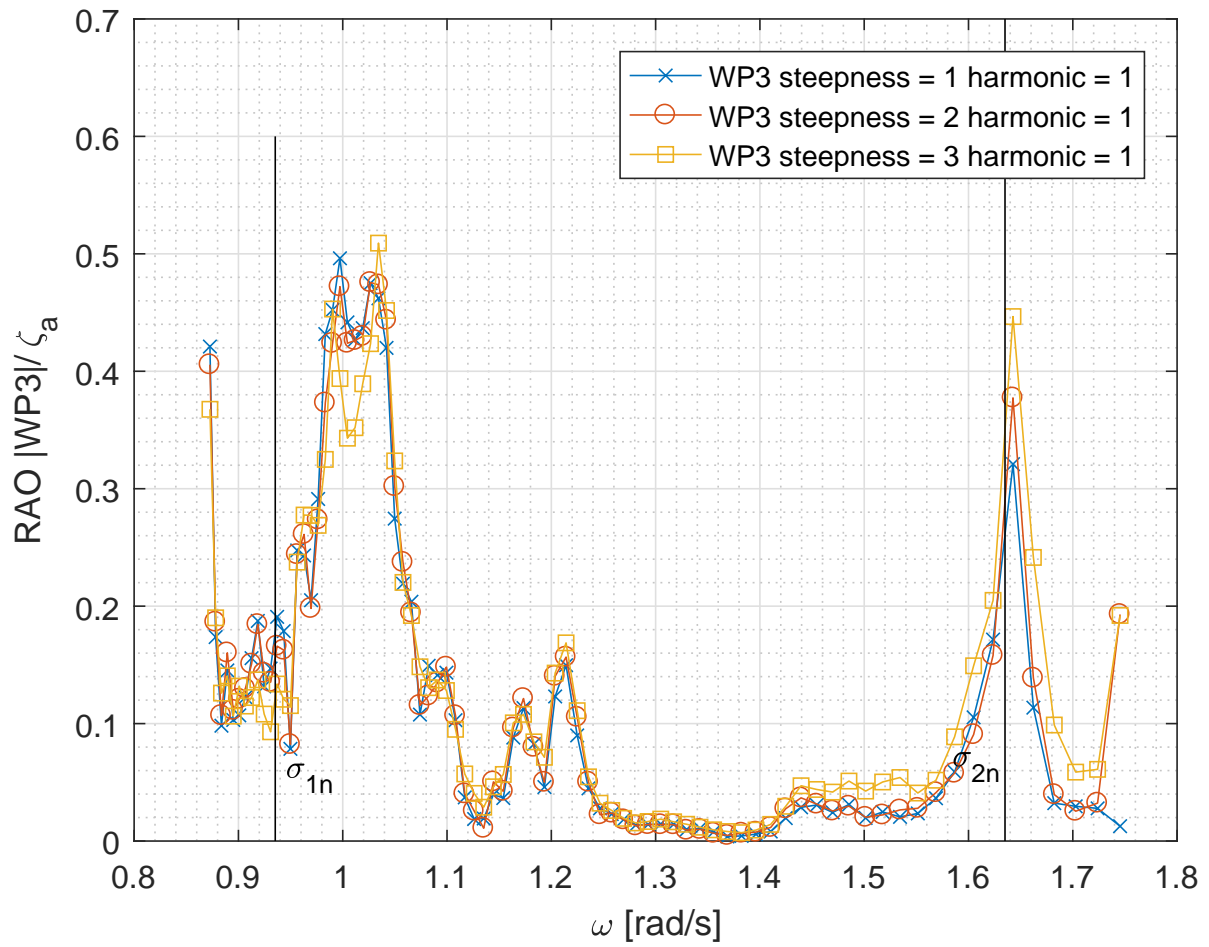Figure F.8: RAO for internal wave probe WP4 in full scale for 1st, 2nd and 3rd harmonic for wave steepness $H/\lambda = 1/45$. The black vertical lines represent the first and second modal natural sloshing frequency.

Figure F.9: RAO for internal wave probe WP4 in full scale for 1st, 2nd and 3rd harmonic for wave steepness $H/\lambda = 1/30$. The black vertical lines represent the first and second modal natural sloshing frequency.

F.2 Steepness Comparison for 1st, 2nd and 3rd harmonic
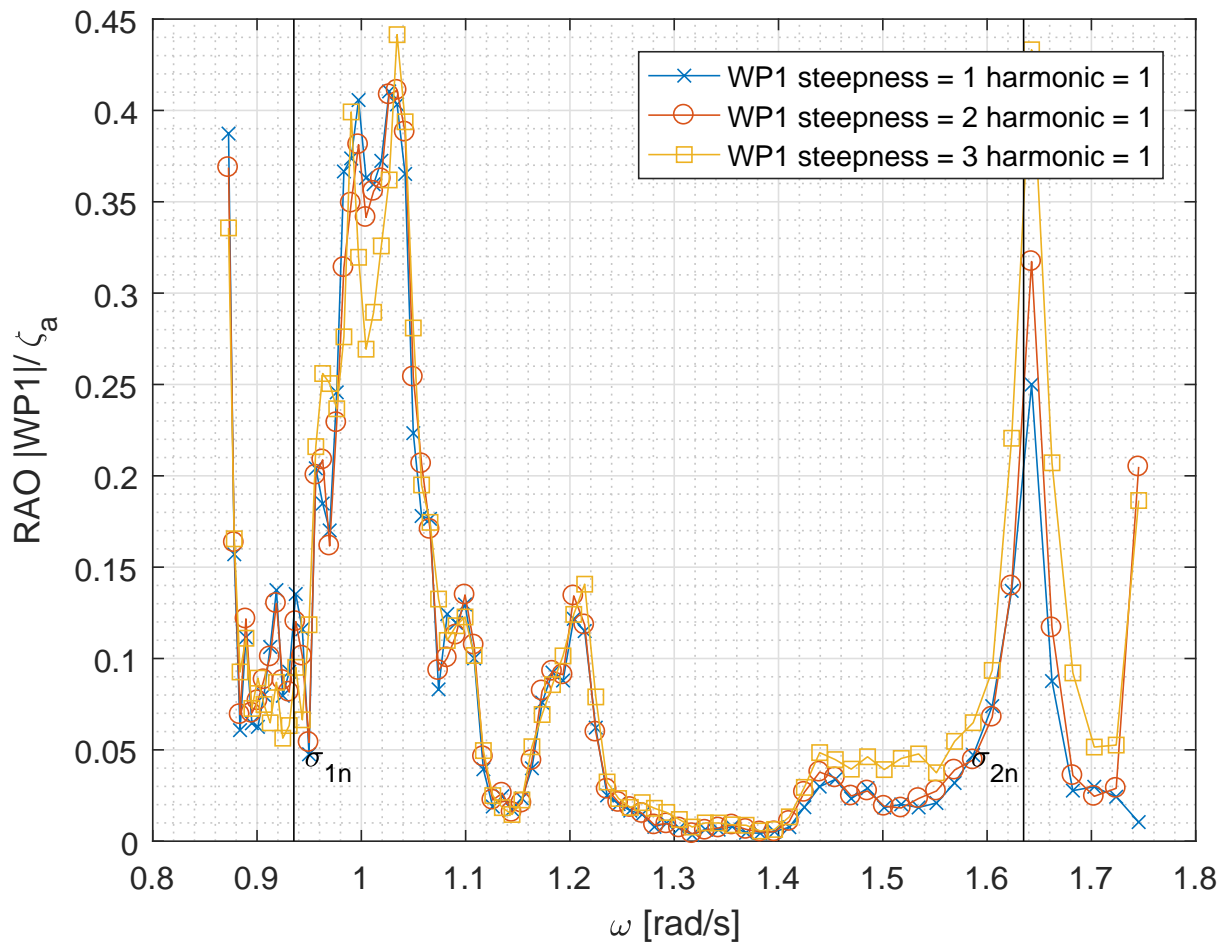
Figure F.10: RAO for internal wave probe WP1 in full scale for 1st harmonic for wave steepness $H/\lambda = 1/30$, $1/45$ and $1/60$. The black vertical lines represent the first and second modal natural sloshing frequency.
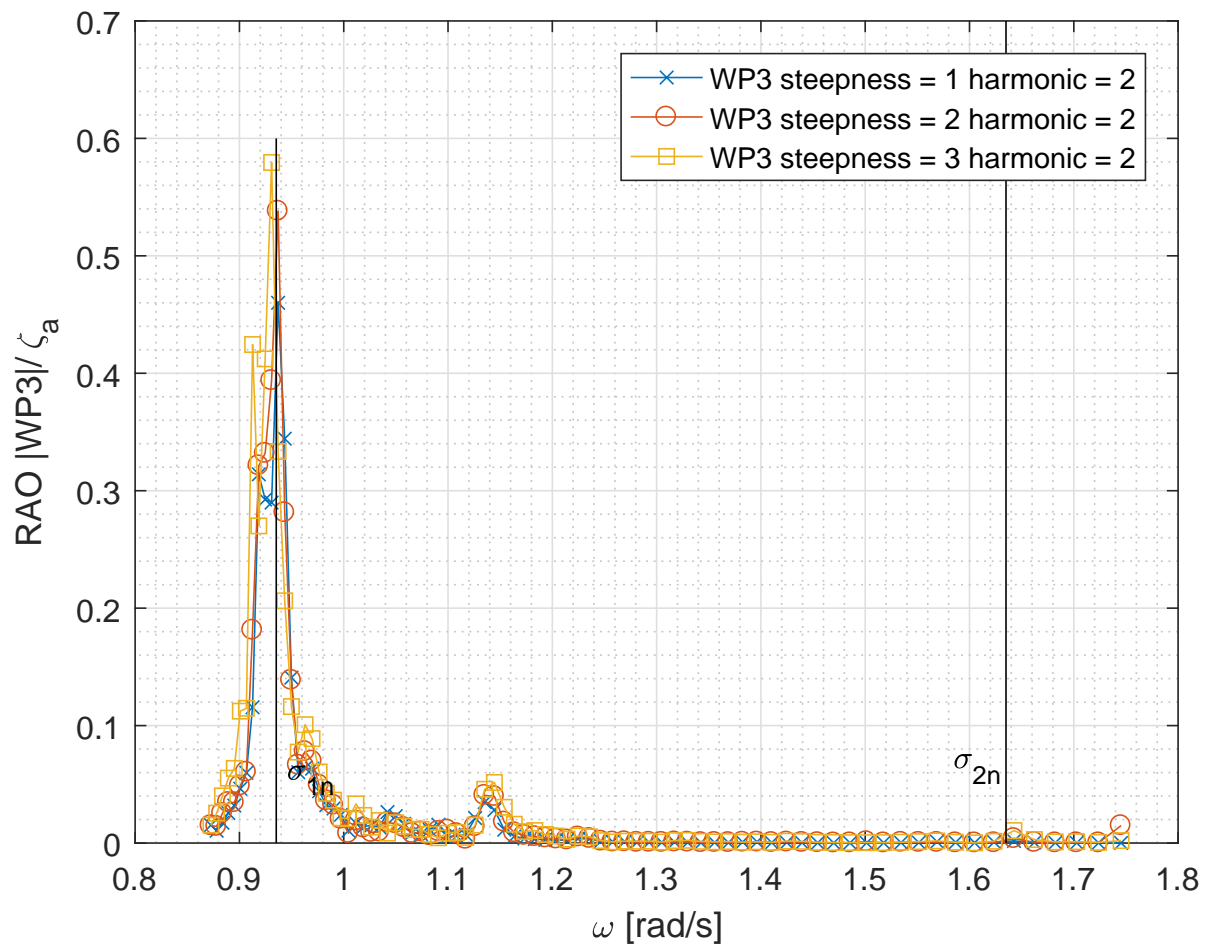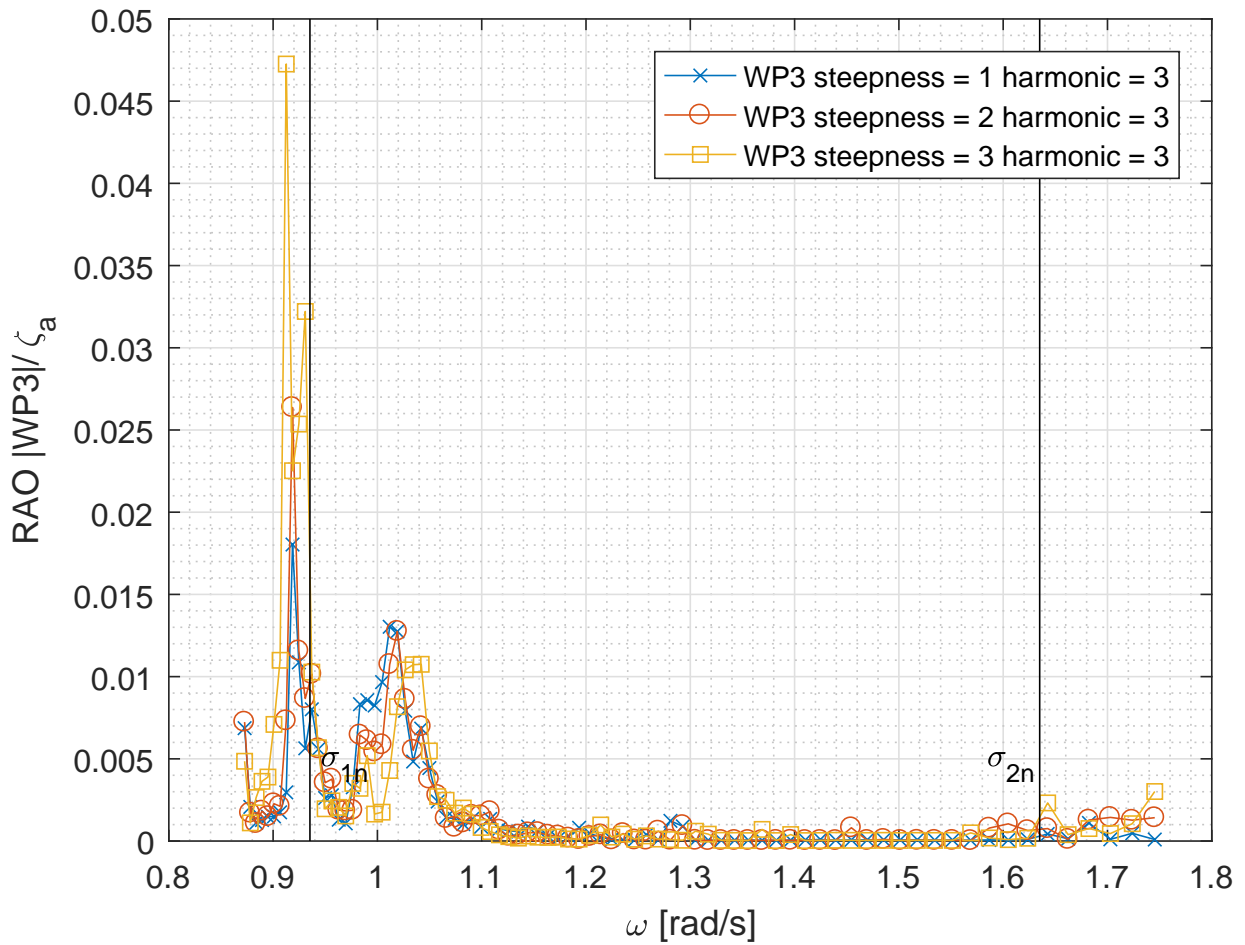
Figure F.11: RAO for internal wave probe WP1 in full scale for 2nd harmonic for wave steepness $H/\lambda = 1/30$, $1/45$ and $1/60$. The black vertical lines represent the first and second modal natural sloshing frequency.

Figure F.12: RAO for internal wave probe WP1 in full scale for 3rd harmonic for wave steepness $H/\lambda = 1/30$, $1/45$ and $1/60$. The black vertical lines represent the first and second modal natural sloshing frequency.
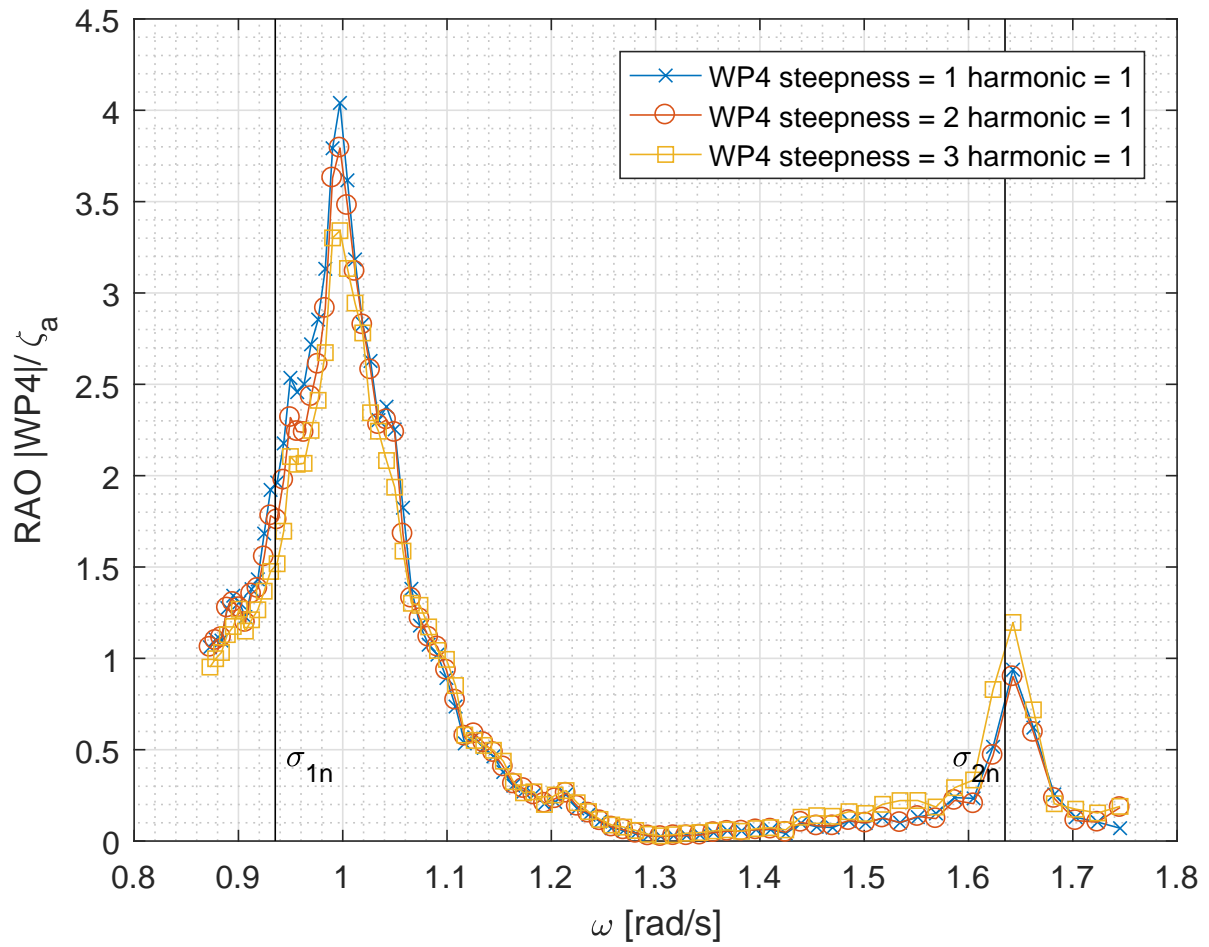
Figure F.13: RAO for internal wave probe WP2 in full scale for 1st harmonic for wave steepness $H/\lambda = 1/30$, $1/45$ and $1/60$. The black vertical lines represent the first and second modal natural sloshing frequency.

Figure F.14: RAO for internal wave probe WP2 in full scale for 3nd harmonic for wave steepness $H/\lambda = 1/30$, $1/45$ and $1/60$. The black vertical lines represent the first and second modal natural sloshing frequency.
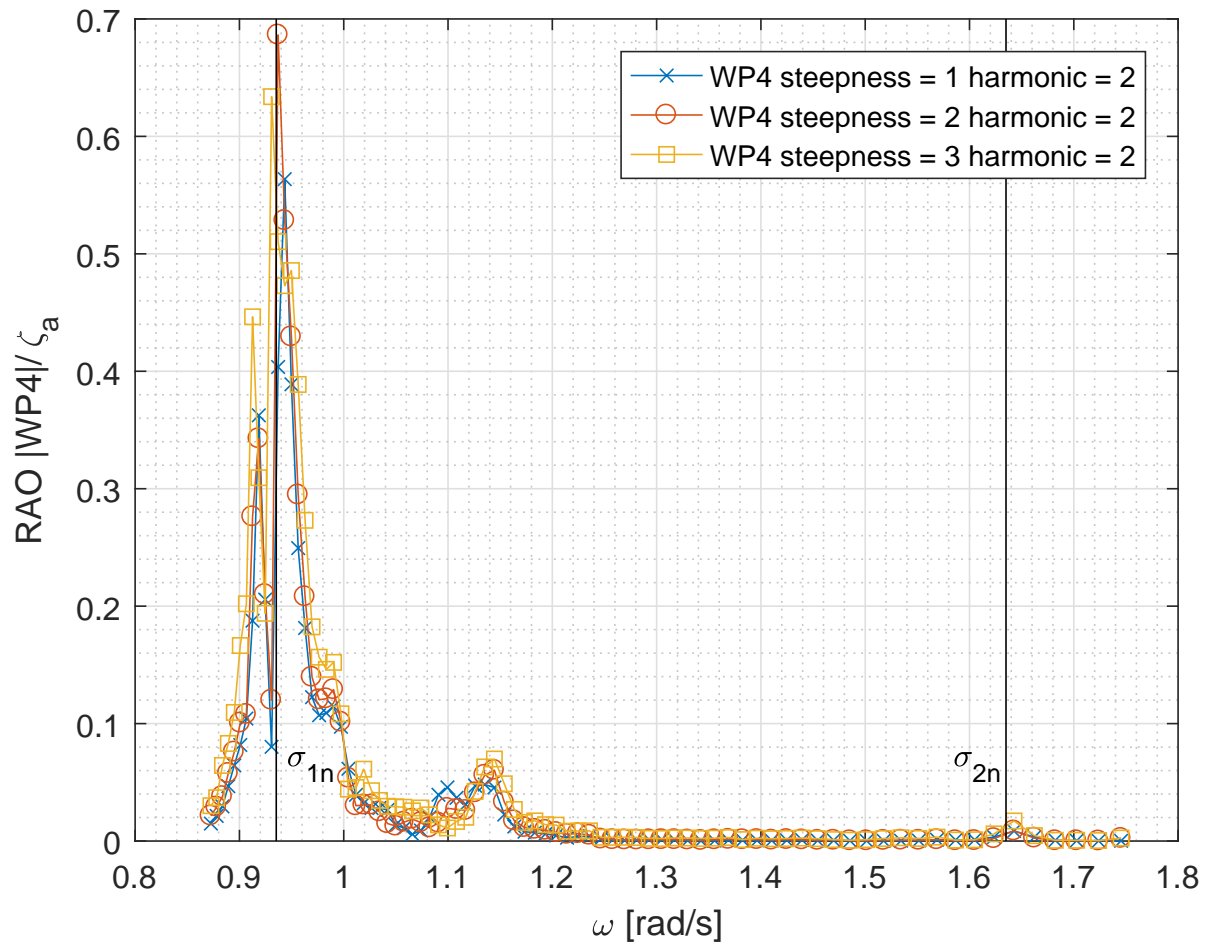
Figure F.15: RAO for internal wave probe WP3 in full scale for 1st harmonic for wave steepness $H/\lambda = 1/30$, $1/45$ and $1/60$. The black vertical lines represent the first and second modal natural sloshing frequency.
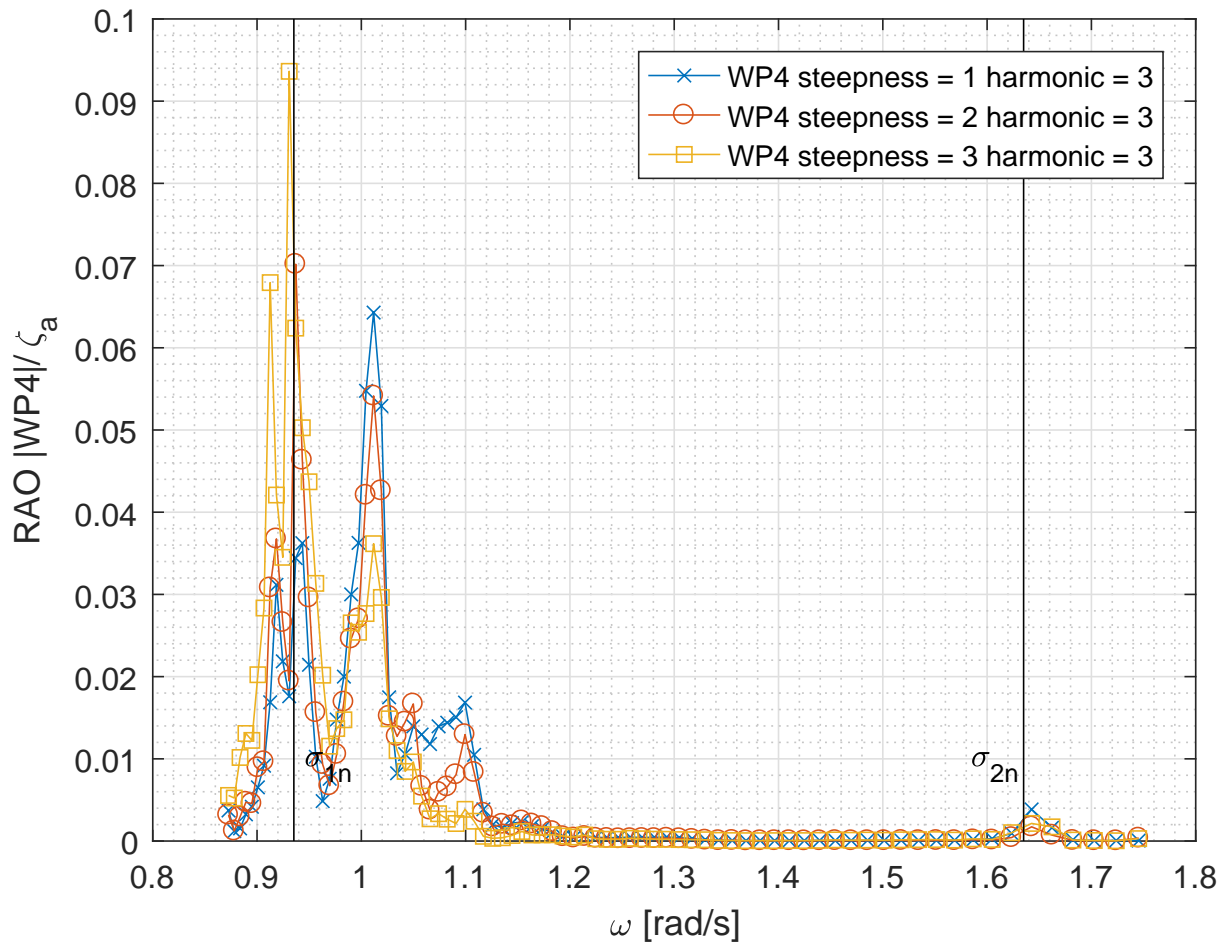
Figure F.16: RAO for internal wave probe WP3 in full scale for 2nd harmonic for wave steepness $H/\lambda = 1/30$, $1/45$ and $1/60$. The black vertical lines represent the first and second modal natural sloshing frequency.

Figure F.17: RAO for internal wave probe WP3 in full scale for 3rd harmonic for wave steepness $H/\lambda = 1/30$, 1/45 and 1/60. The black vertical lines represent the first and second modal natural sloshing frequency.

Figure F.18: RAO for internal wave probe WP4 in full scale for 1st harmonic for wave steepness $H/\lambda = 1/30$, $1/45$ and $1/60$. The black vertical lines represent the first and second modal natural sloshing frequency.

Figure F.19: RAO for internal wave probe WP4 in full scale for 2nd harmonic for wave steepness $H/\lambda = 1/30$, $1/45$ and $1/60$. The black vertical lines represent the first and second modal natural sloshing frequency.

Figure F.20: RAO for internal wave probe WP4 in full scale for 3rd harmonic for wave steepness $H/\lambda = 1/30$, $1/45$ and $1/60$. The black vertical lines represent the first and second modal natural sloshing frequency.

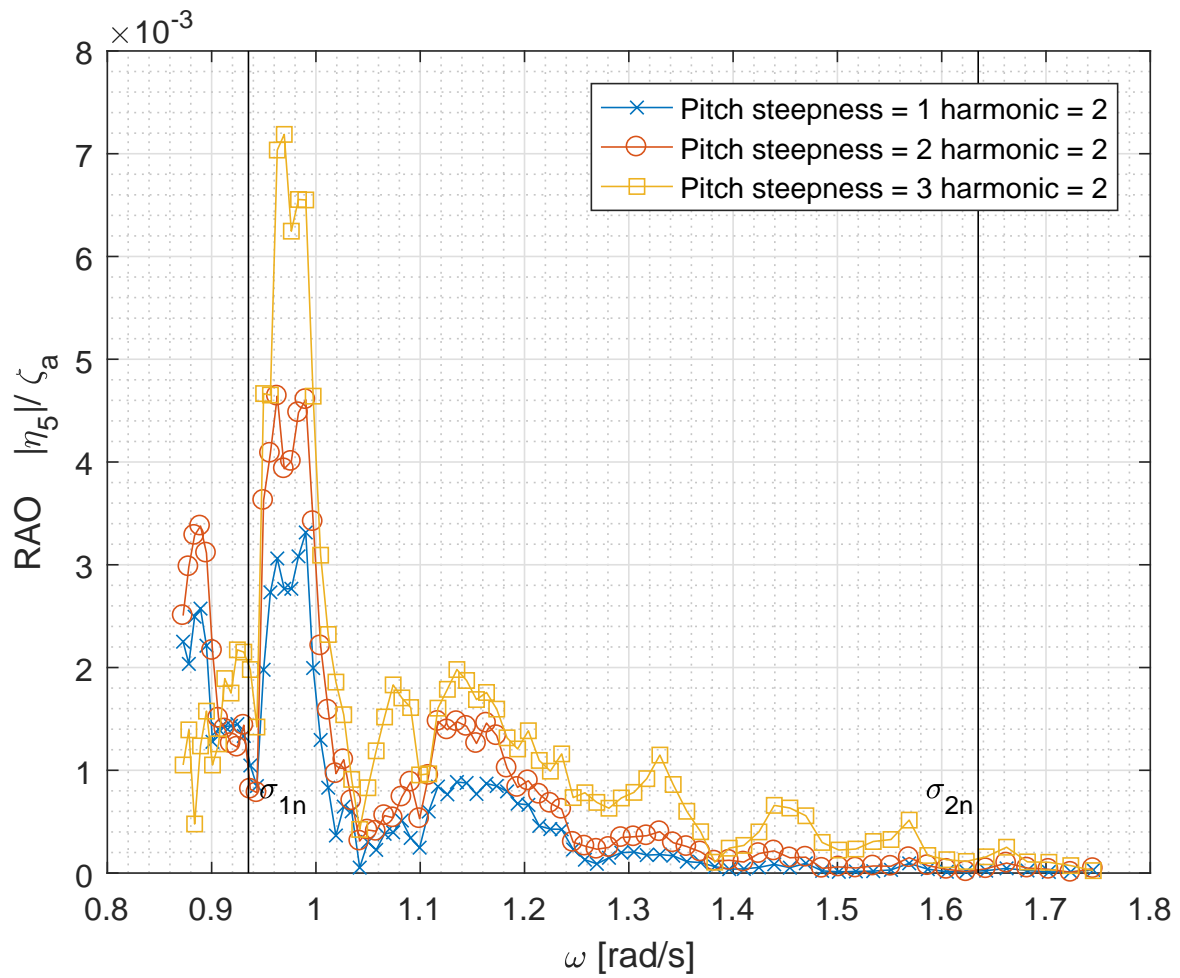## F.3   Steepness Comparison of Heave, Pitch and Surge for the Different Harmonics
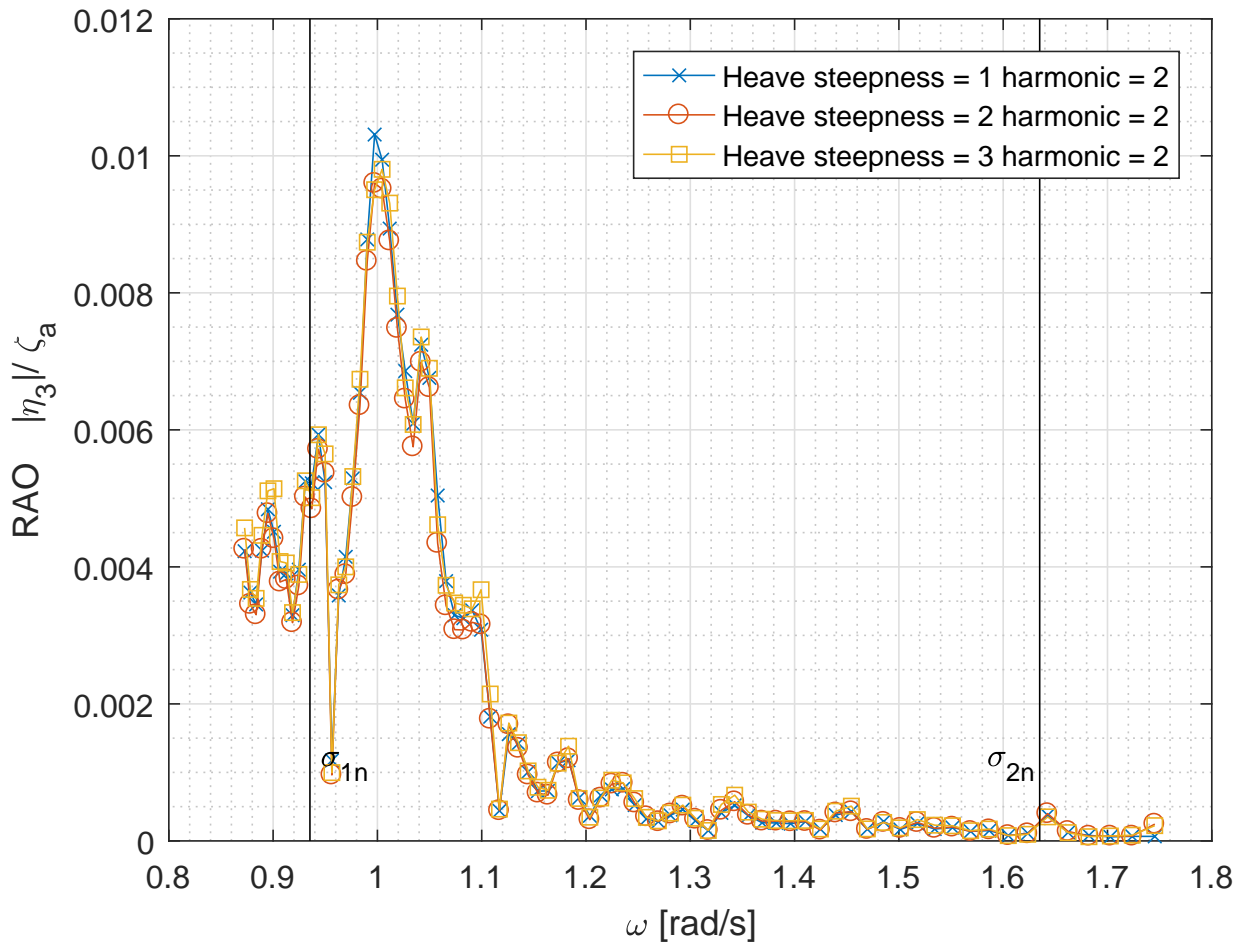
Figure F.21: The 2nd harmonic of the heave motion in full scale for the three steepnesses $H/\lambda = 1/30$, $1/45$ and $1/60$.
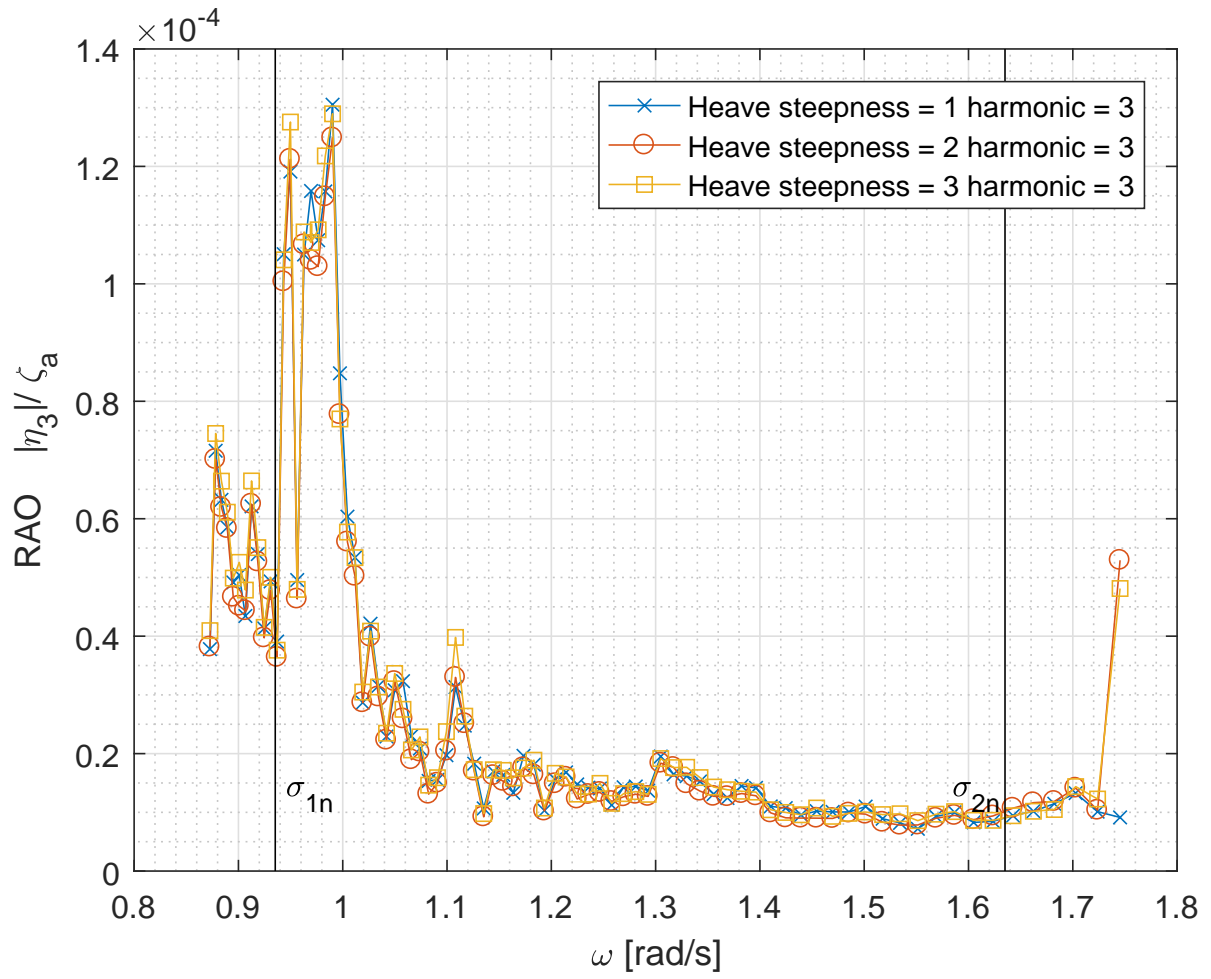
Figure F.22: The 3rd harmonic of the heave motion in full scale for the three steepnesses H/λ = 1/30, 1/45 and 1/60.

Figure F.23: The 2nd harmonic of the pitch motion in full scale for the three steepnesses H/λ = 1/30, 1/45 and 1/60.
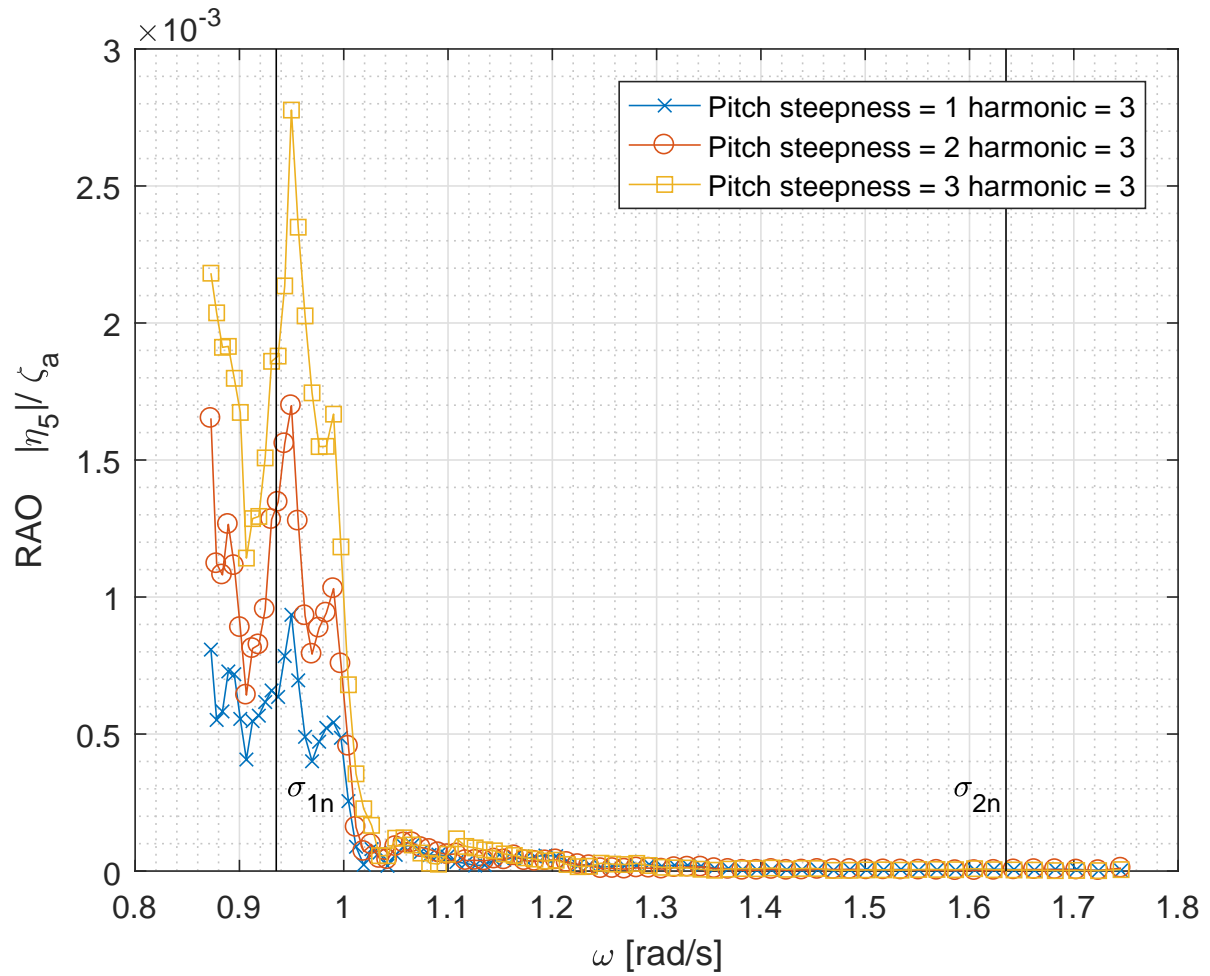
Figure F.24: The 3rd harmonic of the pitch motion in full scale for the three steepnesses H/λ = 1/30, 1/45 and 1/60.
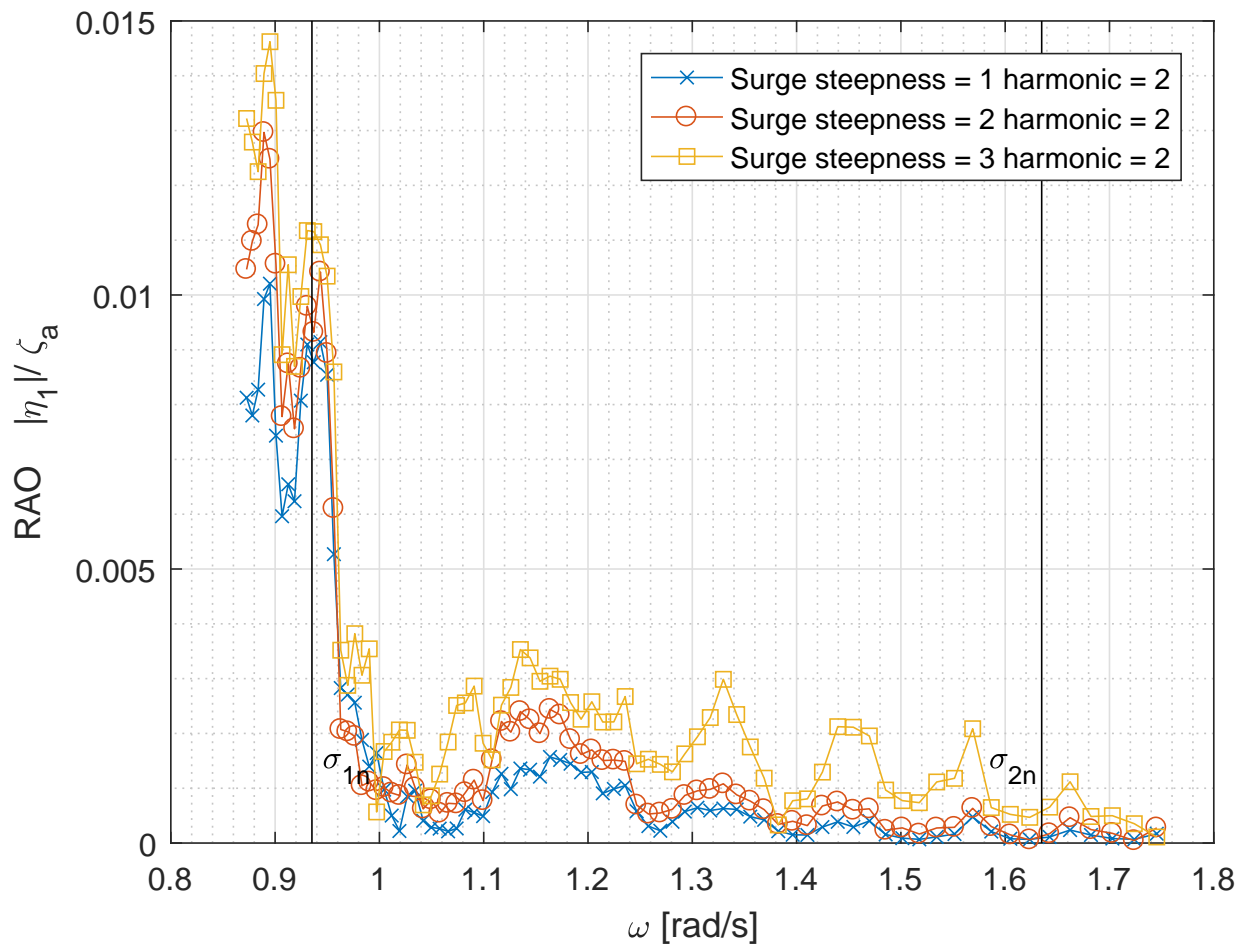
Figure F.25: The 2nd harmonic of the surge motion in full scale for the three steepnesses H/λ = 1/30, 1/45 and 1/60.
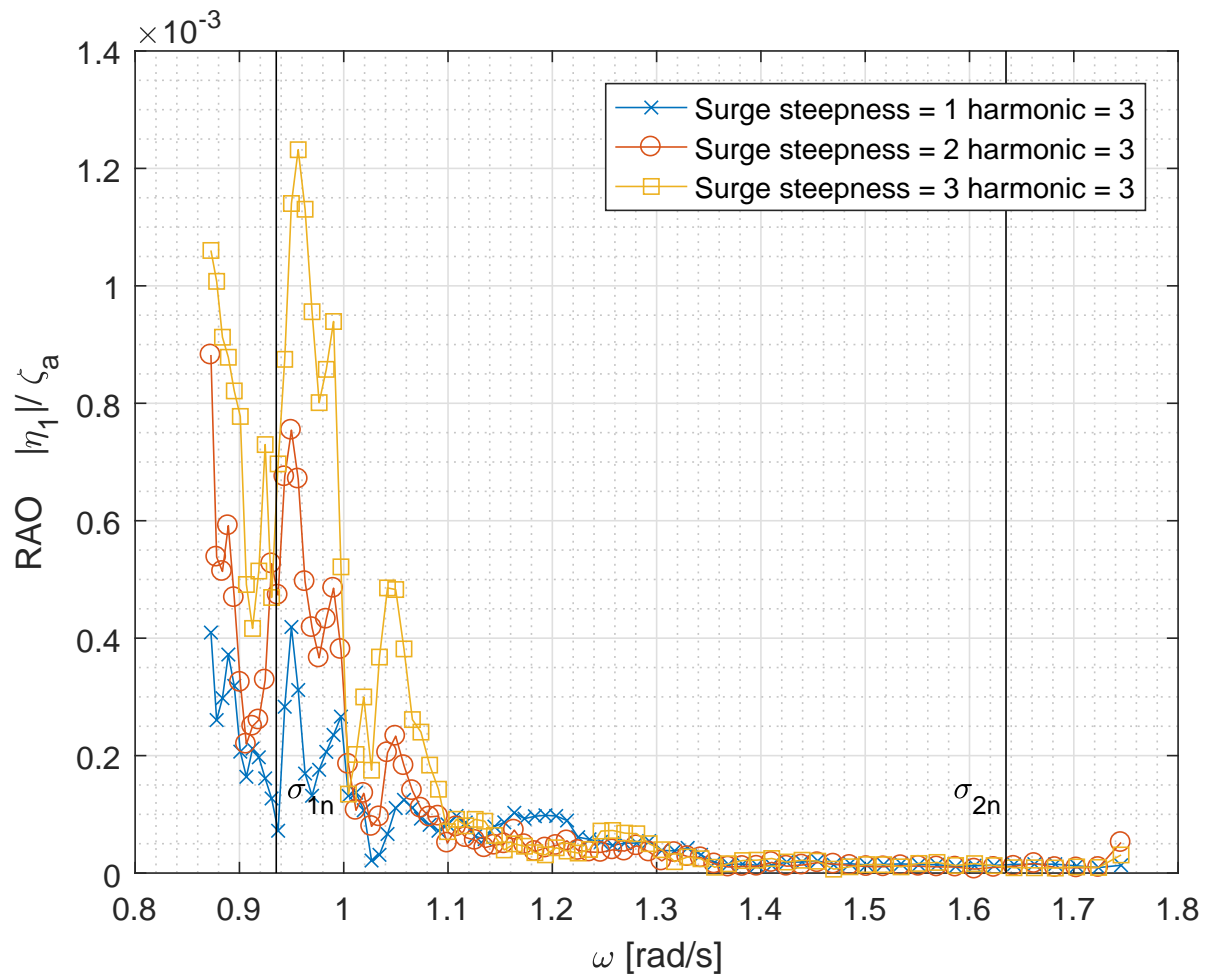
Figure F.26: The 3rd harmonic of the surge motion in full scale for the three steepnesses H/λ = 1/30, 1/45 and 1/60.